

Evolution of Metal Foams during Solidification

vorgelegt von
Master in Science (Engineering)
Manas Mukherjee
aus Indien

von der Fakultät III – Prozesswissenschaften
der Technischen Universität Berlin
zur Erlangung des akademischen Grades
Doktor der Ingenieurwissenschaften
-Dr.-Ing.-

genehmigte Dissertation

Promotionsausschuss:

Vorsitzender: Prof. Dr. Helmut Schubert

Berichter: Prof. Dr. John Banhart

Berichter: Dr. Carolin Körner

Tag der wissenschaftlichen Aussprache: 14.10.2008

Berlin 2009

D83

Abstract

The evolution of metal foams during solidification (cooling) was studied in-situ by means of X-ray radioscopy. Foams were processed by mixing metal powders (Al, Al-alloy and Zn) with TiH_2 powders and foaming the compact of this mixture inside X-ray transparent furnaces while foam evolution was continuously monitored. Foam expansion was quantified by analysing the radioscopic image sequence.

The main finding of this study is a hitherto unknown expansion stage during solidification of metal foams. This expansion stage has been referred as extra expansion or EE. Measurements were carried out by varying alloy composition, holding time (HT), cooling rate, gas atmosphere and pressure in order to understand the mechanisms responsible for EE.

In binary and ternary alloys EE stage can be subdivided into two parts (EE1 and EE2). It was observed that as HT increases, EE1 initially increases, then becomes nearly constant and finally decreases to zero. In contrast, EE2 was observed for all HT and even in foams free of blowing agent. While EE1 is mainly caused by the production of hydrogen from blowing agent, EE2 is a result of precipitation of dissolved hydrogen from the metallic melt during solidification. Cooling rate has significance influence on EE1: increases with decreasing cooling rate. Beside HT and cooling rate, EE is also influenced by the alloy composition.

The kinetic interplay of shrinkage of the hydrogen gas present inside the foam, the out-diffusion of hydrogen to the surrounding space and the production of hydrogen from the blowing agent was identified as the main reason of EE. It was observed that higher EE induces defects in the foam structure which is caused by EE-induced ruptures during solidification.

This page intentionally left blank

Declaration

Ich erkläre an Eides Statt, dass die vorliegende Dissertation in allen Teilen von mir selbständig angefertigt wurde und die benutzten Hilfsmittel vollständig angegeben worden sind.

This page intentionally left blank

Dedicated to my Mother and Sister

This page intentionally left blank

Acknowledgements

I would like to thank my research supervisor Prof. John Banhart for offering me the opportunity to pursue my PhD at the Department of Materials at Hahn-Meitner-Institute. I also thank him for giving valuable suggestions throughout my PhD. I am grateful to Dr. Francisco Garcia-Moreno for always helping me from the moment I landed in Berlin till the last days of my thesis submission. He has always given support in experiments, discussions and even in official works. Thanks are due to Prof. U. Ramamurty for giving useful suggestions and allowing me to work in his group in IISc, Bangalore, India. The valuable suggestions of Dr. Carolin Körner are thankfully acknowledged.

The help of Holger Kropf with the cutting and polishing of samples, Jörg Bajorat in computer problems and Yvonne Herzog in dealing with the never ending forms are highly appreciated. Dr. Ingo Manke and Dr Nikolay Kardjilov taught me X-ray tomography. Dr. Cynthia Chang and Stefan Höring are acknowledged for helping in various occasions. I thank all the SF3 members for creating a nice working ambience.

Special thanks are due to my colleague-cum-officemate-cum-friend Catalina Jimenez for her support and encouragement throughout my PhD. It's my great opportunity to thank Dr. Sashank Nayak and Dr. Vinod Kumar; the time spent with them at House-of-Nations in Berlin is highly cherished. I feel privileged to be a part of the metal foam group and would like to take this opportunity to convey my thanks to all my present and past colleagues, especially to Dr. Eusebio Solorzano, Dr. Alan Brothers, Dr. Norbert Babcsan, Dr. Axel Griesche, Hans Martin Helwig, Avinash Chethan, Nunzio Raffaele, Dichao Pan and Beate Pfretzschner. The non-stop help of Hans Martin Helwig in multiple topics is appreciated and gratefully acknowledge.

Thanks are due to my friends Tanmoy Banerjee, Avijit Santikary, Dr. Santonu Ghosh, Dr. Ravi Sankar Kottada, Dr. M.G. Basavaraj and Dr. Rejin Raghavan. The time spent with Dr. Chhaybrita Biswas, Ibrahim Khalil, Dr. Karen Nahmod, Ehsan Mohsenian, Dr. Rakesh Sohail, Pinki Sohail, Meenakshi Sarkar, Nilam Barekar, Dr. Jens Vierke, Jens Brunner and Eliana Jimenez in several occasions are cherishable. Dr. Rajani Panchang is remembered for being a wonderful friend to me. The effort of Frau Koppe for teaching me German is highly appreciated.

Last but not least, I would like to take this opportunity to show my sincere gratitude to my mother, sister and all the family members for their constant support and encouragement in all my endeavours and cheering me for all the achievements.

This page intentionally left blank

Contents

1	Introduction	1
1.1	Definition of metal foam	1
1.2	A brief history of metal foam production	2
1.3	Physics of metal foaming	5
1.3.1	Source of gas for foaming	5
1.3.2	Foam evolution	6
1.3.3	Foam stabilization	8
1.3.4	Effect of processing conditions on foaming	9
1.4	Objectives of the present work	9
2	Experimental	13
2.1	Materials	13
2.1.1	Powders	13
2.1.2	Precursor preparation	13
2.2	Experimental set-up	15
2.2.1	Lamp furnace	15
2.2.2	Pressure furnace	16
2.2.3	X-ray radioscopy set-up	17
2.2.4	Image analysis	17
2.2.5	X-ray computer tomography	19
2.3	Experimental methodology	19
3	Results	21
3.1	Temperature calibration	21
3.2	Foaming process	25
3.3	Anomalous behaviour during solidification	27
3.3.1	Anomalous expansion or <i>extra expansion</i>	27
3.3.2	Cooling curve of foaming	28
3.3.3	Cooling rate curve and <i>extra expansion</i>	29
3.4	Holding time experiments	30
3.4.1	Results for AlSi6Cu4 alloy	30
3.4.2	Results for AlSi7 alloy	36
3.4.3	Results for other alloys	37
3.5	Cooling rate experiments	39
3.5.1	Results for AlSi6Cu4 alloy	39
3.5.2	Results for AlSi7 alloy	42
3.5.3	Results for other alloys	45
3.6	Pressure induced foaming (PIF)	46

3.7	Distribution of extra expansion inside foam	49
3.8	Foam morphology	51
3.8.1	Macrostructure	51
3.8.2	Microstructure	52
3.9	Influence of atmosphere on foaming	54
3.10	Summary of the results	57
4	Discussion	59
4.1	Phase transformations in alloys.....	59
4.1.1	Al-Si-Cu system.....	59
4.1.2	Al-Si system.....	61
4.1.3	Al-Cu-Mg system.....	61
4.2	Foam formation kinetics	64
4.2.1	Decomposition of TiH_2	64
4.2.2	Foam expansion behaviour	65
4.3	Individual contributions to volume change of foam during solidification.....	69
4.3.1	Hydrogen production from TiH_2	70
4.3.2	Precipitation of hydrogen.....	71
4.3.3	Recalescence effects	74
4.3.4	Solidification shrinkage of metallic melt.....	74
4.3.5	Gas bubble shrinkage	77
4.3.6	Hydrogen out-diffusion.....	77
4.3.7	Contribution from all mechanisms.....	80
4.4	Reason of extra expansion – the kinetic effects.....	80
4.5	Individual influences on extra expansion.....	83
4.5.1	Holding time	84
4.5.2	Alloy composition – gas evolution from dissolved hydrogen	87
4.5.3	Alloy composition – fluidity of metallic melt.....	88
4.5.4	Alloy composition – rate of gas production from TiH_2	91
4.5.5	Cooling rate.....	94
4.5.6	Heat capacity of furnace	96
4.6	Practical relevance of extra expansion and its effect on foam structure.....	96
5	Summary and Conclusions	99
	Appendix A – Fatigue of a laterally constrained closed cell aluminium foam.....	101
	Appendix B – Hydrogen solubility calculation in aluminium alloys.....	102
	Appendix C - Calculation of out-diffusion of hydrogen from foam.....	103
	References	104

1 Introduction

It is amazing that metal foams are being considered as interesting materials not primarily for their metallic constituents but for their emptiness or voids. Metal foams are increasingly finding favour in the scientific community due to their novel physical, mechanical, thermal, electrical and acoustic properties. The high specific strength or stiffness (i.e., strength/stiffness to weight ratio) in conjunction with functional properties makes them potential material for light-weight construction, energy absorption and thermal management.

1.1 Definition of metal foam

Foams are a special class of dispersion of one phase in a second; see Fig. 1.1(a) [1]. By definition, foams are dispersions of gas cells in liquids. In case where the liquid is a metallic melt it is called *liquid metal foam*. Solidification of the metallic constituents results in solid material which is called *metal foam* or *metallic foam*. In general, the term metal foam is used for the solid, and the name *liquid metal foam* is reserved for the intermediate liquid stage that occurs during production. Sometimes they are also referred to as *cellular solids*. However, cellular solids which are not made from the liquid state can have any morphology. In contrast, metal foams can have only certain morphologies given by the minimization of surface energy during their production in the liquid state. The name metal foam usually refers to *closed-cell metal foams* as the cells (or bubbles) are predominantly isolated from each other. In the case where cells are interconnected is called *open-cell metal foams*. This thesis deals with closed-cell metal foams.

Metal foams consist of gas bubbles or cells. In foam bubbles take the form of spheroid or polyhedral cells. The components of a cell are film (cell wall in the solid state), Plateau border and nodes as shown in Fig. 1.1(b). A film separates two gas bubbles and shows a curvature due to the pressure difference between the two bubbles it separates. The pressure difference, ΔP , is given by the law of Laplace as follows:

$$\Delta P = \frac{2\gamma}{r}. \quad 1.1$$

The force of surface tension is γ , and r is the local radius of curvature of the cell wall [2]. This equation is valid only when one gas-liquid interface is involved, e.g. surface of a metallic melt. In foam every cell wall contains two gas-liquid interfaces, and, therefore Eq. 1.1 must be adjusted as follows:

$$\Delta P = \frac{4\gamma}{r}. \quad 1.2$$

The intersections of the cell walls are denoted as Plateau borders. These are interconnected in a disordered way and form a network whose nodes are junctions of at least four Plateau

borders. In 2D, cell walls and Plateau borders are represented as lines and intersection of lines, respectively.

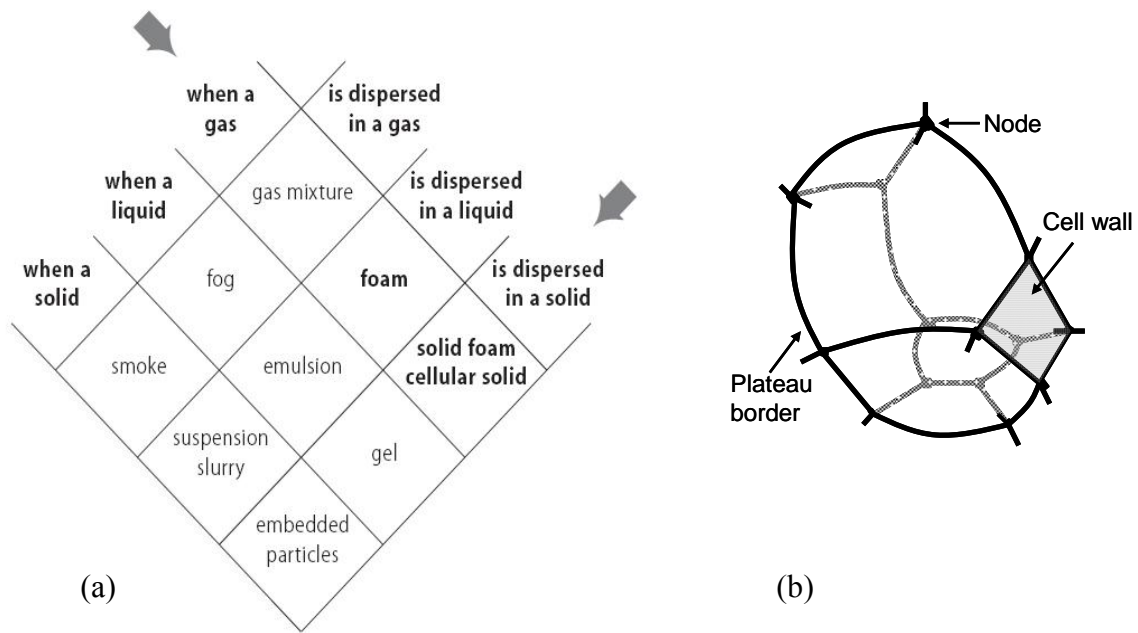


Figure 1.1. (a) Dispersions of one phase in a second one, where each phase can be in one of the three states of matter [1]. (b) Schematic of a cell or bubble (inside foam) and its structural components.

The geometry of the foam is determined by two conditions – minimization of surface energy and space filling. Only a limited number cell geometries is space filling. Previously the so-called Kelvin cells were thought to minimize energy. Today Weaire-Phelan cells are known to fill the space more efficiently [2]. Real metal foam structures, however, are far away from the theoretical ones. During its evolution process from the liquid state metal foam does not get enough time or scope to minimize its surface energy and thus remains in a metastable state. In general, if a foam (liquid) contains more than a percent or so of liquid, by volume, the structure does not conform to the efficient-space-filling geometry. Liquid metal foams usually contain 10 percent or more of liquid by volume. Hence, their structure cannot be defined by any of the space filling ideal polyhedral cells.

1.2 A brief history of metal foam production

One of the first ever reported evidences of metal foam is by Meller in 1926 [3]. The foaming of light metals (e.g. aluminium and aluminium alloys) either by inert gas injection or by using a blowing agent (e.g. carbonate and bicarbonate) was suggested. Later, Sosnick in 1948 [4] and subsequently in 1951 [5] proposed a technique to produce foamed aluminium by vaporization of mercury in molten aluminium. Subsequently Elliott brought the idea of adding

TiH₂ and ZrH₂ as *blowing agent* or *foaming agent* to the molten aluminium alloys to produce metal foams [6]. The blowing agent may be mixed with metal powders instead of molten metal in order to produce foam. This was realized by Pashak in 1960 [7]. Mixture of metal (Al or Mg) and Mg/Cd carbonate powders were used as starting material. The mixture was subsequently extruded and thereafter the extruded material was heat treated to produce foam. Later the process was further developed by Allen et al. [8]. They used ZrH₂, TiH₂ and CaCO₃ as blowing agent. Beside Al and Mg metals or alloys, other metals, e.g. Pb-Zn alloy, were foamed by Niebylski et al. [9]. They showed that stirring during the addition of blowing agent results in a more uniform structure. Pre-treatment of blowing agent was introduced by Speed in 1976 [10]. The onset of decomposition of the metal hydride thus can be controlled. Patten showed an alternate way of foam production by entrapping gas in metal and subsequent heating to above the melting point [11]. Holding the metal above its melting point permits the entrapped gas to expand and finally resulting in foam.

The first and frequently cited review article on metal foams was published in 1983 by Davies et al. [12]. This article summarizes the early years of development in metal foam research. In the early history of metal foam production a small number of scientific articles were published. Most of the citations given by Davies et al. concerns patented work. It is not entirely clear whether the ideas proposed in those patents actually worked. A second stage of activity started in the late 1980s with industrial take up and gradual increase in scientific interest. In 1987, at Shinko Wire Company (Japan), Akiyama developed a process which allowed economic production of metal foams [13]. Addition of Ca and TiH₂ with aluminium melt combined with stirring proved to be faster way of production. This process was quickly commercialized and given the trade name *Alporas*. Foaming by gas injection was explored in 1990s at Alcan International in Montreal (Canada) [14]. Introduction of gas into a metallic composite (containing ceramic particles) generates foam at the surface of the melt. This process is currently being exploited by Cymat in Canada. The production based on metal and blowing agent powders as starting materials was brought to sophistication at Fraunhofer-Institute in Bremen (Germany) by Baumeister [15]. This process is known today as *powder metallurgical* or PM route of metal foam production; this method is being exploited by the Austrian company Alulight. There is a considerable difference in hydrogen solubility in liquid and in solid metal. A metallic melt, saturated with hydrogen, forms cylindrical pores upon directional solidification due to the rejection of the gas at the solid/liquid interface. This property was exploited to produce the so-called *gasar* foams [16]. Nakajima used the same principle to produce porous metals known as *lotus-type porous metals* [17].

In 2000 a processing technique called *FORMGRIP* was proposed that combines some of the advantages of melt- and PM-route approaches [18]. It involves preparation of a precursor material by dispersion of gas-generating particles in a liquid aluminium-based/SiC_p composite, followed by solidification. Subsequent heating of this precursor results in foam. A new concept of gas injection that leads to foams with excellent uniformity of cell sizes was developed in Kleinreichenbach (HKB), (Austria) [19]. By casting the foam into moulds, complex-shaped foamed parts can be manufactured. This type of foam is called *Metcomb*. A

new processing technique was developed at Hahn-Meitner-Institute in Berlin (Germany) [20]. This is based on the PM route except that it does not require addition of any blowing agent. At first, the heating of the metal powder compact is done under overpressure, after which the subsequent release of pressure results in foam. This process is referred to as *pressure induced foaming* or PIF. Alloys with high melting point can be foamed in the solid state using pressurized entrapped gas. In this process metal powders are consolidated under high Ar pressure. Subsequent heat treatment (below the melting point) further increases the pressure of Ar present in the voids, and when the pressure exceeds the resistance to plastic flow, the component expands by either plasticity or creep [21, 22]. This kind of foaming is called *solid state foaming* and is being used by Boeing to create low-density core Ti-6Al-4V sandwich panels with pore fractions up to 50% [23]. A detailed description of all the processing techniques of metal foam can be found elsewhere [23–25].

History of development of new material suggests a scenario like the one sketched in Fig. 1.2 as suggested by Ashby et al. [23]. Research work on new material grows rapidly followed by a slump before flourishing again in association with industrial take-up. Usually in 15 to 20 years a new material should find implementation. In case of metal foams the scenario is not consistent with the usual trend. Metal foams did not find any real industrial application even in the 65 years after their first production. Perhaps the process control was not adequate to produce foam with reproducible quality, or the need for light-weight materials was not high enough before 1990s as suggested in [25]. Having started its journey almost in the beginning of the twentieth century, metal foam is still far from being perfect and certainly a long way to go before it can establish itself at a higher status in the era of modern materials.

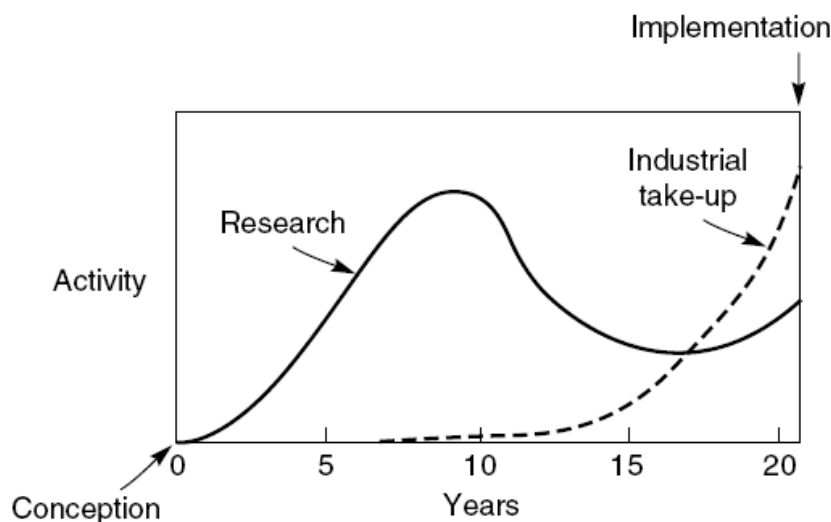


Figure 1.2. Typical development history of many new materials. Research into the new material grows rapidly, and then slumps when little interest is shown by industry in using it. On a longer (15-year) time scale, applications slowly emerge [23].

1.3 Physics of metal foaming

Metal foam research can be classified broadly into two categories: the first, physics and technology of foaming; the second, characterization of structure and properties. The study of the physics of foaming is necessary to understand the underlying principle of metal foam formation and stabilization in order to produce better foam. On the other hand, characterization of properties allows assessment of foam qualities and opens up prospects of application. An impression of the main research activities is shown in Fig. 1.3, which, however, does not include all the current activities on metal foams. The following sections discuss the key improvements made towards understanding the physics of metal foaming as the present thesis also deals with the same.

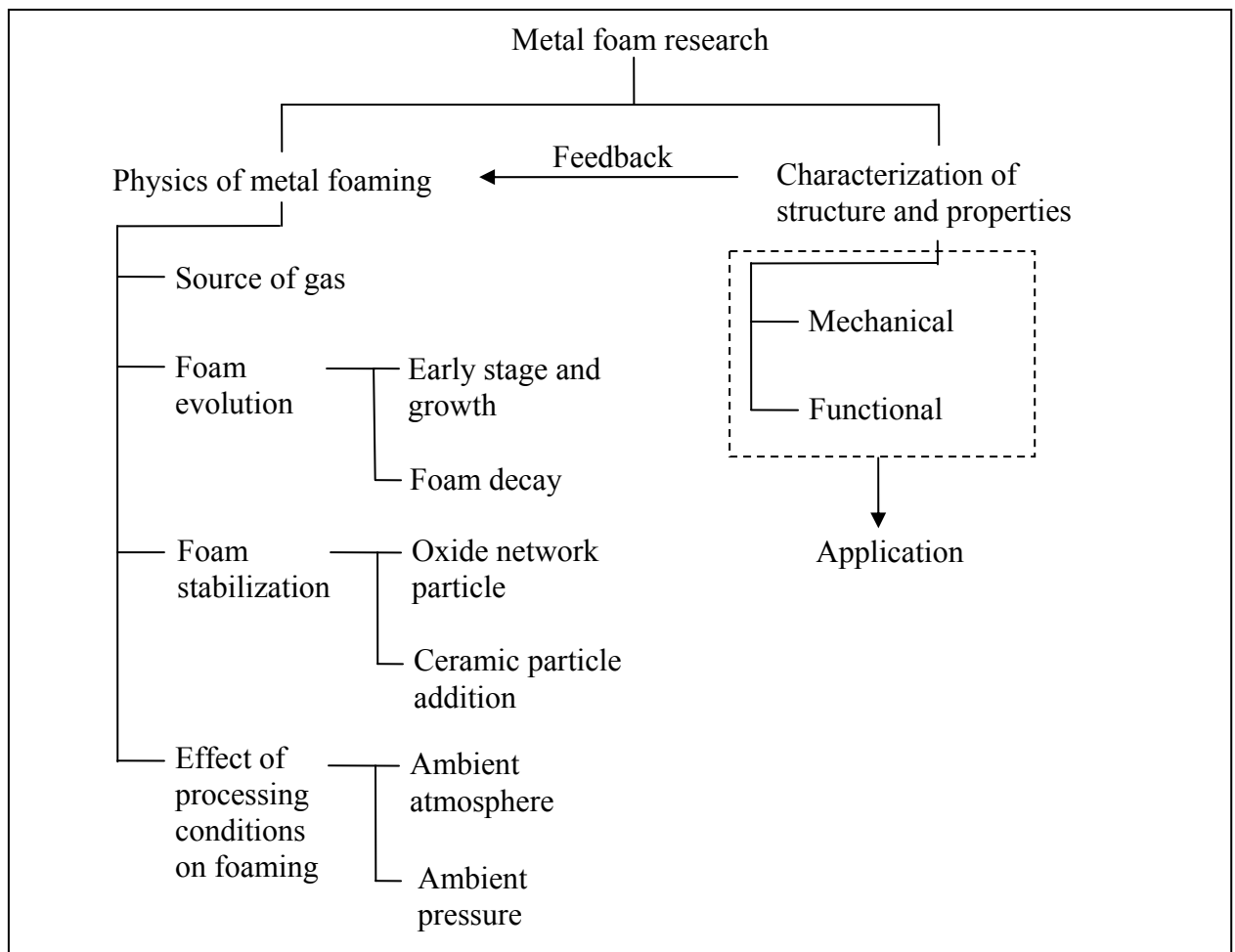


Figure 1.3. Landscape of metal foam research.

1.3.1 Source of gas for foaming

The formation of porosity in metal foam requires a gas source. Gas can be supplied either by *gas injection* from outside into the molten metal or by in-situ decomposition of gas-releasing *blowing agent*.

The gases usually used (in the gas injection method) are air, oxygen, nitrogen and argon [19, 26]. Originally air, carbon dioxide, water vapour or any inert gas were proposed [14]. Gas injection is straight-forward and can be performed whenever required. However, control of pore size is rather difficult to achieve. At present, only Metcomb foams guarantee uniform pore size and density distribution [19].

Most of the foaming techniques (Alporas, FORMGRIP and PM) utilize gas from the decomposition of blowing agents, particularly TiH_2 . To ensure satisfactory foaming, the melting temperature of the metal and the gas decomposition temperature range of the blowing agent have to be coordinated. The decomposition below the melting point of the metal leads to cracking and premature escape of gas resulting in a non-uniform foam structure [27]. Pre-treatment of TiH_2 is performed to form an outer oxide layer (TiO_2) which delays gas evolution [18, 28, 29]. By using pre-treated TiH_2 , better foam structures can be achieved [27, 30]. Alternatively, coating of TiH_2 powder particles with SiO_2 layers [31] or $\text{SiO}_2/\text{Al}_2\text{O}_3$ binary layers [32] also proved to be efficient in delaying gas release. ZrH_2 and MgH_2 are the other metal hydrides used as blowing agent [33–35]. Besides metal hydrides, carbonates are used. The carbonates of Cu, Mg, Zn, Pb have been used for foaming lead and lead alloys [33], while CaCO_3 has been identified suitable for foaming aluminium [36]. Depending on the melting point of the alloy one has to choose the blowing agent [34].

It has been suggested that the adsorbants present on metal powder surface can release sufficient gas for foaming; this property is exploited to produce foam by PIF [20, 37]. Release of hydrogen gas from as-received metal powder and further enhancement in amount when exposed to humidity has been verified by mass spectrometry study [38]. Entrapped pressurized inert gas for solid state foaming and dissolved gas for producing gasar foams are other kinds of gas sources in use.

1.3.2 Foam evolution

The *early stage* and *growth* during foam evolution have been studied by several researchers. It has been reported that pore nucleation can occur in the solid state [39]. Gas evolution generally occurs below the melting point of aluminium alloy. The pressure generated by the gas can deform the matrix that has low strength at high temperature. It is interesting to note that this is actually the principle of solid state foaming. With the help of synchrotron tomography it has been shown that pore formation (in PM foam) initiates at the weak regions, e.g. Al/Si interfaces, by mechanical cracking [40]. The pores thus produced at early stages of foaming appear as cracks, the long axis of which is nearly aligned perpendicular to the compaction direction [41]. Pressing parameters of foamable precursors, foaming temperature and heating rate were found to have major influence on foam expansion behaviour [42]. Early stages and growth have been investigated in situ with the help of synchrotron radiography [43] and ultra small-angle neutron scattering (USANS) [44, 45]. By means of numerical simulation of foam formation and evolution the effect of foaming velocity, hydrogen loss and gas

pressure on foam expansion and pore structure has been successfully demonstrated [46, 47]. Inter-bubble gas diffusion seems to have no significance on growth process as supported by other work [43]. However, in another study hydrogen diffusion through liquid aluminium has been reported to control pore size [48].

Foam decays by combination of three phenomena – *gas loss*, *drainage* and *coalescence*. Part of the gas is lost by diffusion from the outer surface to the surrounding. In the liquid state, loss is expected to be higher due to the higher diffusivity than in the solid state. However, crack formation during expansion at the outer surface of precursors can also lead to gas losses. Moreover, bubble rupture at outer surface also results in sudden gas loss. The second and third way of gas loss are random events and thus not much effort was attributed to assess their contribution except for some qualitative statement. Numerical studies showed that diffusional loss of gas can modify cell structures [46]. Surprisingly, the volume of the foam was shown not to be affected by this loss. Perhaps it was assumed that the continuous production of hydrogen is sufficient to compensate such losses, as argued by other authors [26].

Drainage is one of the driving forces for the temporal instability of molten metal foams. Drainage is caused mainly by gravitational and capillary effects. For aqueous foams this phenomenon is easier to investigate and already well understood [2]. In contrast, study of drainage in metal foams is difficult due to their opaque nature. Neutron radioscopy [49] and X-ray radioscopy [26, 50] were employed for in situ observation of drainage. It has been shown that qualitatively drainage in metal and aqueous foams is similar [49]. Predictions of numerical models were found to match with experimental observations [51]. Drainage in aqueous foams has been successfully described by incorporating the *foam drainage equation* (FDE) [2]. Brunke et al. showed that the standard FDE can principally be used to describe drainage in metal foams [52]. However, the effective viscosity was considered to be one order of magnitude higher than the original one to match the experimental observations. A high effective viscosity, even as high as 400 mPas in Ref. [51], due to the presence of oxide particles has been suggested by several authors [18, 43, 51, 53]. Foam produced under microgravity condition shows less drainage, and as a result higher expansion [54]. In our own investigation a significant difference in drainage behaviour between microgravity and terrestrial conditions has been observed by means of in-situ X-ray radioscopy [55]. The metallic melt which accumulates at the bottom of the foam due to gravity-induced drainage is absorbed by the foam due to capillary suction when exposed to microgravity conditions. This suggests that under normal gravity the capillary forces active in metal foams are weaker than gravitational force.

Coalescence of two bubbles is due to the rupture of the liquid film separating them. Thermal and mechanical instabilities result in such rupture. On the one hand foam expansion is intimately related with cell coalescence; this process is called growth coalescence [56]. On the other hand, coalescence also results in coarser foam morphology [54]. The coalescence process is rapid and requires high time resolution to observe. There have been several efforts to measure the time scale of film rupture. Time scale of rupture has been reported as less than

500 ms [43], less than 55 ms [57], less than 33 ms [26]. Recently, using high-speed synchrotron X-ray microradioscopy, rupture events were observed in detail and a time scale of between 400 and 1000 μ s has been established [58]. By simulation of rupture, a localized thinning process has been suggested as the initiation of rupture [47].

1.3.3 Foam stabilization

How metal foams are stabilized is the most controversial topic in the entire metal foam research. Aqueous foams are stabilized by surface active constituents (surfactants) which decrease the surface tension and produce a disjoining pressure against thinning of film [2]. Electrostatic screening of metals does not allow any disjoining pressure. Moreover, the high cell wall thickness (some 10 μ m) in metal foams also rules out the existence of traditional types of disjoining pressure [59]. Aluminium melt has one order of magnitude higher surface tension than water; this further reduces the foaming ability of aluminium. Nevertheless, despite all these facts metal foams show high stability. In general, a widely accepted theory of stabilization is the presence of particles, usually oxide particles. Solid particles in the cell wall result in a mechanical disjoining pressure and stabilize foam [59]. The presence of solid particles also increases the effective viscosity, which in turn reduces the drainage of the melt and thus prevents coalescence.

When foam is produced from liquid metals, a composite melt containing 10–20 vol.% of SiC particles (Duralcan) is usually used [18, 19, 26]. Alternately, solid particles can be created in-situ as it is done by the Alporas method by adding Ca to the melt which in turn produces CaO particles. Other frequently used ceramic particles are TiB₂ [60, 61] and Al₂O₃ [62]. The solid phase in partially solidified foam has also been suggested as stabilizer [35].

The question arises that why one needs 10–20 vol.% of stabilizing particles for melt route foaming process while very small amounts of oxide filaments (\approx 1%) are sufficient in the PM route [24]. The oxide layers initially present on the metal powder surfaces is sufficient for stabilization. By varying the oxide content of the powder, foam stability can be influenced [54]. During foaming, the oxides are not present as particles but form crumpled structures which form a global oxide network [56]. The effective volume fraction they occupy is much larger (30–35%) than the net oxide content. Some of the existing stabilizing theories are summarized by Haibel et al. [63]. In their investigation they did not find any network of particles. Instead, they concluded that liquid metal foams must be stabilized by interactions between particles attached to one side of a film. Recently Dudka et al. showed the existence of cluster-like oxide structure inside cell walls which might be part of a global oxide network [64]. A new approach based on single metallic film has been proposed to understand the stabilizing mechanisms instead of having to deal with the multitude of different structural elements present in a foam [61].

At the end the stabilization mechanism remains to contain many mysteries. During solidification growing solid phases push the oxide particles to the grain boundaries. As a

result, in the solidified structure the position of the particles might not be the same as it was in liquid state. The solution for this problem could be to perform high resolution and high-speed tomography of liquid metal foams; there is no doubt that it is a big challenge.

1.3.4 Effect of processing conditions on foaming

The ambient atmosphere and pressure play an important role for the foaming behaviour. Foaming under air increases oxidation of the outer surface layer and hinders foam expansion, while when foamed in argon higher expansion was observed [64, 65]. When an alloy with low tendency to oxidation is used, the final foam expansion varies only slightly on the type of atmosphere. Higher heating rate leads to higher expansion by reduction of the oxide formation [65]. The thickness of the outer oxide layer in aluminium foam has been reported as 92 and 30 nm when foaming was performed in air and argon, respectively [66]. Foaming under high pressure leads to smaller expansion but a better pore structure as it inhibits coalescence [56, 67]. In case of foaming using PIF, a higher expansion is observed when the precursor is melted under higher pressure, after which pressure is released to 1 bar [37].

1.4 Objectives of the present work

It has been already shown that the physics of the foaming process has been investigated by several researchers. Although a complete picture is still lacking, much progress has been achieved in last two decades. The major properties have been identified and metal foams are being applied in several industrial sectors. The strength of the foam comes entirely from the metallic part of the cell wall; the gas phase present in pores does not have any strength of its own. The foams in real application are in the solid state. Liquid metal foam is merely a stage that occurs during processing. It is obvious that *solidification* is an essential and unavoidable processing step that all liquid metal foams have to go through as illustrated in Fig. 1.4. However, in general, the study of solidification process has always been neglected; and thus it remains as the missing link between foam processing and their properties.

There are some studies found in the literature that address the solidification issue. The changes of porosity level during solidification have been estimated by Zhaojin et al. [68]. A model of solidification of metal foams based on the theory of quasi-equilibrium mushy zone was developed by Sobolev [69]. Based on that model the optimum conditions of solidification have been proposed in order to achieve better mechanical properties. A wide solidification region was suggested for better control of foaming process [70]. Stanzick et al. tried to estimate the number of cell wall ruptures during solidification [57]. It is evident that the number of references on solidification of metal foams is little and a complete understanding of the same is still lacking. The present thesis deals with some of the aspects of solidification of metal foams.

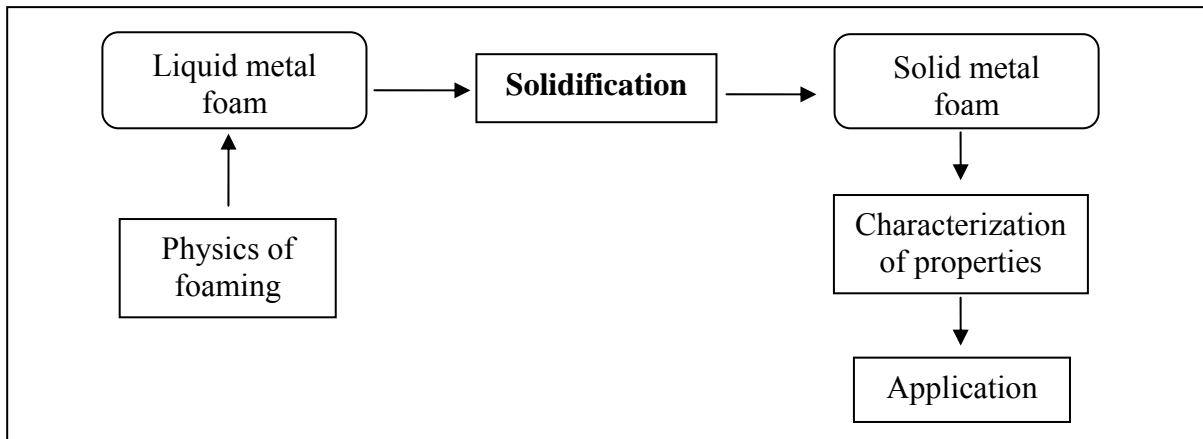


Figure 1.4. Schematic illustration of the importance of solidification in metal foam processing.

Solidification science of metals or alloys, from which the metal foams are made of, is already well established. It is expected that the solidification of the metal in the cell walls of foam will be, in general, similar to normal metal solidification. Hence, one can profit from the vast amount of literature that already exists on solidification. The strength of metals or alloys depends on their microstructure, which is determined by their solidification history and composition. In a similar way, the strength of metal foam is built up during solidification as the solid fraction increases from 0 to 1. Depending on the solidification conditions, different microstructures can be achieved. The importance of the microstructural features on the mechanical properties of foam has already been verified in several studies [71–73]. Porosity in the cell wall microstructure can lead to crack formation under mechanical loading [74]. Hence, it is imperative to have proper understanding of the cell wall microstructure of metal foams.

Formation of shrinkage or gas porosities is a well-known phenomenon in solidification [75, 76]. The choice of alloy composition and solidification rate determines the dendritic or cellular type microstructure, which in turn influences the amount of micro-porosity. The composition of the alloy also determines the fluidity of the metallic melt [76]. Fluidity has a great influence on shrinkage porosity and other defects that arise from the lack of fluidity. By applying these solidification ideas, one can predict the cell wall microstructure of metal foam. However, modification should be made as in metal foams solidification occurs in a section of small thickness, about 100–300 μm , i.e., the cell wall thickness.

Besides pore size, pore shape, and their distributions, the mechanical performance of foams also depends on macro-structural defects. Missing (or broken) cells, partially coupled cells and elliptical cells are the examples of such structural defects (some defects are shown in Fig. 3.37) [77–79]. It has been postulated that removal of cell walls can convert equiaxed cells into elliptical ones [77]. Partially coupled cells are characterized by the presence of a residual cell wall [79]. It has been shown that the cell morphologies and shapes dictate yielding. The band formation during deformation was found to initiate preferentially at elliptical and partially coupled cells [77, 79]. Removal of cell walls can also merge few small

cells into a larger one. Band formation was found to arise preferentially at the largest cells [80]. Our own investigations also showed that deformation starts at large and geometrically unfavourable cells (see Appendix A) [81, 82]. Given the role of cell shape and size, improvement of the mechanical properties through control of the cells during manufacture appears to be particularly challenging. While the elimination of large cells is tractable, approaches for avoiding elliptical cells are less clear [77].

It is not clear why there are missing cells or partially coupled cells. Considering the short time scale (less than 1 ms [58]) of cell wall rupture it is expected that cell shape can quickly rearrange and the liquid of the ruptured cell wall is retracted into adjacent cells. Therefore, it is not clear how partially coupled cells can be present in the final structure. Some hints have been provided by Körner et al. [56]; larger time scale of cell wall rupture is expected during solidification. The viscosity of the metallic melt increases with increasing solid fraction as solidification progresses. The much higher viscosity strongly slows down material redistribution. As a result, at very high solid fraction the redistribution process can come to a halt and remains as residual cell wall, and thus creates coupled and elliptical cells. Slowing down of rupture due to an increase in effective viscosity was also mentioned by other authors [58]. In-situ observation of the solidification process can also clear this issue.

In the present study the solidification of aluminium foams was investigated in detail. Mainly the macroscopic contraction behaviour during cooling was studied by means of in-situ X-ray radioscopy. Micro- and macro-structural defects resulting from different solidification conditions were addressed. Some approaches to avoid these defects have been proposed. The main finding of the present study is a hitherto unknown expansion stage during solidification of metal foams. This expansion is an unexpected or *anomalous* behaviour since one would expect contraction of the foam throughout solidification. Some preliminary results have already been published [83]. The mechanisms behind this anomalous expansion behaviour are discussed in this thesis.

This page intentionally left blank

2 Experimental

2.1 Materials

2.1.1 Powders

Metal powders (Al, Si, Cu, AlMg50, Zn) and blowing agent powders (TiH₂) were used to prepare foamable precursors. Two different modifications of TiH₂ were used – as received (untreated) and heat-treated. Untreated TiH₂ was used only to prepare zinc-based foamable precursors. Heat-treatment of TiH₂ was carried out at 480 °C for 180 minutes in air. The metal powders and TiH₂ used are listed in Table 2.1 along with their supplier and purity level as given by the suppliers.

Table 2.1

Details of the metal and TiH₂ powders used to prepare foamable precursor

Powder	Supplier	Purity (%)
Aluminium	Aluminium Powder Company Ltd. (Alpoco), UK	99.7
Copper	Chempur GmbH, Karlsruhe, Germany	99.5
Silicon	Wacker Chemie, Munich, Germany	99.5
AlMg50	Possel Erzkontor GmbH, Lübeck, Germany	–
Zinc	Grillo-Werke Aktiengesellschaft, Goslar, Germany	99.99
TiH ₂	Chemetall GmbH, Frankfurt, Germany	98.8

2.1.2 Precursor preparation

To prepare Al-based foamable precursors through the *powder metallurgy* (PM) route, 30 g of metal powder(s) was mixed with 0.5 wt.% of TiH₂ powder (see Table 2.2) in a tumbling mixer (supplier J. Engelsmann AG, Ludwigshafen, Germany) for 15 minutes. For zinc, 0.6 wt.% of untreated TiH₂ was used. Precursors were also prepared without any blowing agent as indicated by “No blowing agent” in Table 2.2. After mixing, the powder blend was subjected to hot uni-axial compression using a hydraulic press supplied by MATRA-Werke GmbH, Frankfurt (Main), Germany. The press has a load cell of 1000 kN. To reduce friction and wear of the die, a coating spray namely Molykote (supplier Dow Corning GmbH, Wiesbaden, Germany) was used and dried before pouring the powder into the 36 mm diameter cylindrical steel die. Cold-pressing applying 295 MPa pressure, corresponding to 300 kN load in the press, was carried out first. The pressing device and a sketch of the die are shown in Fig. 2.1(a) and (b), respectively. In a subsequent step, the cold-pressed sample, die and punches together were heated up to 400 °C using an electric heater. During heating the

die was kept on top of a ceramic plate to minimize heat losses. Temperature was measured by a K-type thermocouple in a hole located in-between the inner and outer diameter of the die.

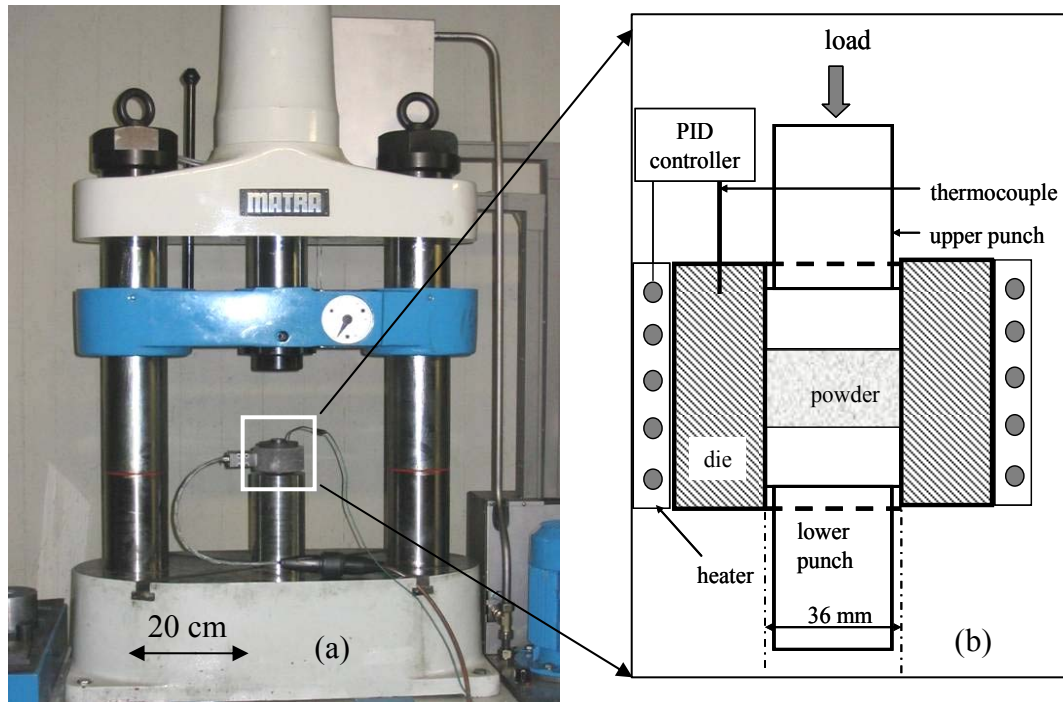


Figure 2.1. (a) 1000 kN uni-axial pressing device with die and heating system marked by white rectangle. (b) A detailed sketch of the die and punch showing the thermocouple, heating device and powder.

Heating time was approximately 20–25 minutes. Upon reaching 400 °C the temperature was maintained at 400 °C using a Eurotherm temperature controller, and the sample was again pressed using the same pressure for 5 minutes. At the beginning of the pressing, temperature came down ~10 K due to heat losses through the contact of the press. For zinc precursor, the preparation temperature was set to 350 °C. To prepare blowing agent free precursors, only metal powders (without any TiH_2) were mixed, the rest of the process was same. The alloys that were prepared by the PM route are listed in Table 2.2. Samples of dimension $10 \times 10 \times 4 \text{ mm}^3$ (mass ~1.1 g) were cut out from the pressed tablets by a Struers Accutom-50 cutting machine using aluminium oxide blade. The pressing direction is along the thickness (4 mm) of the sample. The foam manufacturing method by the PM route is shown by a flow chart in Fig. 2.2.

Table 2.2
Details of the alloys used as foamable precursors

Alloy	Blowing agent – TiH_2 (wt.%)
Al, AlSi7, AlSi11, AlSi6Cu4, AlCu13Mg4	0.5, pre-treated
Zn	0.6, untreated
AlSi6Cu4, AlCu13Mg4, AlCu13Mg1, AlCu20Mg5	No blowing agent

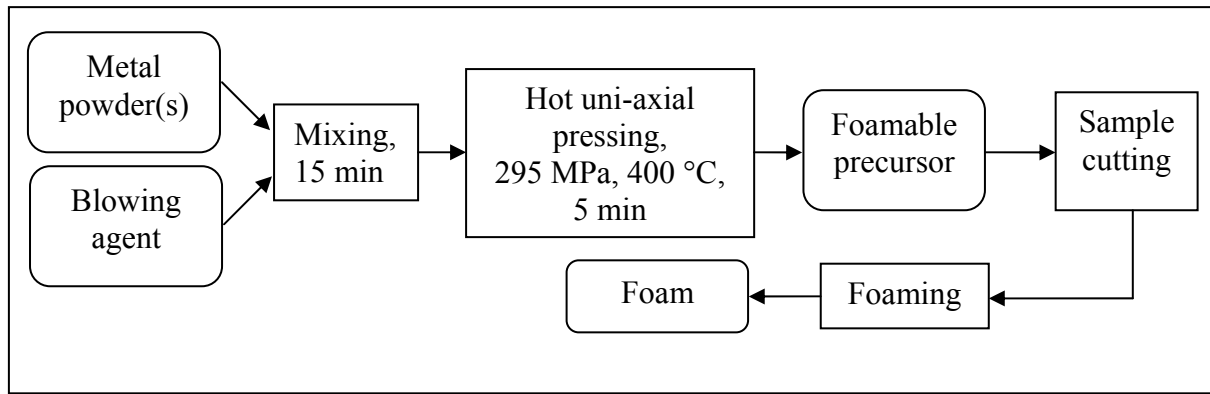


Figure 2.2. Flow chart of foam manufacturing method by the powder metallurgical route. The process parameters of aluminium-based precursor used in the present study are given.

2.2 Experimental set-up

2.2.1 Lamp furnace

This furnace consists of two halogen photo-optic lamps (Osram Xenophot HLX 64635) each of which has 150 Watt heating power and an IR reflector [67]. Both lamps are fixed to an aluminium frame as shown schematically in Fig. 2.3. The lamps are connected in series to a 300 W (30 V and 10 A) power supply. The input of the power supply (on or off) is the output from a temperature controller (JUMO dTRON 16.1). The temperature on the sample is measured by a K-type thermocouple and recorded by computer.

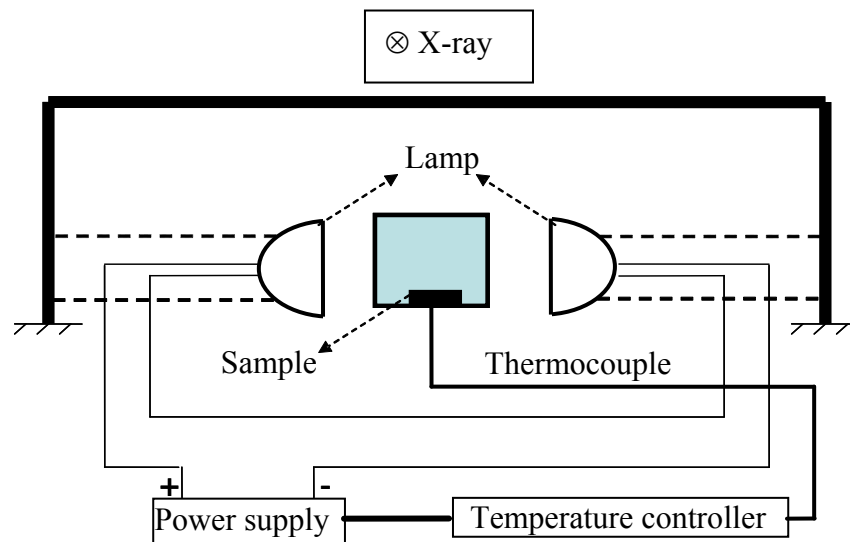


Figure 2.3. Schematic of the lamp furnace assembly.

Foaming was performed inside a steel square tube with the opened ends aligned in the direction of the X-rays. The inner vertical section of the tube (perpendicular to X-ray) is $25.5 \times 25.5 \text{ mm}^2$, thickness of the tube wall is 2 mm and length along the X-ray direction is 28 mm. The opened ends of the tube were covered with thin aluminium foils (0.1 mm) during foaming to minimize heat losses due to air convection. The steel tube was placed on a ceramic insulator (not shown in the schematic) to minimize heat losses by conduction. Centre of the steel tube's bottom surface has a hole through which the thermocouple was introduced.

2.2.2 Pressure furnace

This furnace is a specially designed resistive heater furnace that allows foaming under controlled pressure and gas atmosphere. It was mainly used to foam precursors without any blowing agent by the *pressure induced foaming* (PIF) method [37]. However, blowing agent containing samples were also foamed using this furnace for controlled-atmosphere foaming. This furnace consists an aluminium tube (40 mm diameter, 200 mm long, 0.5 mm wall thickness) sealed at both ends. It can operate up to a pressure of 9 bars. A sketch of the furnace is shown in Fig. 2.4. One end of the tube is used to introduce the sample as well as for heating and thermocouple connection. The other end is used as gas inlet/outlet. Heating was performed by a ceramic resistive heating plate (conducting graphite layer embedded in Si_3N_4) and has a maximum heating power of $\sim 600 \text{ W}$. The temperature was measured by a thermocouple touching the bottom surface of the heating plate. Temperature was controlled by a CAL 3300 temperature controller and recorded in computer. Later, a modified pressure furnace was constructed with steel casing and aluminium plate covered windows. Temperature measurement was improved by inserting a thermocouple through a drilled hole in the heating plate. The thermocouple touches the bottom surface of the foam. This furnace can operate up to 40 bar pressure.

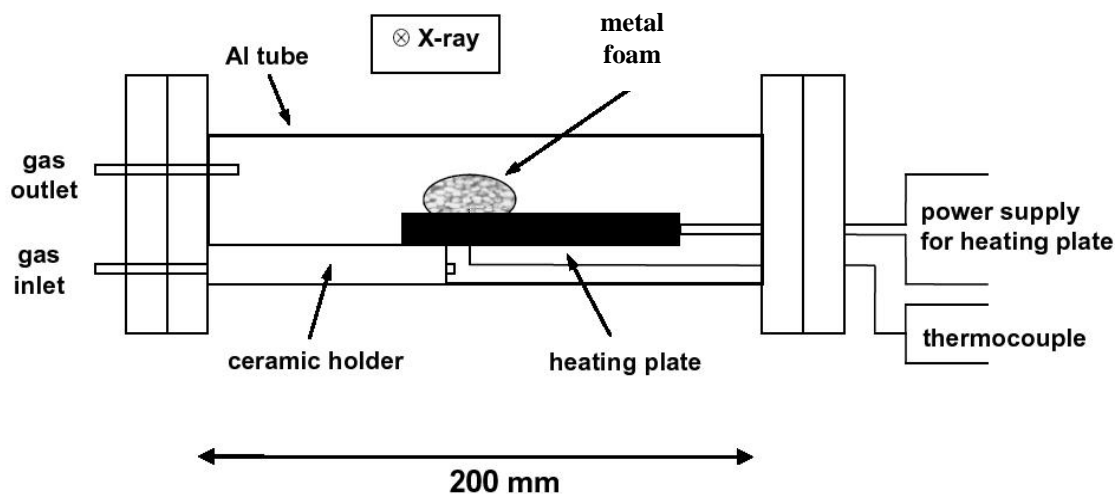


Figure 2.4. Schematic of the pressure furnace used for foaming.

2.2.3 X-ray radioscopy set-up

The foaming process was continuously monitored using an X-ray radioscopy set-up [67]. It consists of a micro-focus X-ray source and a flat panel detector for recording images, Fig. 2.5(a). Both were supplied by Hamamatsu Photonics, Japan. X-ray radioscopy allowed for in-situ monitoring of the evolution of foam and pore structure inside the foam, e.g., growth, coalescence etc. The X-ray source has a minimum spot size of 5 μm and can operate at a maximum of 150 kV, 500 μA . The flat panel detector has $2240 \times 2368 \text{ pixel}^2$ ($120 \times 120 \text{ mm}^2$) with 50 μm pixel size. Due to the cone beam geometry of the X-ray source the pixel size corresponds to, e.g. 5 μm at a magnification of 10. The maximum image acquisition rate varies from 1 to 9 Hz depending on the time and spatial resolution. HiPic (Hamamatsu, version 7.1) commercial software was used for image acquisition. The radioscopy image formation is illustrated schematically in Fig. 2.5(b). The image formed on the detector represents the X-ray projected image of the foam. The foaming is monitored from the X-ray projected images.

2.2.4 Image analysis

A quantitative analysis of foam expansion was performed with the dedicated software AXIM [84]. This computer analysis software is based on the commercial program PV-WAVE and is able to quantitatively analyze the expansion of the foam from the radioscopy images. Foam expansion is measured from the growth of the X-ray projected area of the sample. The projected area of the foam (A) normalized by that of the precursor (A_0) is defined as the *area expansion* (A/A_0). AXIM is able to separate darker object pixels from brighter pixel above and beneath the object and from black pixels of the sample support. The object pixels can be separated from the environment by fixed threshold criteria. An example is illustrated in Fig. 2.6. The original radioscopy image of foam and the corresponding reconstructed image after separating the foam from the background are shown in Fig. 2.6(a) and (b), respectively. Thermal expansion of the sample support is corrected applying a correction procedure. Apart from expansion calculation, AXIM is also able to detect rupture of cell walls and to measure density gradient and drainage in foam.

In general, the contrast at the boundary of the projected image of foam is small (e.g. see Fig. 2.5(b)) and sometimes can be so small that AXIM cannot distinguish exactly the boundary of the foam and the background (i.e., the detector). In those cases some fluctuations can be observed in the A/A_0 curve. These types of fluctuations can be visually verified by comparing the AXIM generated images with the corresponding radioscopy images. Every image sequence was visually checked and qualitatively matched with the resulting area expansion curve.

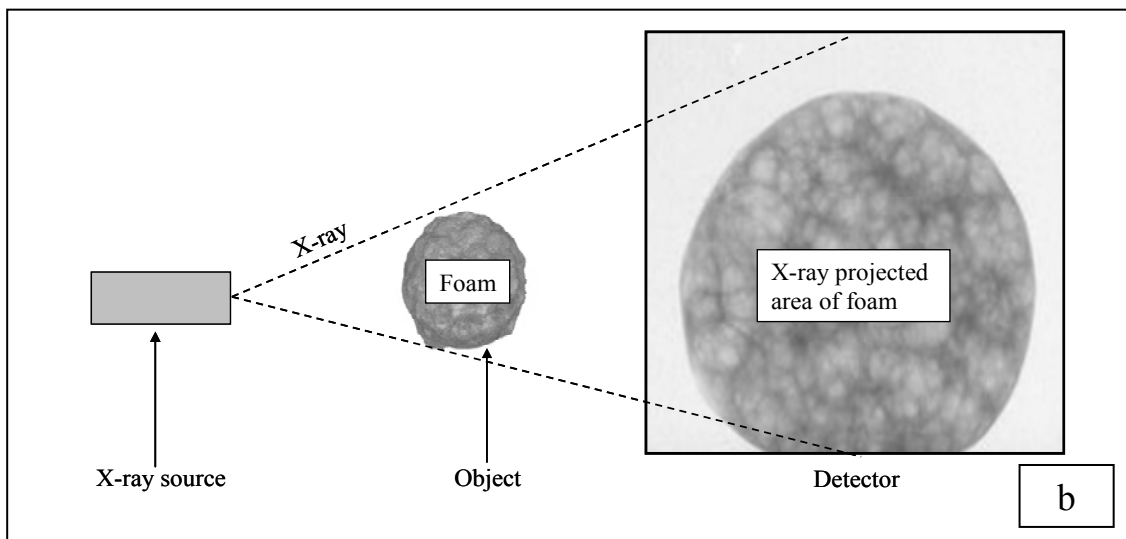
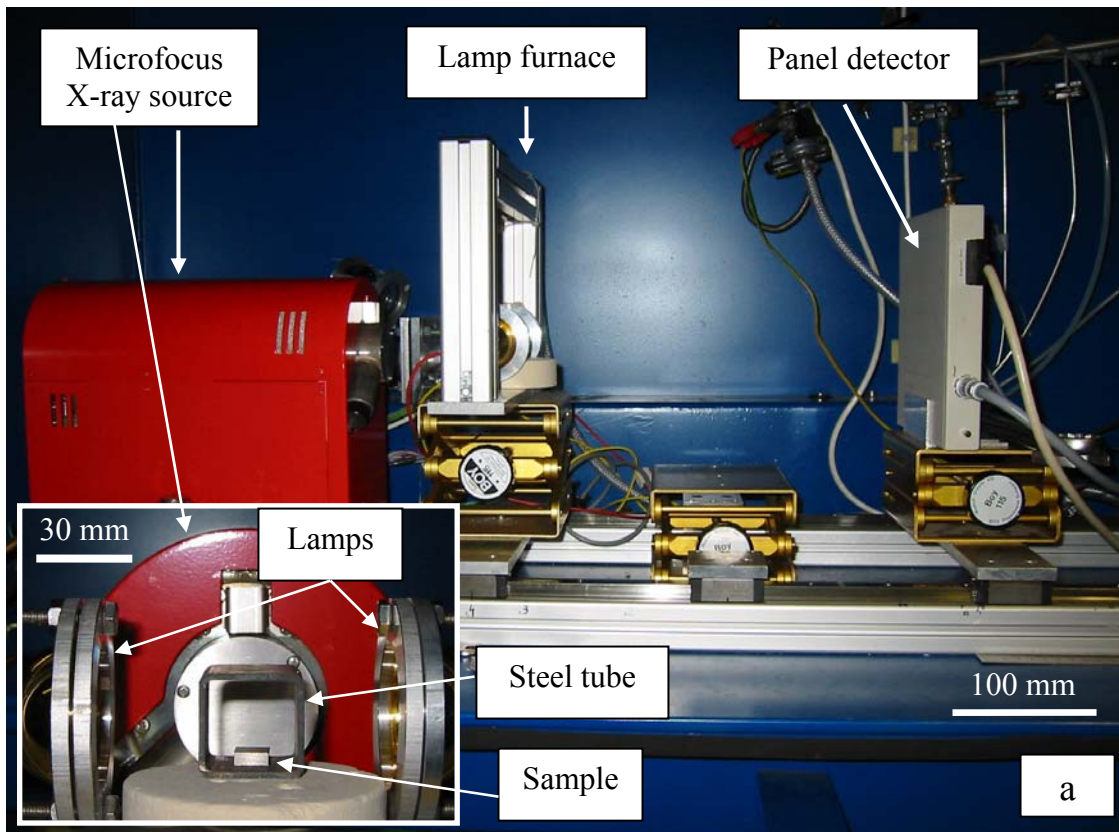


Figure 2.5. (a) X-ray radioscapy set-up consisting of a microfocus X-ray source and a panel detector. The lamp furnace is placed in-between the X-ray source and the detector. The inset shows a close-up (viewed from the detector side towards X-ray source direction) of the lamps, steel tube and sample. (b) Schematic illustration of the formation of radioscopic image (i.e., the X-ray projected image) of a foam.

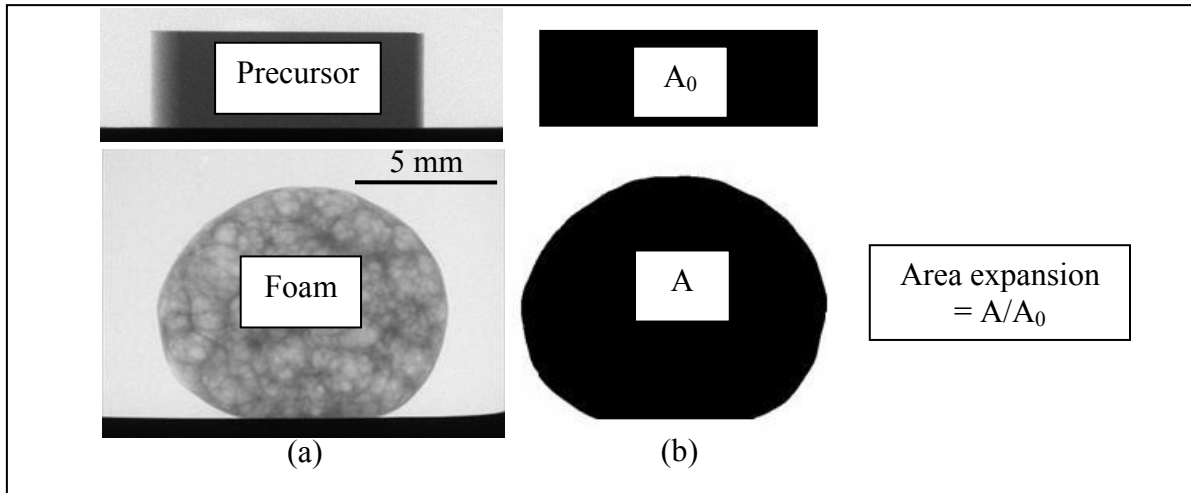


Figure 2.6. (a) Radioscopic images and (b) the corresponding image reconstructions by AXIM. Expression of area expansion is given.

2.2.5 X-ray computer tomography

Ex-situ structure analysis was performed by X-ray computer tomography. The same X-ray radioscopy set-up was used for this purpose. Foam was placed on a motor-controlled rotating table in between the X-ray source and detector. The foam was rotated by 1° at a time around its vertical axis and a radiographic projection of the foam was taken after each step. A total of 360 projections with an exposition time of 8s were taken for a complete rotation of the foam. Later tomographic cone beam reconstructions were performed on these projections using the commercial software Octopus 8.1. After reconstruction, the commercial software VGStudioMax 1.2.1 was used to visualize the reconstructed 3D volume of the foam.

2.3 Experimental methodology

In the present study the X-ray source was always used with $5 \mu\text{m}$ spot size at 100 kV voltage and 100 μA current. Images were recorded at a rate of 1 image per 2 seconds (0.5 Hz). The position of the furnace and detector was set for a magnification of 4 times. Unless otherwise indicated, all the samples containing TiH_2 were foamed in the lamp furnace. A hole was made at the centre of one of the $10 \times 10 \text{ mm}^2$ faces of the sample. The hole was just big and deep enough ($\approx 0.5 \text{ mm}$) to accommodate the tip of the thermocouple. The sample was placed on top of the thermocouple. Thus the measured temperature indicated the temperature at the bottom surface of the sample. Care was taken to ensure that the sample was in good contact with the steel tube's inner bottom surface, thereby guaranteeing reproducible and good heat conduction. In the direction of X-rays, the projection of the sample precursor is $10 \times 4 \text{ mm}^2$. To standardize all the experiments, heating from room temperature ($\sim 30^\circ\text{C}$) up to 600°C was considered as heating stage. The time from the point when temperature reached 600°C up to

the point when cooling started was considered as the *holding time* (HT). Maximum temperature reached during the holding period was 604 °C. Due to the open construction of the lamp furnace, temperature fluctuates and is not constant at the set point value (604 °C) during the constant heating period. However, it is usually above 600 °C. Therefore, 600 °C was chosen as reference and the time period through which temperature is above 600 °C was considered as constant heating period, i.e., holding time. Expansion mainly occurred against gravity direction. After the holding period, the foam was allowed to cool down. 0 s holding time indicates that cooling started immediately after the temperature reached 600 °C. While ambient cooling was applied by simply turning off the power supply of the lamps, slow cooling was achieved by decreasing the power of the heating lamps to a lower value and then turning off the power supply after temperature reached a certain value.

Blowing agent free samples were first heated inside the pressure furnace at overpressure using pressurized air. After melting of the samples, gas pressure was released to ambient pressure (1 bar). Release of pressure immediately induced expansion in the sample driven by the gas produced by the adsorbants present in the compact [37]. After foaming the experiment was identical to that of the samples containing blowing agent. The temperature measured in the pressure furnace does not provide the actual temperature of the sample but is lower, because the thermocouple touches the lower surface of the heating plate. In contrast, a higher temperature value is measured when the thermocouple is inserted through the heating plate in the modified pressure furnace. Because of its position immediately next to the heating plate, the thermocouple in the modified pressure furnace measures higher temperature than the real temperature in the sample. Therefore, prior to performing any experiment, the temperature set point was determined for each of these furnaces so that the temperature inside the sample would be the desired foaming temperature. Besides PIF or argon atmosphere foaming experiments, samples containing blowing agent were also foamed in these furnaces. Foaming of Al precursors was performed in these furnaces as the heating power of the lamp furnace is not enough to reach 660 °C. Table 2.3 lists all the various experiments that were performed and the corresponding furnace used.

Table 2.3
Various furnace set-ups used

Type of furnace	Heat source	Thermocouple position	Experiments performed
Lamp	2 lamps	Into the sample	AlSi6Cu4, AlSi7, AlSi11, AlCu13Mg4 (with TiH ₂ , foamed in air)
Pressure–9 bar	Si ₃ N ₄ heating plate	At the heating plate	Al (with TiH ₂ , foamed in air) AlCu13Mg4, AlCu13Mg1, AlCu20Mg5 (without TiH ₂ , foamed in air)
Pressure–40 bar	Si ₃ N ₄ heating plate	Into the sample	AlSi6Cu4 (with and without TiH ₂ , foamed in air and argon) Al (with TiH ₂ , foamed in air and argon)

3 Results

Foaming was triggered by heating the precursors to above their melting point. Expansion of the X-ray projected area of the sample was determined from radiosopic images by image analysis software. Analysis of the expansion graph revealed a transient expansion stage during solidification. This is an anomalous behaviour considering the fact that the foam made of gas and liquid/solid metal phases should shrink with falling temperature during solidification. Experiments based on different heating times and cooling rates were carried out to investigate the nature of this anomalous behaviour. AlSi6Cu4 and AlSi7 (containing 0.5 wt% TiH₂) are the main alloys used in this study. Some selective experiments were performed for other alloys as well. Except few, all precursors were prepared with blowing agent. Unless otherwise indicated, all the results shown in this chapter are for alloys containing 0.5 wt.% pre-treated TiH₂. Results from blowing agent free precursors will be mentioned separately. Foaming was performed in air. In some cases argon (Ar) was used; that will be mentioned separately.

3.1 Temperature calibration

It is necessary to place a thermocouple inside the foam in order to measure the real temperature of it. However this disturbs the stability and expansion of the foam. Moreover, the thermocouple is likely to be damaged during extraction from the solidified foam. Therefore, the thermocouple was placed in contact with the bottom surface of the foam as stated in section 2.3. In order to compare the real temperature inside the foam and the temperature measured at the bottom surface of the foam some calibration tests were carried out by using two thermocouples at the same time – the first one at the bottom surface of the foam and the second one inside the foam.

The first thermocouple was kept constant in all tests while the second one was placed inside the foam at various depths from the outer surface. The measurement scheme is illustrated schematically in Fig. 3.1. The starting precursor and the foam are expressed by thick dashed and solid lines, respectively. The filled circles indicate the positions of the thermocouples with respect to the foam. Thermocouples were placed approximately along the central vertical axis (shown as dashed-dotted line) of the foam or the precursor. They are indicated as TC_x (where $x = 1, 2, 3, 4$ and 5). Note that while TC₁ and TC₂ are in contact with the precursor; TC₃, TC₄ and TC₅ are initially outside of the precursor. They are placed in such a way that in the expanded foam the position of TC₃, TC₄ and TC₅ corresponds to the centre, in-between centre and top and top, respectively. TC₄ is about 3 mm from the outer surface of the foam after foam has expanded fully. By knowing the average foaming behaviour the final foam height was anticipated and accordingly the thermocouples were placed.

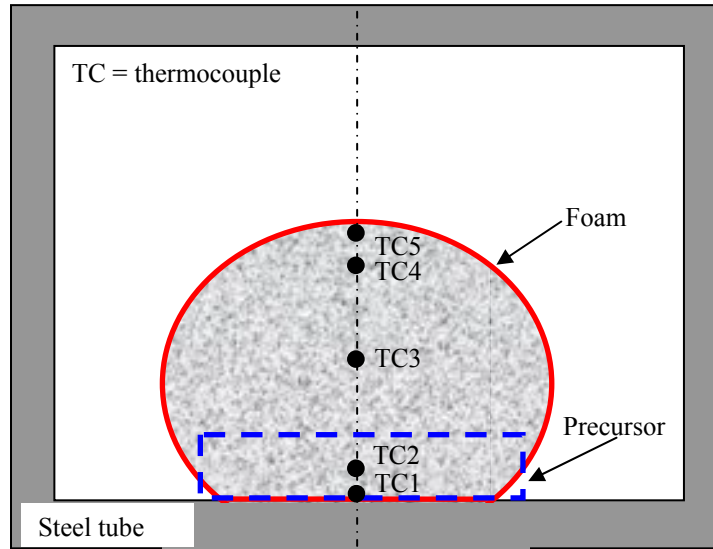


Figure 3.1. Schematic of temperature measurement scheme (not to scale). The black filled circles indicate positions of thermocouples. The starting position of the sample (precursor) is shown as dashed rectangle.

AlSi6Cu4 precursor was used for the calibration tests and natural cooling was employed. The foaming procedure was the same as described in section 2.3 except that two thermocouples were used. It was observed that after equilibration of temperature at both thermocouples, the inside temperature of the foam measured by TC3 and TC4 was about 20-25 K higher than the one measured by TC1. An example is shown in Fig. 3.2(a) where the temperatures measured simultaneously by TC1 and TC4 are shown. The TC4 temperature reaches a maximum of 650 °C before the expanding foam comes into contact with it. Radioscopic image sequences revealed the contact event; it is indicated in Fig. 3.2(a). After this, the TC4 temperature comes down and becomes stabilized at about 23–24 K above the TC1 temperature.

After about 550 s cooling starts and the temperature starts to decrease as seen in the cooling part of the temperature curves. Hereafter the cooling part of the temperature curve will be mentioned as *cooling curve*. Cooling curves of TC1, TC2, TC3, TC4 and TC5 show three kinks; these are related to the phase transformation in the alloy occurring during solidification. This will be discussed later more in detail in section 4.1.1. The first derivative ($\Delta T/\Delta t$, where T = temperature and t = time) of the cooling curves produces temperature arrest peaks corresponding to each of the kinks. Fig. 3.2(b) shows examples of such temperature arrest peaks for TC1 and TC4. Negative values of the first derivative indicate cooling. Henceforth the first derivative of the cooling curve will be mentioned as *cooling rate curve*. The start of each temperature arrest peak is referred to as minimum of that peak. It can be seen that the moment of the minima in the cooling rate curve of TC1 nearly coincides with that of the corresponding minima of the cooling rate curve of TC4. Similarly, the minima of the cooling rate curve of TC1 also nearly coincide with those of TC2, TC3 and TC5; the maximum time deviation observed was ± 1 s. The corresponding temperatures of all the minima are listed in Table 3.1.

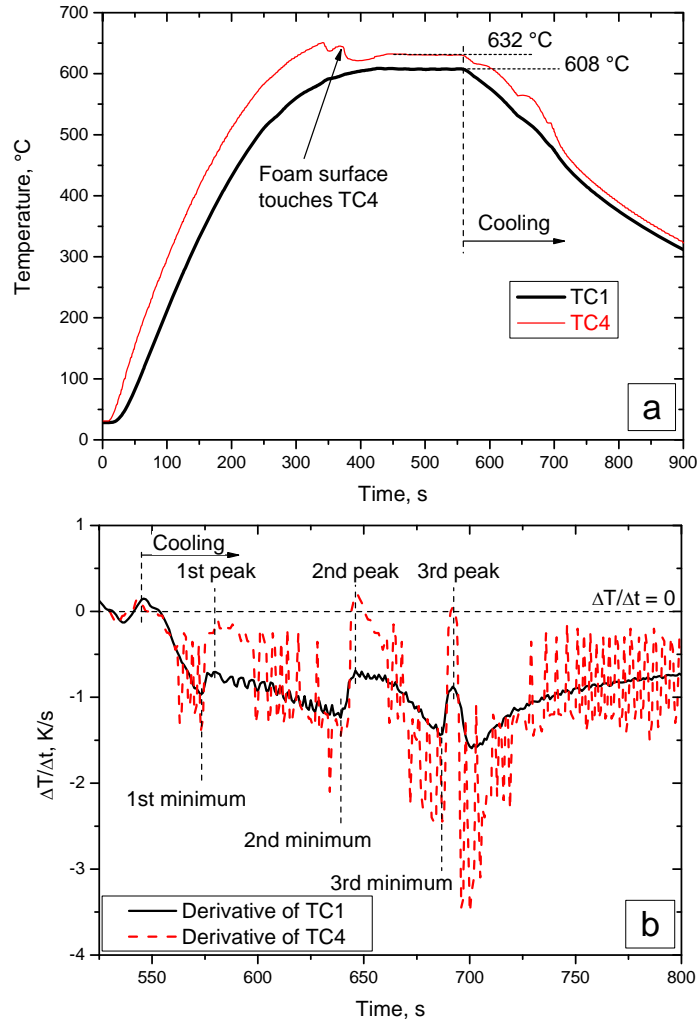


Figure 3.2. (a) Temperature as a function of time measured at two different positions in a AlSi6Cu4 alloy during foaming. TC1 corresponds to the outer bottom surface temperature of the foam, while TC4 represents temperature at a depth of ~3 mm from the outer surface of the foam (see Fig. 3.1). Temperature set point is 600 °C and the temperature was controlled with the TC1 thermocouple. (b) The first derivative of the temperatures measured by TC1 and TC4. The positions of the temperature arrest peaks and minima are indicated.

The inside temperatures of AlSi7, AlSi11, AlCu13Mg4 and Al alloy foams were also measured by inserting a thermocouple through the centre of the bottom surface of the precursor at a height of 3 mm. As a result, in the expanded foam the position of the thermocouple was 3 mm inside from the outer surface. This position is similar to the thermocouple TC4 in Fig. 3.1. Therefore, this thermocouple will also be referred as TC4. The first three alloys (in Fig. 3.3(a)) were foamed inside lamp furnace, whereas for Al the pressure furnace was used. The temperatures are shown in Fig. 3.3(a). It can be seen that the heating and cooling rates are higher for Al than those of other alloys. An enlarged view of the rectangle-marked part of each cooling curve is shown in Fig. 3.3(b). In case of Al, cooling is shown from 700 °C. The cooling curve of AlSi6Cu4 shows three kinks whereas for AlSi7 and AlSi11 alloy just two kinks can be seen. The cooling rate curves (not shown here) show temperature arrest peaks corresponding to each of the kinks. Although for AlCu13Mg4 only

two kinks can be observed in Fig. 3.3(b), the cooling rate curve reveals a small transient peak in-between two major temperature arrest peaks. This alloy shows 9 K temperature rise at 486 °C during cooling. This temperature increase behaviour is consistent in all experiments and the value measured by the TC1 thermocouple is 2–3 K. The corresponding temperatures of the minima of all alloys are given in Table 3.2.

Table 3.1

Temperatures of the minima of the three temperature arrest peaks in the cooling rate curve of AlSi6Cu4 alloy foam measured at different positions

Position of thermocouple (TC)	Temperature (°C)		
	1st minimum	2nd minimum	3rd minimum
TC1	597.9	533.8	490.7
TC2	604.5	555.1	512.2
TC3	617	571.2	523.5
TC4	619.9	566.4	524.4
TC5	613.1	556.4	514

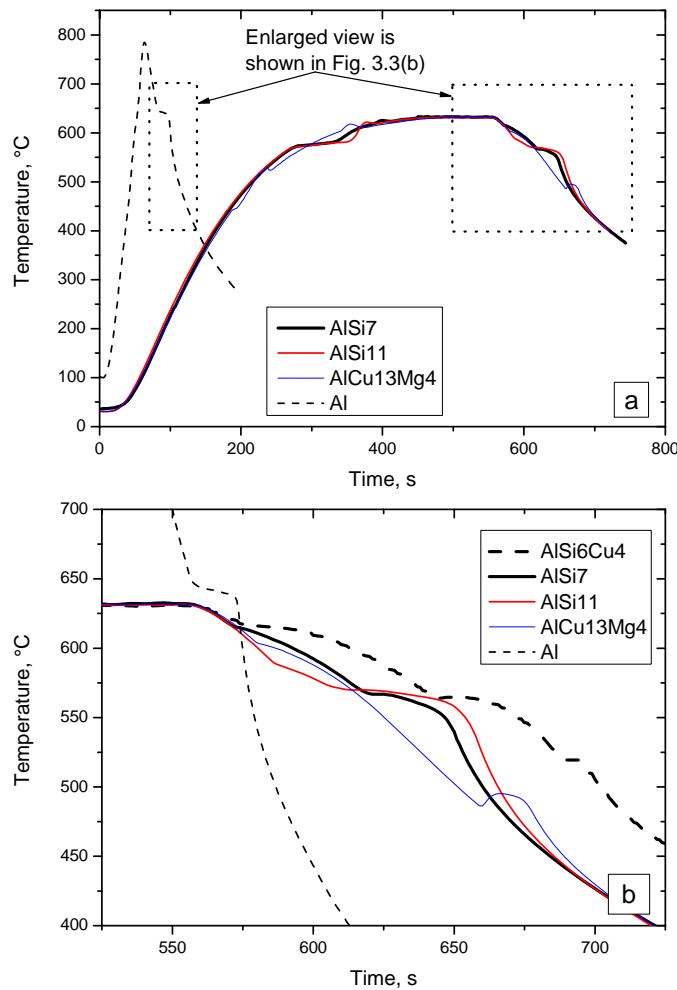


Figure 3.3. (a) The temperatures measured ~3 mm inside (i.e., by TC4 thermocouple) from the outer surface of different foams. (b) An enlarged view of the rectangle-marked parts of Fig. 3.3(a) and cooling curves of AlSi6Cu4.

3.2 Foaming process

The foaming procedure was similar for all the alloys (except Al) containing blowing agent. A typical foaming process is explained here for AlSi6Cu4 alloy (containing blowing agent). Foaming was carried out using the lamp furnace. Area expansion (i.e., A/A_0 , see section 2.2.4) behaviour and temperature profile are shown in Fig. 3.4(a) for a 100 s HT experiment. Natural cooling was employed to solidify the foam. The radioscopic images of different stages are shown in Fig. 3.5. The time and expansion corresponding to each image are indicated.

Table 3.2

Temperatures of the minima in different alloys measured by TC1 and TC4

Alloy	Thermocouple position	Temperature (°C)		
		1st minimum	2nd minimum	3rd minimum
AlSi6Cu4	TC1	597.9	533.8	490.7
	TC4	619.9	566.4	524.4
AlSi7	TC1	595.7	547.6	–
	TC4	618	572.4	–
AlSi11	TC1	557	548.3	–
	TC4	597	574.3	–
AlCu13Mg4	TC1	583	503	477
	TC4	606	521.5	493.3
Al	TC1	Not measured	–	–
	TC4	661	–	–

Three stages of foaming (heating, holding and cooling) have already been described in section 2.3; they are shown in Fig. 3.4. A small expansion can be observed from time 0 s up to point **1** ($T = 503$ °C). After this, the expansion curve forms an edge and the expansion rate changes drastically. Radioscopic images in between point **1** and **2** reveal the appearance of small protrusions at the outer contour of the precursor as shown by the image at 206 s in Fig. 3.5. These protrusions then disappear after a few seconds; see image at 220 s in Fig. 3.5. At point **2** ($T = 540$ °C) and **3** ($T = 589$ °C) the change in expansion slope can be observed.

In the cooling stage the foam begins to shrink, which is indicated by the decreasing value of A/A_0 . Fig. 3.4(b) represents the area expansion behaviour as a function of temperature. Three stages of foaming can be correlated directly with the temperature course of foaming. The vertical rise in area expansion at constant temperature indicates the holding stage. The area expansion curve in Fig. 3.4(a) reveals that foam starts to shrink soon after cooling starts. However, after some time of cooling, the expansion curve indicates an

intermediate expansion stage followed by further shrinkage. This expansion is indicated in Fig. 3.4(a) and (b).

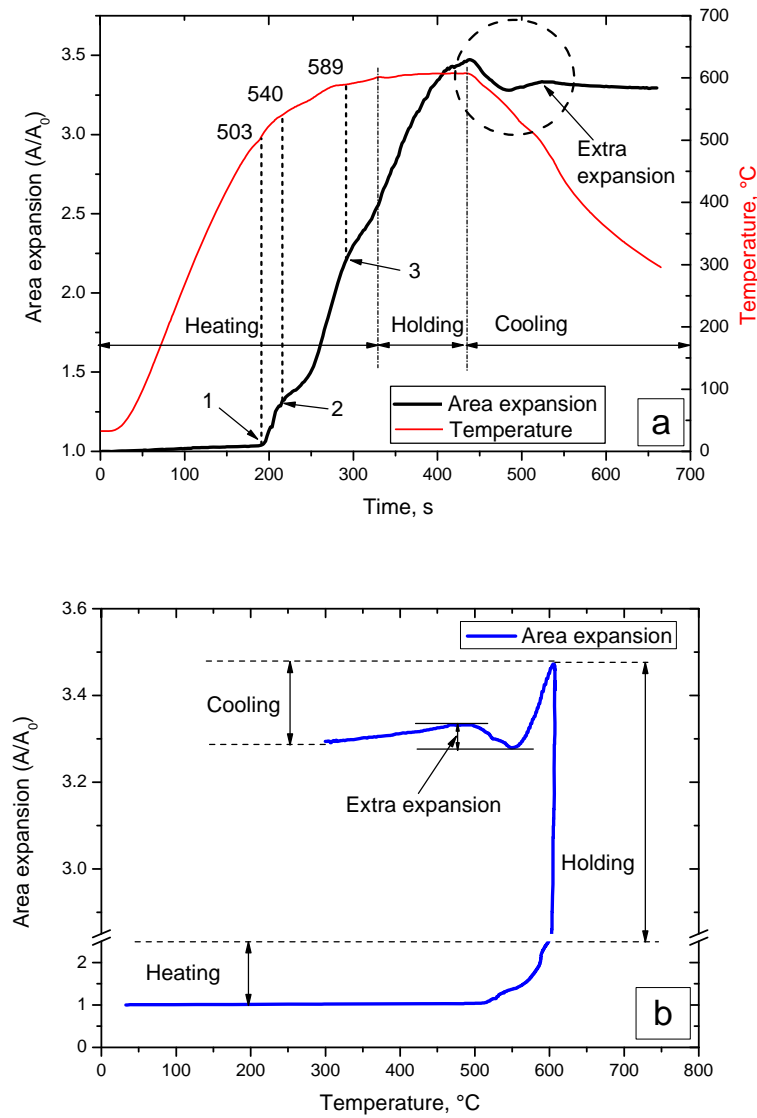


Figure 3.4. (a) Area expansion and temperature (measured by TC1 thermocouple) as a function of time for foaming of AlSi6Cu4 alloy showing three stages – *heating*, *holding* and *cooling*. *Holding time* is 100 s followed by natural cooling. (b) Area expansion as a function of temperature for the same experiments as in (a). The cooling part of the area expansion curve in both (a) and (b) shows extra expansion.

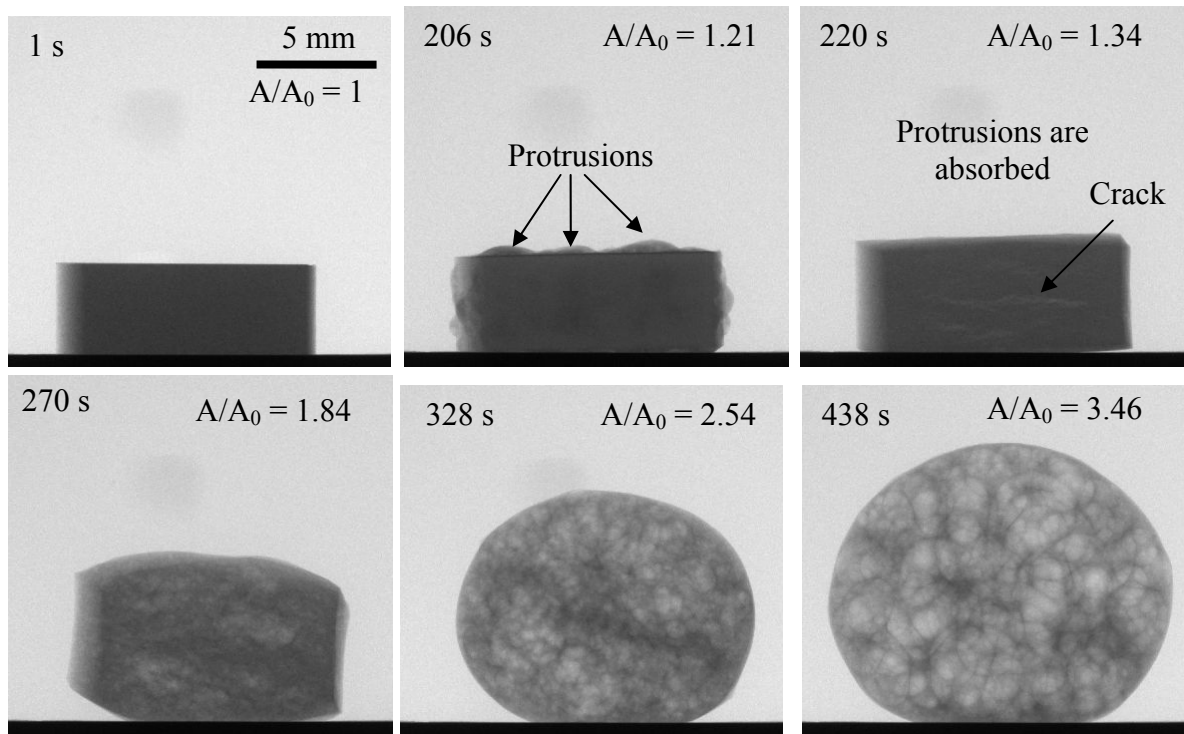


Figure 3.5. Radioscopic images of different stages of foam expansion. Time shown in each image corresponds to the time in Fig. 3.4(a). The corresponding area expansion values (i.e., A/A_0) are indicated. The image of the sample corresponding to 1 s is for the initial precursor. Images at 328 and 438 s correspond to the time of reaching 600 °C and maximum expansion, respectively.

3.3 Anomalous behaviour during solidification

3.3.1 Anomalous expansion or *extra expansion*

An enlarged view of the circle-marked part of the expansion curve in Fig. 3.4(a) is shown in Fig. 3.6. Points of interest (of the expansion curve) are labelled by numbers and indicated with arrows. Point **1** indicates the start of cooling. In a few seconds the foam begins to shrink. Careful observation reveals that at point **2** the slope of the expansion curve changes slightly. The change in slope is not as prominent as other features of the expansion curve; however, it is present in the expansion curve of all the experiments. Foam continues shrinking up to point **3** ($A_{\min,1}/A_0$), after which the foam expands instead shrinking. The expansion continues up to point **6** ($A_{\max,2}/A_0$) followed by shrinkage for the remaining cooling stage. This transient expansion from point **3** to **6** is an *anomalous behaviour* considering the fact that foam should shrink during cooling as a result of temperature drop. This anomalous expansion is an extra addition to the normal expansion of the foam and that is why it is denoted as *extra expansion*.

(EE). The value of EE is given by the difference in values in A/A_0 from point **6** to **3** and expressed as percentage, i.e., $\{(A_{\max,2} - A_{\min,1})/A_0\} * 100\%$. The value of EE in Fig. 3.6 (or in Fig. 3.4(a) and (b)) is 5.4%. It can be seen in Fig. 3.6 that EE stage has kinks at points **4** and **5** and hence can be divided into two stages – the first from point **3** ($A_{\min,1}/A_0$) to **4** ($A_{\max,1}/A_0$) and the second one is from point **5** ($A_{\min,2}/A_0$) to **6** ($A_{\max,2}/A_0$). The first and second subdivisions of EE are referred to as EE1 and EE2, respectively. They are expressed as follows

$$EE1 = \left(\frac{A_{\max,1} - A_{\min,1}}{A_0} \right) * 100\% \quad 3.1$$

$$EE2 = \left(\frac{A_{\max,2} - A_{\min,2}}{A_0} \right) * 100\% \quad 3.2$$

If $A_{\max,1}/A_0 = A_{\min,2}/A_0$ (e.g. in Fig. 3.6), then total $EE = EE1 + EE2$. In some cases $A_{\max,1}/A_0 \neq A_{\min,2}/A_0$. In those cases, total $EE \neq EE1 + EE2$.

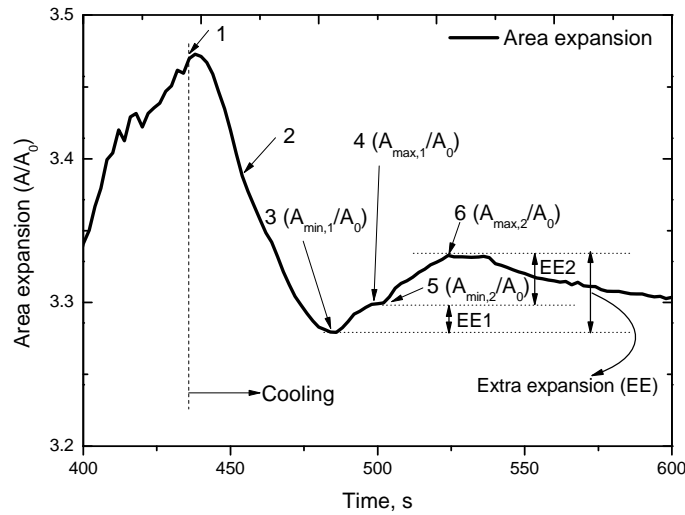


Figure 3.6. An enlarged view of the encircled part of the expansion curve in Fig. 3.4(a). An expansion stage (*extra expansion* or EE) is present in the cooling stage of the expansion curve. Interesting points are labelled by numbers and explained in the text. Extra expansion 1 (EE1) and extra expansion 2 (EE2) are indicated.

3.3.2 Cooling curve of foaming

An enlarged view of the encircled part of the temperature curve in Fig. 3.4(a) and the first derivative ($\Delta T/\Delta t$) of the same are shown in Fig. 3.7. Interesting points of the cooling rate curve—i.e., $\Delta T/\Delta t$ of the cooling curve—are labelled with numbers. Point **7** indicates the beginning of cooling. Cooling rate increases—i.e., $\Delta T/\Delta t$ decreases—up to point **8**. It can be seen that there are three temperature arrest peaks in the cooling rate curve (peaks and

minima of a cooling rate curve have already been described in Fig. 3.2(b)). Points **8**, **9** and **10** indicate the minimum (i.e., the starting points of the temperature arrest peaks) of the first, second and third peak, respectively. The cooling rate reaches maximum at point **11**, after which it decreases slowly and approaches zero as temperature decreases to room temperature. The corresponding temperatures of the first, second and third minima are 592 °C, 532 °C and 487 °C, respectively.

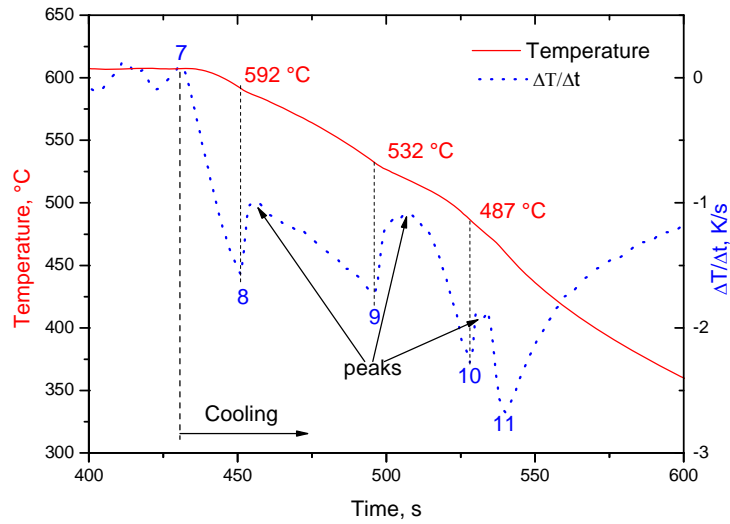


Figure 3.7. Temperature as measured with TC1 thermocouple (encircled part of Fig. 3.4(a)) and first derivative ($\Delta T/\Delta t$) of temperature curve against time. The corresponding temperatures of the minimum of each temperature arrest peak are indicated.

3.3.3 Cooling rate curve and *extra expansion*

Fig. 3.8 is a combination of the expansion curve of Fig. 3.6 and the cooling rate curve of Fig. 3.7. The interesting points of both curves are indicated. It is observed that the first minimum (point **8**) of the cooling rate curve is followed by the change in slope in the expansion curve (point **2**). EE1 (point **3** to **4**) falls approximately in-between the first (point **8**) and second (point **9**) minimum whereas EE2 (point **5** to **6**) is situated approximately in-between the second (point **9**) and third (point **10**) minimum. Hereafter, the EE that is located in-between the first and second minima will be referred to as EE1, while the EE appearing after the second minimum will be referred to as EE2. In future, this convention will be followed for AlSi6Cu4 and all other alloys as well. It should be noted here that in some cases there are 1-2 seconds time mismatch between temperature and expansion curve. This is because temperature and foam evolution was recorded using different software, which were not synchronised.

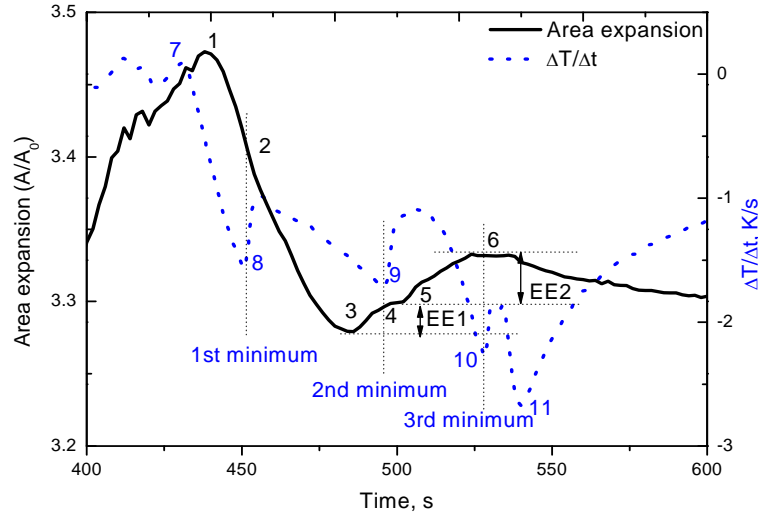


Figure 3.8. Area expansion (encircled part in Fig. 3.4(a)) and the corresponding first derivative ($\Delta T/\Delta t$) of the temperature (TC1) curve as a function of time. This figure combines Figs. 3.6 and 3.7 (without the temperature).

3.4 Holding time experiments

3.4.1 Results for AlSi6Cu4 alloy

Foaming of AlSi6Cu4 alloy was carried out for a number of *holding times* (HT), ranging from 0 to 3000 s, and using the lamp furnace. Heating and cooling procedures were similar in all cases. Natural cooling was employed at the end of the HT. Thermocouple position was TC1 (see Fig. 3.1). The area expansion (A/A_0) behaviour (solid line) and the corresponding temperature course (dashed line) of foaming for some HTs are shown as a function of time, see Figs. 3.9–11.

The area expansion curves for HT 50, 100 and 200 s are shown in Fig. 3.9(a). The various slope changes during the heating stage, as indicated by points 1, 2 and 3 in Fig. 3.4(a), can be seen. Maximum expansion is higher for higher HT. The starting point of EE in each case is indicated with an arrow. An enlarged view of the dashed-rectangle marked part of Fig. 3.9(a) is presented in Fig. 3.9(b). The two-stage behaviour of EE can be seen, especially for 200 s HT where it is prominent. The values of EEs as measured from the expansion curves are: EE1 = 1% and EE2 = 3.2% for 50 s HT; EE1 = 2% and EE2 = 3.4% for 100 s HT; and EE1 = 4.2% and EE2 = 3.1% for 200 s HT.

Fig. 3.10 shows the expansion behaviour and temperature course of AlSi6Cu4 foaming applying 400, 500 and 600 s HT. An enlarged view of the rectangle-marked position is shown in the inset. The starting points of EE1 and EE2 are indicated in the inset. EE1 and EE2 can be seen for 400 and 500 s HT, whereas in case of 600 s HT there is only EE2. Whether an EE is EE1 or EE2 was identified by following the aforementioned convention,

i.e., by matching its position with the positions of the minima in the cooling rate curve. In this way the EE observed for 600 s HT was identified as EE2. The edge in the A/A_0 curves (as indicated by the point 1 in Fig. 3.4(a)) in each case is offset from each other by several seconds. This is probably because of the accidental variation in the thermocouple (TC1) position, which leads to some difference in the temperature control and foam expansion starts at different times.

The foaming behaviour of AlSi6Cu4 for 1500, 2500 and 3000 s HT is presented in Fig. 3.11. The A/A_0 curves show expansion up to about 1000 s HT for each case. After this, A/A_0 decreases slightly for the rest of the HT period in case of 2500 s HT. In contrast, for 3000 s HT A/A_0 decreases slightly at the beginning and then shows a pronounced drop for the remaining HT. The cooling part of the expansion curve is similar for all HTs. The sudden drop in A/A_0 curve, marked by circles, in the case of 3000 s HT indicates rupture of bubbles at the outer surface of the foam. These ruptures were identified in the radioscopic image sequence. EE for each HT is indicated with arrow.

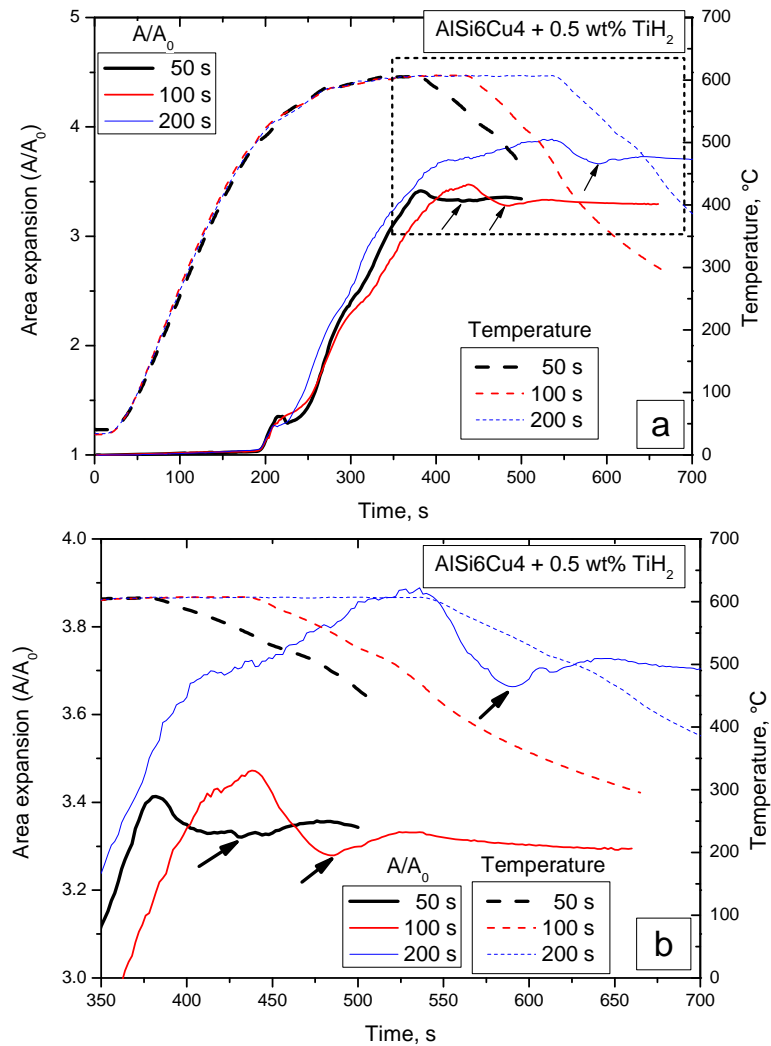


Figure 3.9. (a) Area expansion and temperature (measured by TC1 thermocouple) as a function of time for 50, 100 and 200 s HT. (b) An enlarged view of the dashed-rectangle marked part of Fig. 3.9(a). The arrows in (a) and (b) indicate the beginning of EE.

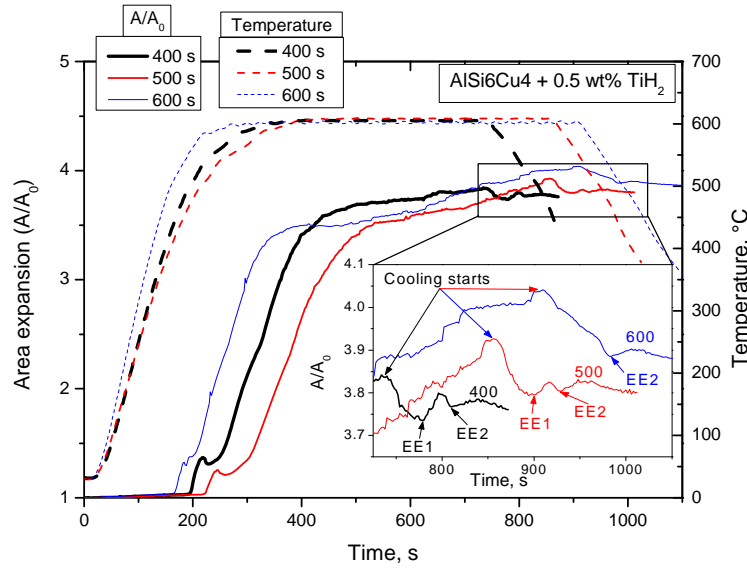


Figure 3.10. Area expansion and temperature (measured by TC1 thermocouple) as a function of time for AlSi6Cu4 alloy applying 400, 500 and 600 s HT. Inset shows the enlarged view of the A/A_0 curve marked with a rectangle. The beginning of EE1 and EE2 are indicated in the inset. The values of EE1 for 400 and 500 s are 6.5 and 2.5, respectively. The values of EE2 for 400, 500 and 600 s are 1.7%, 2.4% and 1.8%, respectively.

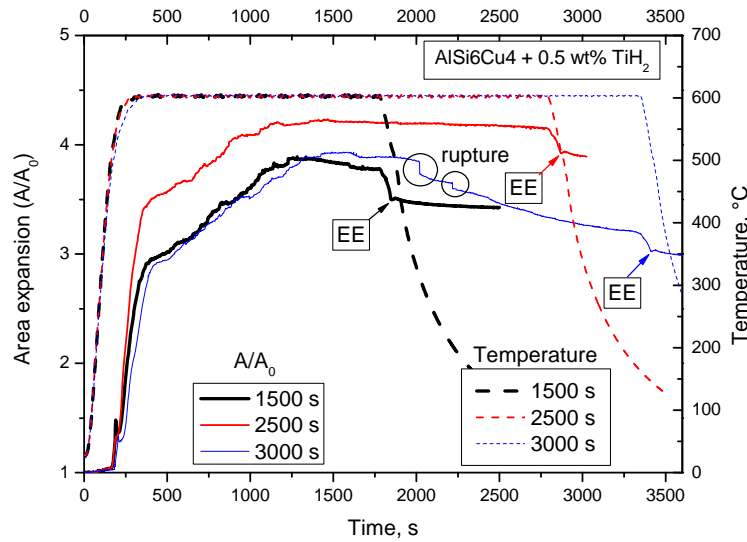


Figure 3.11. Foam area expansion and temperature (measured by TC1 thermocouple) as a function of time for AlSi6Cu4 alloy applying 1500, 2500 and 3000 s HT. The sharp drops, marked by circles, indicate rupture of bubble at the outer surface of the foam. The starting points of EE are indicated with arrows.

The shrinkage behaviour of foams after short (solid line) and long (dashed line) HT is compared in Fig. 3.12. The value of A/A_0 for all HT at the beginning of cooling is shifted to the same value to facilitate comparison. The data corresponds to Figs. 3.9 and 3.11. Foams with 50, 100 and 200 s HT do not shrink immediately after the onset of cooling. The samples with 50 s HT expands more than 100 and 200 s HT before finally begins to shrink. In the case

of experiments with longer HTs, foams show immediate shrinkage at the beginning of cooling. The slope of A/A_0 is higher for 200 s HT than for 50 and 100 s HT. The initial part of shrinkage for 1500, 2500 and 3000 s HT is similar. A/A_0 however, drops faster in case of 1500 s HT than for the other long-HT foams. Foams with HT longer than for HT = 200 s show less shrinkage than 200 s. Up to the beginning of EE the cooling part of the A/A_0 curves for 250–1500 s HT lies in-between 50 and 200 s. For all the longer-HT foams, starting from 600 s, the initial cooling part of the expansion nearly follows the trend shown by 1500, 2500 and 3000 s HT. The slope of the A/A_0 curves after the end of EE is same in all cases as can be seen for six HTs in Fig. 3.12.

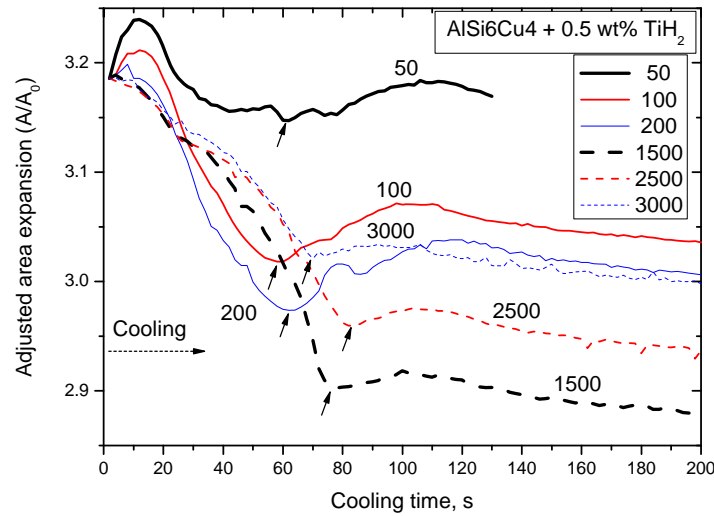


Figure 3.12. Area expansion as a function of cooling time for the cooling part of the expansion curve for AlSi6Cu4 applying short (50, 100 and 200 s) and long (1500, 2500 and 3000 s) HT. The value of A/A_0 for all HT at the beginning of cooling is set to the same value for matter of comparison. The beginning of EE is indicated by short arrows.

The interesting points of the cooling part of A/A_0 and cooling rate curve have already been shown in Fig. 3.8. The corresponding temperatures of those points can be extracted from the temperature curve. Similarly the corresponding temperature of the points **2**, **3**, **4**, **5**, **6**, **8**, **9** and **10** were extracted for AlSi6Cu4 for 0 to 3000 s HT and are shown in Fig. 3.13. Each data point is the average of 3–7 experiments, except for 50, 150, 250, 350, 450, 2000 and 3000 s HT that represents just a single experiment. For the sake of clarity error bars are not shown except for 500 s HT. Error bars for other HTs are in the similar range as those shown for 500 s HT.

It can be seen in Fig. 3.13 that the first minimum is followed by the change in slope in the expansion curve. EE1 is situated in-between the first and second minima, whereas EE2 appears in-between the second and third minima. No EE can be observed after the third minimum. This trend is similar as already shown for 100 s HT in Fig. 3.8. EE1 is seen up to 500 s HT; EE2 is present for all HT. For a particular HT all the different temperatures seem to

be shifted by almost the same value on the temperature axis. For example, the data points of 350 s HT are of higher magnitude than the corresponding data points of 400 s HT. The differences between EE1 start and end temperatures are smaller for short HTs; whereas, the differences between EE2 start and end appears to be nearly constant for all HT. It should be mentioned here that the experiments applying 50, 150, 250, 350 and 450 s HT were performed in a second set than the other HTs. The accidental slight variation in thermocouple (TC1) position (i.e., little more inside the sample) probably caused in higher temperature measurement in this set and resulted in zigzag behaviour in the temperatures in Fig. 3.13 . It has already been shown in section 3.1 that temperature measurement can vary significantly with the position of the thermocouple.

The values of EE1 and EE2 for AlSi6Cu4 are shown in Fig. 3.14 for 0 to 3000 s HT. Statistics of data points are similar to that for Fig. 3.13. The error bars represent the standard deviation. EE1 can be seen up to 500 s HT. EE1 increases rapidly up to 200 s HT. Although there is some fluctuation in the EE1 value between 200 and 450 s HT, it is nearly constant if one considers the error bars. EE decreases after 450 s HT and no EE can be seen for longer HTs than 500 s. On the other hand, EE2 is present for all HT. It increases from 0 to 50 s HT and then shows a gradual decreasing trend till 600 seconds beyond which it is almost constant for even longer HTs. A mean value of 1.5% was obtained by considering all the averaged values of EE2 from 600 to 3000 s HT. The error bars for EE2 are smaller than that those for EE1.

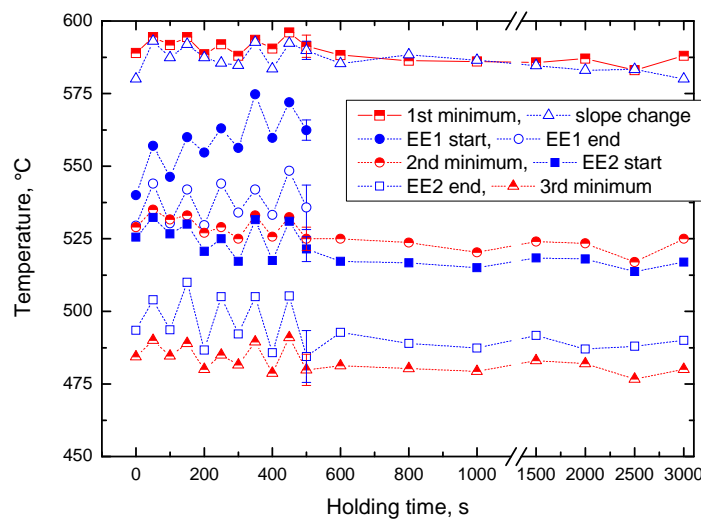


Figure 3.13. Corresponding temperatures (measured by TC1 thermocouple) of the points **2, 3, 4, 5, 6, 8, 9** and **10** of Fig. 3.8. Average values are shown for foaming of AlSi6Cu4 for 0 to 3000 s HT. Except for 500 s HT error bars are avoided for the sake of clarity. The lines through the data points only serve as a guide to the eye.

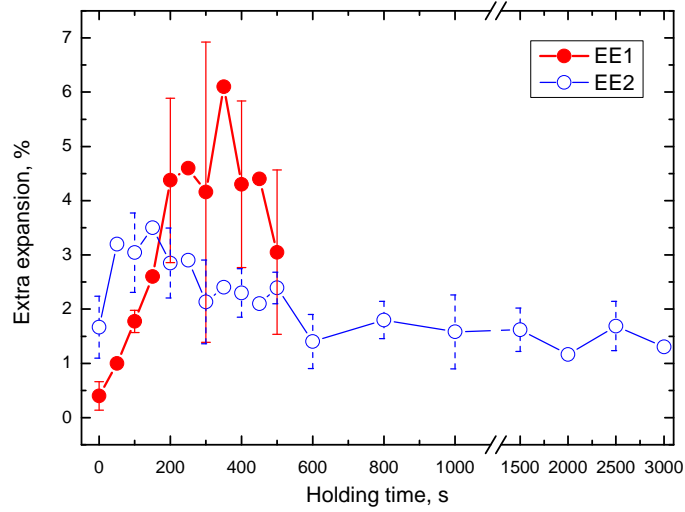


Figure 3.14. EE1 and EE2 as a function of holding time for AlSi6Cu4 alloy. All the experiments were performed with natural cooling. Average cooling rates during EE1 and EE2 are ~ 1.3 – 1.4 and 1.1 K/s, respectively. The error bars represent the standard deviation. The lines through the data points only serve as a guide to the eye.

It was observed that the time taken during EEs is not same in all experiments. The time period range for EE1 is 4 to 30 s with low time for short HT. For EE2 the time period range is 16–44 s for 0–500 s HT, and 20–30 s for longer HT. The time-normalized values of all the EEs are presented in Fig. 3.15 as a function of HT. Comparison of Figs. 3.14 and 3.15 suggests that the general trend is similar in both figures.

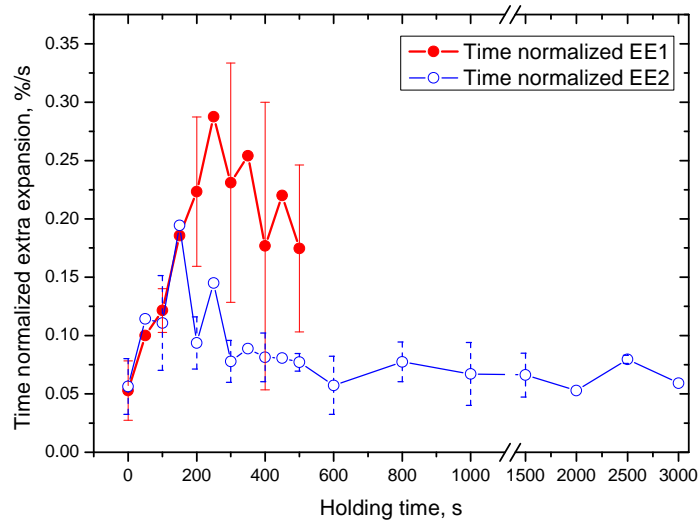


Figure 3.15. Time-normalized extra expansion as a function of holding time for AlSi6Cu4 alloy. Each value in Fig. 3.14 was normalized by their respective time of duration. The error bars represent the standard deviation. The lines through the data points only serve as a guide to the eye.

3.4.2 Results for AlSi7 alloy

The foaming behaviour of AlSi7 alloy is shown in Fig. 3.16(a) for 100 and 200 s HT. Foaming was performed using the lamp furnace, and natural cooling was employed. During the heating stage and up to 100 s HT both show similar behaviour. The beginning of EE is indicated by arrows. Like AlSi6Cu4, AlSi7 also shows two stages of EE, i.e., EE1 and EE2. EE1 and EE2 and their time-normalised values for 50, 100 and 200 s HT are given in Fig. 3.16(b). EEs and normalised EEs show a similar trend and the same behaviour as found for AlSi6Cu4. AlSi7 alloys show two temperature arrest peaks in their cooling rate curve, see Table 3.2. EE1 can be found in-between the first and second minima, and EE2 appears after the second minimum. The correlation between the positions of the EEs and the minima of $\Delta T/\Delta t$ curve is identical to that seen for AlSi6Cu4, see Fig. 3.13.

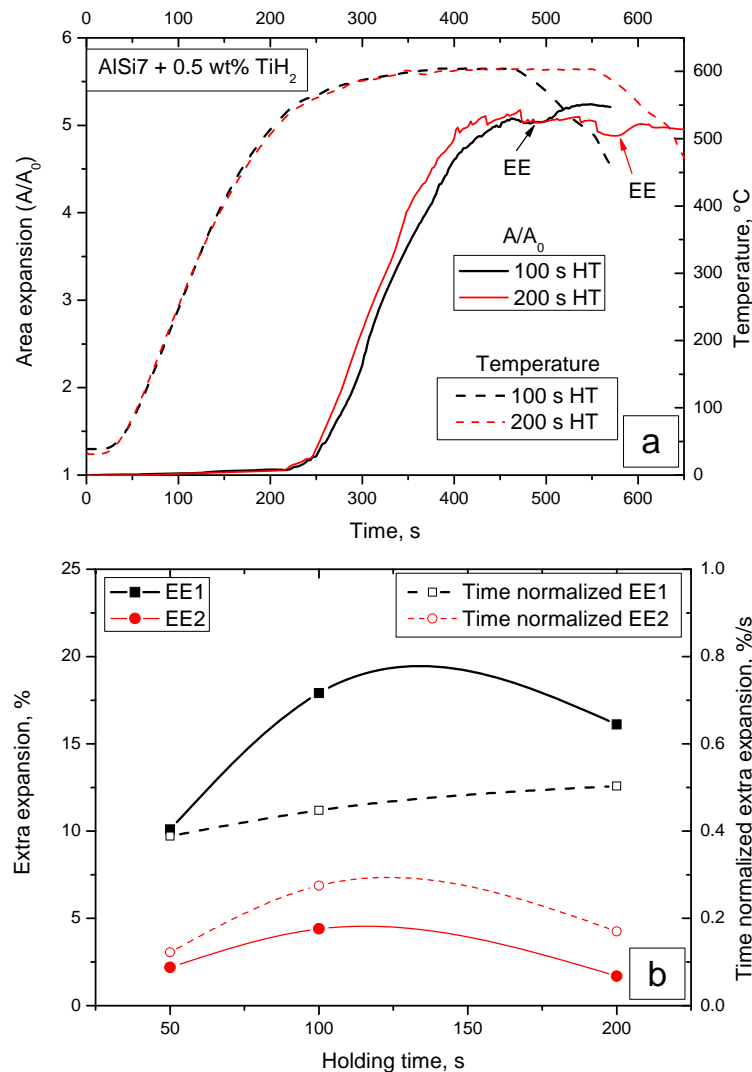


Figure 3.16. (a) Area expansion behaviour and temperature course as a function of time for AlSi7 alloy. The beginning of EE is indicated by arrows. (b) EEs and their time-normalized values vs. holding time. The lines through the data points only serve as a guide to the eye.

3.4.3 Results for other alloys

Fig. 3.17 shows the expansion behaviour of AlSi11 alloy foam. At higher holding time, i.e., 200 s, some large bubbles rupture at the outer surface of the foam. Those are marked by dotted ellipses. A magnified view of the cooling part of the A/A_0 curve for 0 s HT is shown in the inset. EE1 and EE2 are indicated; their respective values are 1.3 and 3.2%. The cooling rate curve (not shown here) of 0 s HT shows two temperature arrest peaks. The temperatures (TC1) of the minima are 570 °C (first) and 531 °C (second). The corresponding positions in the expansion curve are marked in the inset. It can be seen that EE1 is situated in-between the first and second minima, while EE2 appears after the second minimum. This is identical behaviour as already seen for AlSi6Cu4 and AlSi7 alloy. Fig. 3.17 shows that the foam shrinkage begins immediately after the cooling starts for 50 and 200 s HT, whereas for 0 s HT the foam continues to expand for a short time even after cooling. The fluctuations in the 50 s HT expansion curve (marked by dotted squares) are the result of contrast problems in the radioscopic images as described in section 2.2.4.

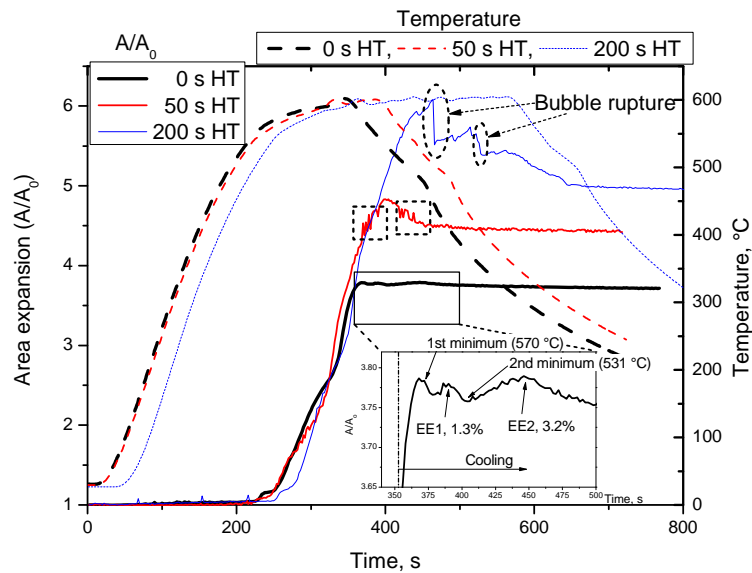


Figure 3.17. Area expansion and temperature (measured by TC1 thermocouple) as a function of time for AlSi11 alloy applying 0, 50 and 200 s HT. The sharp drops, marked by dotted ellipses, are result of outer surface bubble rupture. A magnified view of the expansion curve for 0 s HT (marked by solid rectangle) is shown in the inset. Corresponding positions of the minima in the cooling rate curve ($\Delta T/\Delta t$) are indicated in the A/A_0 curve for 0 s HT.

Expansion behaviour and the temperature profile of AlCu13Mg4 foam (for 200 s HT) and Al foam (for 0 and 100 s HT) are shown in Figs. 3.18 and 3.19, respectively. AlCu13Mg4 does not show any EE for any HT under natural cooling. In case of Al, EE was observed in some experiments. However, the effect is so small that AXIM cannot resolve this transient stage reliably and EE can only be seen by visual inspection of the radioscopic images representing the cooling stage. By means of visual comparison the EE in Al foam appears

smaller than the constant value of EE2 (i.e., for HT of 600 s and longer values) in AlSi6Cu4 alloy. However, no definitive value can be assigned to it. For 0 s HT Al foam does not show shrinkage at the beginning of cooling; an identical behaviour has been shown for AlSi11 alloy, see Fig. 3.17. Al was foamed in the pressure furnace. Consequently, the foaming temperature shown for Al was not measured on the sample but represents the temperature of the bottom surface of the ceramic heater; for details see section 2.2.2. The natural cooling rate in the pressure furnace is higher than in the lamp furnace. A cooling rate of about 9 K/s was measured above 660 °C when thermocouple was inserted inside the sample (i.e., in TC4 position), see Fig. 3.3 for the respective temperature curve.

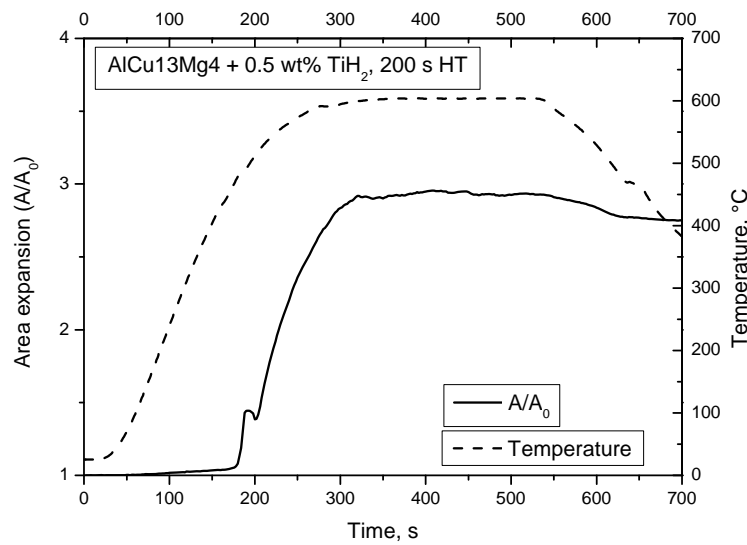


Figure 3.18. Area expansion and temperature (measured by TC1 thermocouple) as a function of time for foaming of AlCu13Mg4 alloy applying 200 s HT.

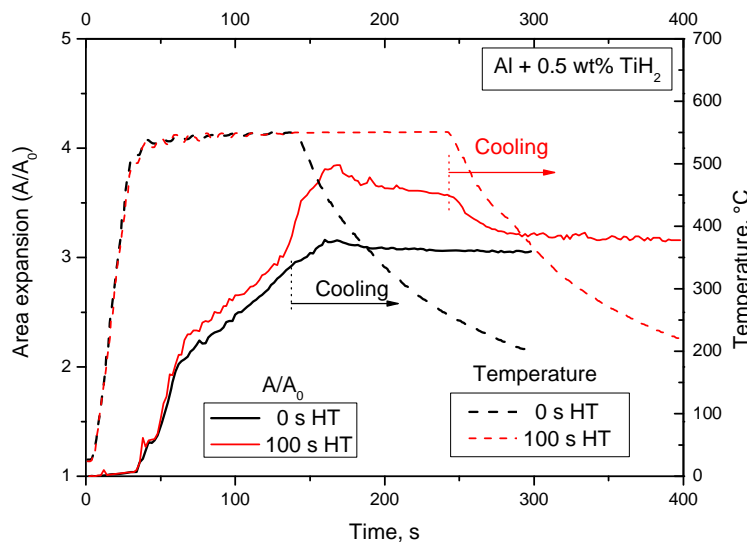


Figure 3.19. Area expansion and temperature (measured at the bottom surface of the heating plate) as a function of time for Al foaming applying 0, 100 s HT. Foaming was performed in the pressure furnace.

Zinc with 0.6 wt.% untreated TiH_2 was foamed using the lamp furnace at 430 °C and natural cooling was employed. One EE was observed during the cooling stage of Zn foam. The typical value under natural cooling (cooling rate 1 K/s) is 5.9% for 50 s HT. No systematic study was carried out in this system.

3.5 Cooling rate experiments

Different slow cooling rates were achieved by reducing the power of the lamps from 300 W to various lower values instead of turning them off completely. As a result, the cooling rate is not constant over the total cooling stage. An automatic ramp of the controller would provide better control on cooling rate. However, that was avoided; the reason will be discussed later. It was observed that for slower cooling rates (than the natural cooling rate) the value of EE1 is much higher than that of EE2. Higher value of EE1 facilitates to identify the variation in its value with changing cooling rates. That is why EE1 was chosen to study the effect of cooling rate on its value. The control of the cooling rate was performed only in the temperature regime of EE1. It has already been stated that EE1 was observed in-between the first and second minima (of the $\Delta T/\Delta t$ curve) in both AlSi6Cu4 and AlSi7 alloys. So, during cooling the power of the lamps was controlled only up to the temperature corresponding to the second minimum of the $\Delta T/\Delta t$ curve. All cooling rates mentioned in this section correspond to the average cooling rate determined from the temperature curve measured by TC1 thermocouple during EE1.

3.5.1 Results for AlSi6Cu4 alloy

The expansion of slowly cooled AlSi6Cu4 foams after 200 s HT is shown in Fig. 3.20. The given cooling rates (mentioned in the legends) represent the average cooling rates during EE1. Cooling was performed by reducing the power of the lamps from 300 to 180 W leading to an average cooling rate of 0.29 K/s. An enlarged view of the rectangle marked part of the A/A_0 curve (in the regime of EE1) is shown in the inset. The respective values of EE1 are 29.9%, 34.4% and 24.8% for 0.28, 0.31 and 0.27 K/s cooling rate. These values of EE1 are higher compared to those obtained during natural cooling, see Fig. 3.14. The values of A/A_0 at the end of EE1 are higher than those achieved at the end of the holding stage for 0.28 and 0.27 K/s cooling rates. This means that the more than the foam area immediately before the onset of cooling can be achieved. The drop in expansion values marked by circle resulted from an outer surface bubble rupture.

Fig. 3.21 shows A/A_0 and the temperature (measured by TC1 thermocouple) profile in the cooling region for foaming of AlSi6Cu4 applying 200, 400 and 600 s HT. Cooling was achieved by reducing the power of the lamps from 300 to 113 W. The resulting average cooling rate is 0.6 K/s. EE1 is the highest for 200 s HT. The initial shrinkage gradient for 600

s HT is shown and superimposed on the A/A_0 curves for 200 and 400 s HT. 200 s HT leads to the highest amount of shrinkage before EE1 starts. The shrinkage for 400 s HT has an intermediate value. This result is in agreement with that mentioned in the context of Fig. 3.12: Longer HTs than 200 s lead to less shrinkage during cooling. EE1 and their respective time-normalized values in AlSi6Cu4 for three cooling rates and three HTs are compared in Fig. 3.22. EE1 decreases with increasing cooling rate for each HT. In contrast, for a given HT the time-normalized EE1 appears to be almost constant. While for 200 s HT EE1 decreases significantly with increasing cooling rate, the time-normalized EE1 almost remain constant if one considers the error bars.

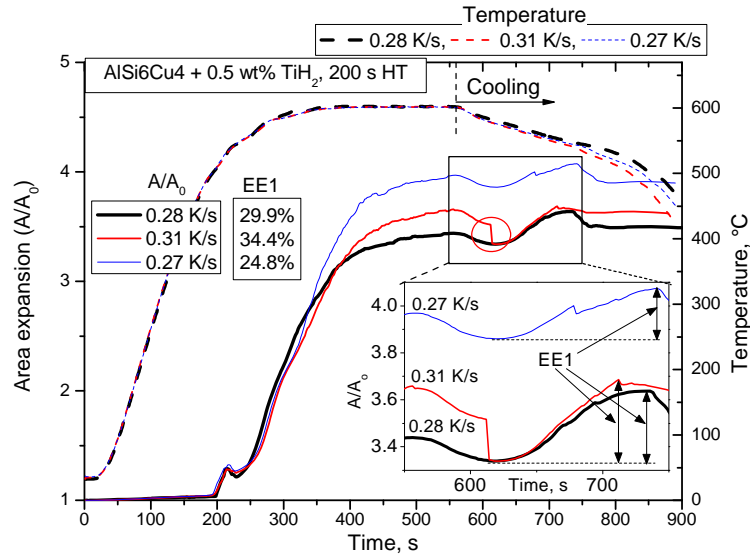


Figure 3.20. Expansion and temperature (measured by TC1 thermocouple) curve for 200 s HT and slow cooling AlSi6Cu4 alloy foams. The cooling rates in the legends represent the average cooling rate measured from the TC1 temperature curve during EE1. EE1s are enlarged in the inset. The circle indicates an outer surface bubble rupture.

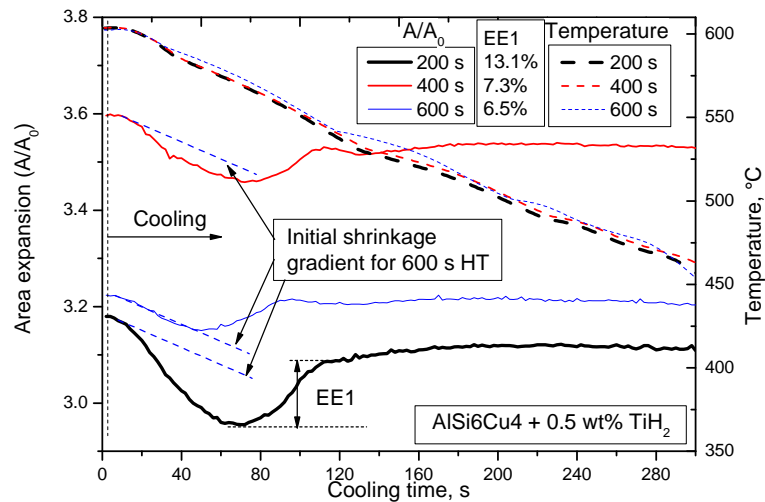


Figure 3.21. Cooling part of the area expansion and temperature (measured by TC1 thermocouple) as a function of cooling time for 200, 400 and 600 s HT. Cooling rate during EE1 is 0.64, 0.6 and 0.59 K/s for the 200, 400 and 600 s HT experiments, respectively. Cooling in each case was performed by reducing the power of the lamps from 300 to 113 W. Different cooling rates were measured due to accidental variations.

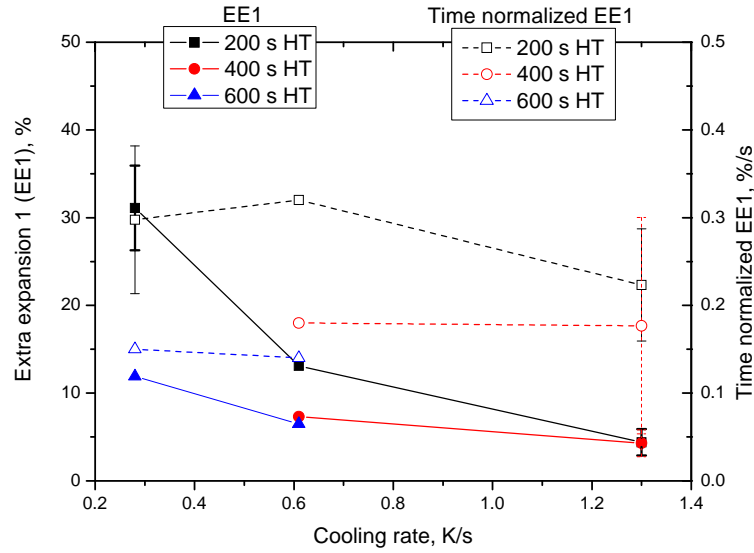


Figure 3.22. EE1 and time-normalized EE1 in AlSi6Cu4 as a function of cooling rate for three holding times. Foaming with the slowest cooling rate was not performed for 400 s HT. Error bars represent standard deviation. Data points without any error bar are just for a single experiment. The lines through the data points only serve as a guide to the eye.

EE1 is visualized by radiosopic imaging in Fig. 3.23. These images correspond to the results shown in Fig. 3.20. Top row and bottom rows are for 0.31 and 0.28 K/s, respectively. The time in each image corresponds to the time in Fig. 3.20. The change in heights during cooling and EE1 are indicated by lines. The increase in height due to EE1 can be clearly seen from the images. For the cooling rate of 0.28 K/s the value of A/A_0 is higher than that at the beginning of cooling.

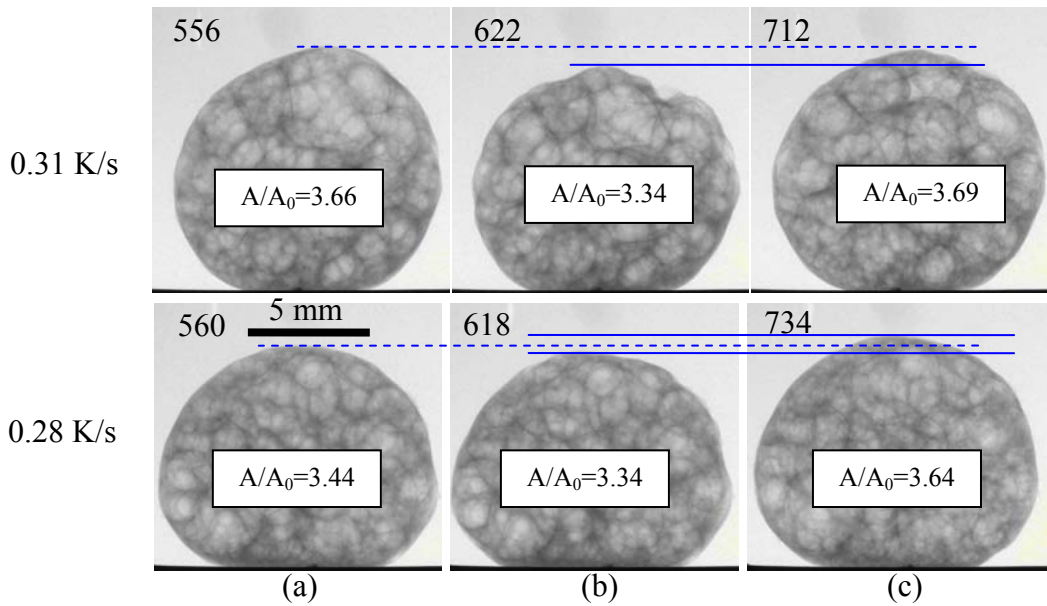


Figure 3.23. Radiosopic images acquired during cooling. Images correspond to the beginning of cooling (a), beginning of EE1 (b) and end of EE1 (c). The lines indicate the apparent increase in height due to EE. Numbers in each image indicate time and corresponds to the time in Fig. 3.20. The corresponding A/A_0 values are specified.

3.5.2 Results for AlSi7 alloy

AlSi7 alloy was foamed for a fixed HT (100 s) using six different cooling rates each being slower than natural cooling rate. The power supply of the lamps was reduced from 300 W to 151, 136, 113, 88, 59 and 18 W to achieve different cooling rates. The expansion behaviour representing two sets of measurement (300 to 136 and 300 to 59 W) is given by Figs. 3.24 and 3.25. The individual cooling rates in each experiment is given in the legends. Corresponding EE1 values are also indicated. The average value of EE1 for the cooling rate corresponding to 300 to 136 W cooling is higher than that for the cooling rate corresponding to 300 to 59 W cooling. The value of EE1 increases with decreasing cooling rate. This is in agreement with the results shown in Fig. 3.22. All cooling rates were calculated based on the data measured by TC1 thermocouple (see Fig. 3.1). In order to find out the real temperature profile inside the foam temperature was measured by a TC4 thermocouple for three cooling rates corresponding to 300 to 136 W, 300 to 59 W and natural (i.e., 300 to 0 W) cooling. The temperature profiles are given in Fig. 3.26. The corresponding cooling rates during EE1 calculated from the temperature measured by TC1 are about 1.28, 0.93 and 0.48 K/s for natural, 300 to 59 W and 300 to 136 W cooling, respectively.

The shrinkage as a function of temperature behaviour of AlSi7 alloy foams for five different cooling rates is shown in Fig. 3.27. HT for each experiment is 100 s. The cooling rate (measured by a TC1 thermocouple) during EE1 is shown in the legend. The value of EE1 changes with cooling rate. The respective values of EE1 are given beside their legends. Foams with lower cooling rate seem to have higher shrinkage after the end of EE1. Few outer surface bubble ruptures can be seen in these foams by the sudden drops (indicated with circles) in the A/A_0 value. The ruptures were verified from the radioscopic image sequences.

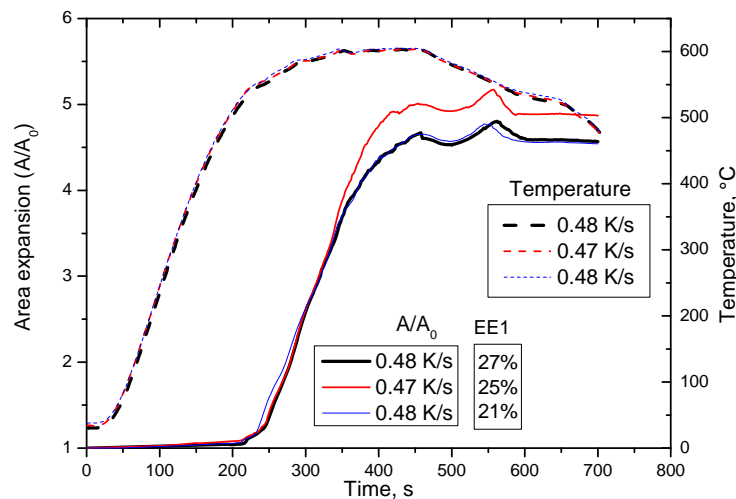


Figure 3.24. Area expansion and temperature (measured by TC1 thermocouple) profile of AlSi7 foaming for three cooling rates. For each experiment HT is 100 s. Cooling rates indicated in the legends correspond to the average cooling rate measured from the TC1 temperature curve during EE1. Cooling in each case was performed by reducing the power of the lamps from 300 to 136 W. Different cooling rates were measured due to accidental variations. The value of EE1 in each experiment is shown.

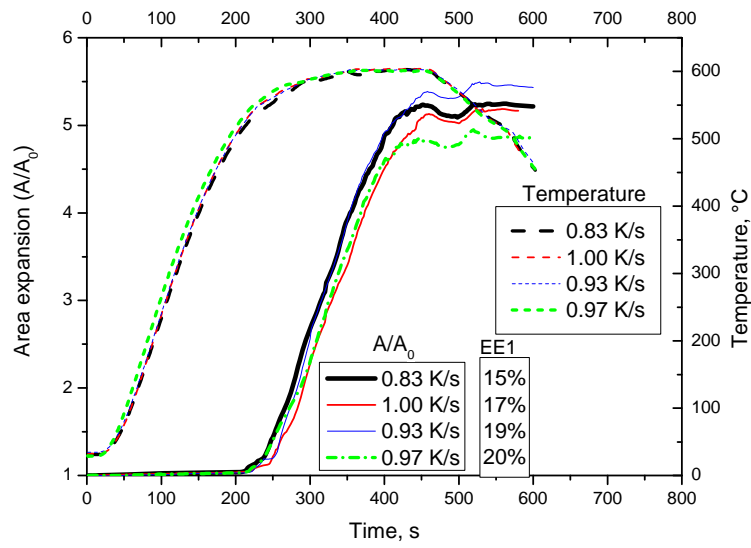


Figure 3.25. Area expansion and temperature (measured by TC1 thermocouple) profile of AlSi7 foaming for four cooling rates. For each experiment HT is 100 s. Cooling rate indicated in the legends corresponds to the average cooling rate measured from the TC1 temperature curve during EE1. Cooling in each case was performed by reducing the power of the lamps from 300 to 59 W. Different cooling rates were measured due to accidental variations. The value of EE1 in each case experiment is shown.

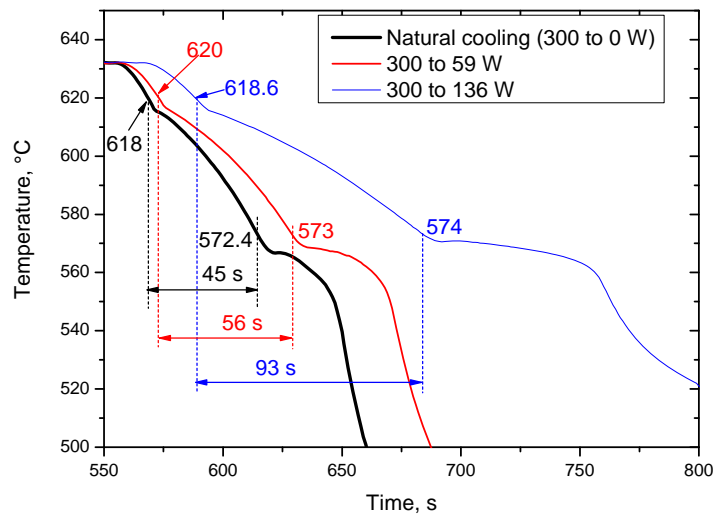


Figure 3.26. Cooling curves measured by a TC4 thermocouple for AlSi7 alloy foam. Legends indicates how cooling was performed. The number in each curve indicates the temperature in °C of the first (top) and second (bottom) minimum. The time given for each cooling curve corresponds to the total time of Al precipitation.

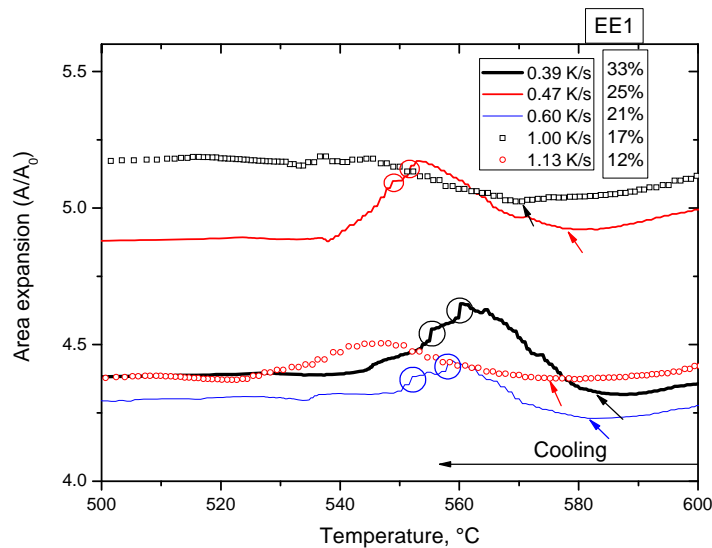


Figure 3.27. Initial cooling part of the expansion profile of AlSi7 foaming (HT 100 s) as a function of temperature (measured by TC1 thermocouple) for five cooling rates. The numbers given in the legend represent the cooling rate (measured by TC1 thermocouple) during EE1. The starting points of EE1 are indicated by arrows. Some of the outer surface bubble ruptures are indicated by circles.

EE1 values for six different cooling rates are shown in Fig. 3.28. For fixed experimental parameters (HT and cooling rate) the values of EE1 are higher in AlSi7 than in AlSi6Cu4. This is already evident when the EEs under natural cooling conditions in these two alloys are compared; see Figs. 3.14 and 3.16(b). That was the reason to perform a more extensive cooling rate experiments on AlSi7 instead of AlSi6Cu4. Higher values of EE1 in AlSi7 allow a more precise measurement. EE1 is plotted as a function of cooling rate in Fig. 3.28. Each data point is the average of at least 3 measurements, except the one for 1.28 K/s cooling rate representing natural cooling. Error bars represent standard deviation. Reducing the power to a fixed lower value does not result in a constant cooling rate in all measurements. This is why error bars for cooling rates were also calculated. The standard deviation in EE1 values is not large except for cooling rate of 0.4 K/s. In total six slow cooling rate measurements were performed. A sharp decrease in EE1 value is observed from cooling rate 0.4 to 0.48 K/s. After that the value of EE1 decreases slowly up to 0.93 K/s followed by relatively higher decrease up to 1.14 K/s. The trend is in agreement with the results for AlSi6Cu4 in Fig. 3.22 where it is shown that EE1 decreases with increasing cooling rate. EE1 corresponding to the natural cooling rate (1.28 K/s) is higher than the EE1 for 1.14 K/s. This is not in agreement with the general trend shown by other the six cooling rates. The range of EE2 is shown for the six slow cooling rate experiments. However, no particular cooling rate can be assigned to them as the cooling was not controlled in the temperature regime of EE2.

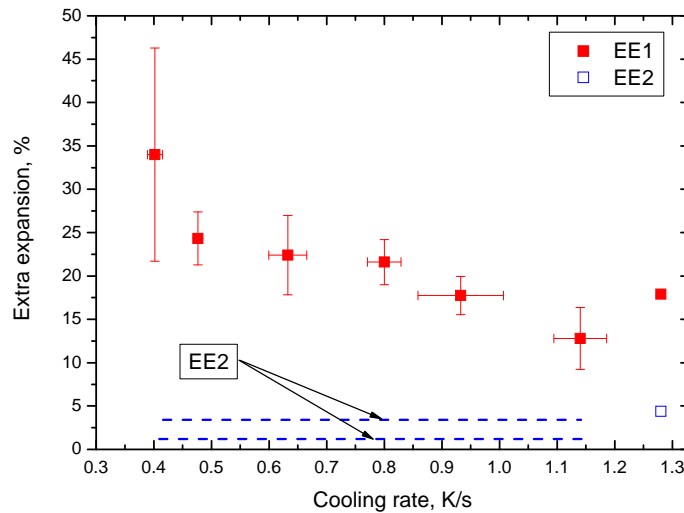


Figure 3.28. Extra expansion 1 (EE1) as a function of cooling rate for AlSi7 alloy foam after applying 100 s HT. The range of EE2 is indicated for six slow cooling rate experiments. The cooling rate represents the average cooling rate measured from the TC1 temperature curve during EE1. Error bars represent the standard deviation. Data point corresponding to 1.28 K/s cooling rate is just for a single experiment. The X-error bar of the data point corresponding to 0.48 K/s has the same range as the width of the symbol.

It was observed that the time period during which EE1 occurs is not constant; longer time for lower cooling rate and *vice versa* was observed. EE1 values were normalized by their respective time periods similarly as for AlSi6Cu4 alloy in Fig. 3.15. The time-normalized values are shown in Fig. 3.29. The trend shown in Fig. 3.28 disappears and all values lie nearly at a constant level including the one for natural cooling.

3.5.3 Results for other alloys

A few selective cooling rate experiments were carried out for AlSi11, AlCu13Mg4 and Al. Area expansion curves for AlSi11 and AlCu13Mg4 are shown for 100 s HT in Fig. 3.30. Cooling was performed with even slower cooling rates than mentioned earlier. For this the power was reduced step by step from 300 to 219, 193, 136 and finally 0 W. At the beginning of cooling AlSi11 continues expanding up to about 555 °C. After that it shrinks drastically. No EE was observed in this alloy. The expanding behaviour of AlSi11 in the initial stage of cooling is identical to that seen in the same alloy for 0 s HT under natural cooling (see Fig. 3.17). Following the same cooling steps, AlCu13Mg4 alloy shows even slower cooling rate as evident from the slopes of the cooling curves. At 580 °C it shows 5.4% EE; an enlarged view of the EE is shown in the inset. The position of the first minimum in cooling rate curve of this alloy is at 583 °C. Therefore, this EE is EE1. The cooling rate during this EE1 is 0.1 K/s. EE was not observed for higher cooling rates. Al was cooled employing two cooling rates, 0.5 and 1 K/s. No EE was observed in any of the cases. Applying a slow

cooling rate of 0.62 K/s to a Zn foam after 100 s HT, 10.3% EE was observed. EE in Zn foam also shows an increase with decreasing cooling rate.

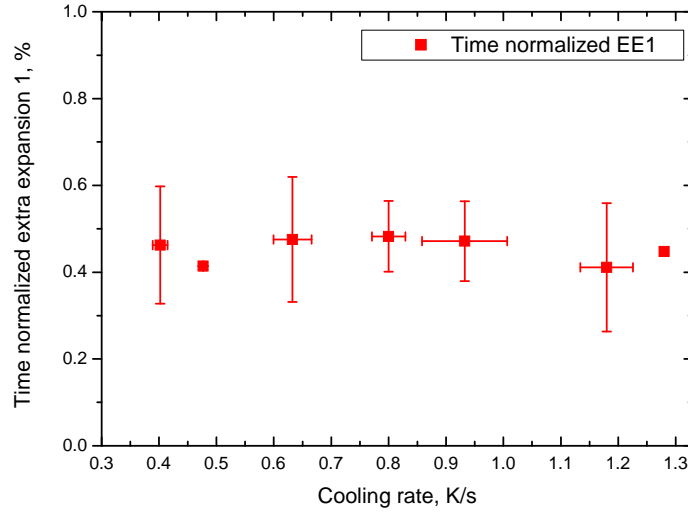


Figure 3.29. Time-normalized EE1 as a function of cooling rate for AlSi7 alloy foam after applying 100 s HT. The cooling rate represents the average cooling rate measured from the TC1 temperature curve during EE1. Error bars represent the standard deviation. Data point corresponding to 1.28 K/s cooling rate is just for a single experiment. The X and Y error bars of the data point corresponding to 0.48 K/s have the same range as the width of the symbol.

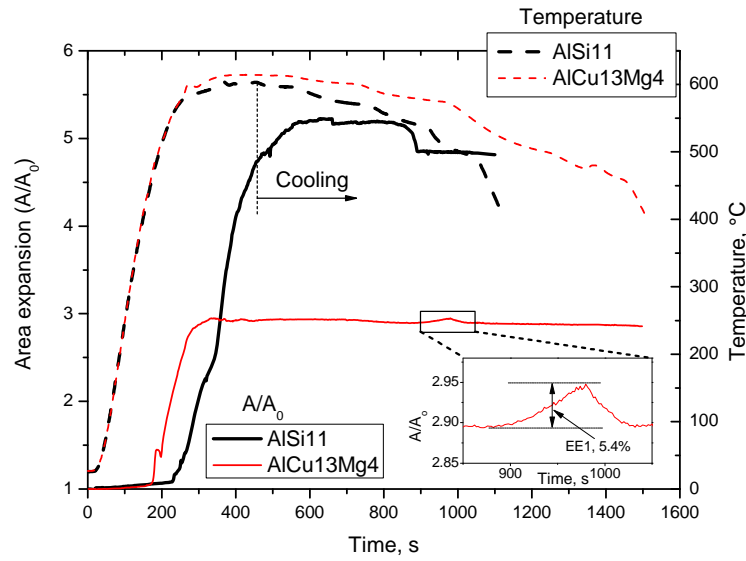


Figure 3.30. Area expansion behaviour and temperature (measured by TC1 thermocouple) as a function of time of AlSi11 and AlCu13Mg4 applying 100 s HT. Slow cooling was employed. Inset shows an enlarged view of the EE in AlCu13Mg4 alloy foam.

3.6 Pressure induced foaming (PIF)

Blowing agent free samples were foamed by PIF method. The modified pressure furnace—where a thermocouple touches the bottom surface of the precursor—was used for

this purpose. The details of PIF method can be found in section 2.3. Foaming temperature was set to 750 °C. A typical example of an expansion curve of AlSi6Cu4 (without blowing agent) made by PIF is shown in Fig. 3.31. The pressure inside the furnace was monitored using a sensor. The sample was melted at 5 bar pressure. During heating the pressure increased slightly due to the temperature rise and finally reached about 5.5 bars. After 100 s of holding the pressure was released to 1 bar. Release in pressure immediately induces expansion of the sample. After 500 s HT at 1 bar natural cooling was employed. The cooling part shows one EE an enlarged view of which is given in the inset. A change in slope in the A/A_0 curve during the initial part of the cooling can be seen. The value of EE in this case is 2.2% and the time spent during EE is 18 s. The cooling rate during EE is about 3 K/s.

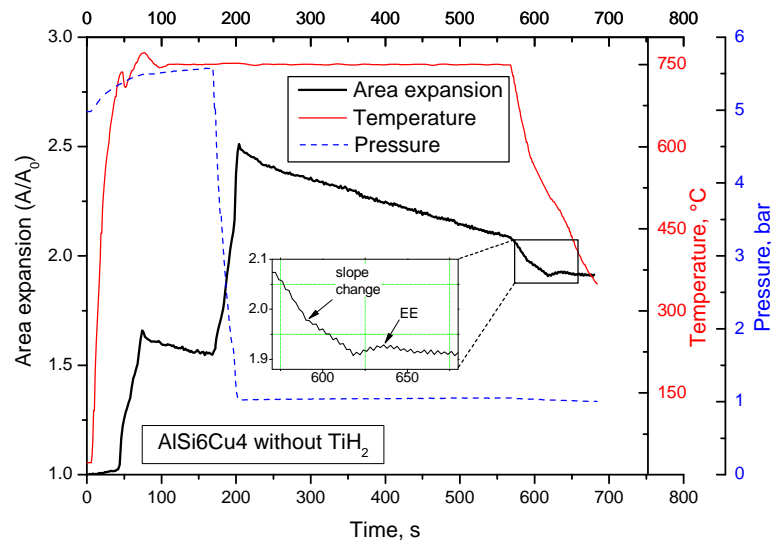


Figure 3.31. Area expansion, temperature and pressure profile of a pressure induced foaming (PIF) experiment for AlSi6Cu4 alloy, EE is 2.2%. The temperature represents the foaming temperature. Pressure inside the furnace was measured using a sensor.

Some more examples of PIF are shown in Figs. 3.32 and 3.33. The experimental details corresponding to Fig. 3.32 are similar to those corresponding to Fig. 3.31, except that after the usual PIF there are additional heating and cooling stages. After cooling to 350 °C, the foam was reheated in each case again to 750 °C under 1 bar pressure. Cooling in each step represents natural cooling. EE was observed in each cooling stages; the values are 2.3, 1.5 and 0.6%. Note that EE decreases from one cooling step to the next. The time taken during EE is 14–18 s. Cooling rates during EE are about 3 K/s. Some slower cooling rate PIF experiments were also performed for this alloy, Fig. 3.33. After cooling down with 2 K/s rate the same foam was reheated again to 750 °C under 1 pressure. A cooling rate of 1 K/s was employed for the second step cooling. EE can be observed in each cooling step: 1.63% for 2 K/s and 2.15% for 1 K/s cooling rate. The time periods of EEs are 32 and 40 s, respectively. Three sets of PIF experiments were carried out using higher pressure, 25 bars for AlSi6Cu4 without blowing agent. For the first, precursor was melted at 25 bars and held at 750 °C for 200 s. Then without releasing the pressure, sample was solidified at a rate of 1 K/s. For the other two

sets the first two steps are similar. Then pressure was released to 16 and 9 bars and then solidified with 1 K/s cooling rate. No EE was observed in any of the higher pressure (25 bars) experiments.

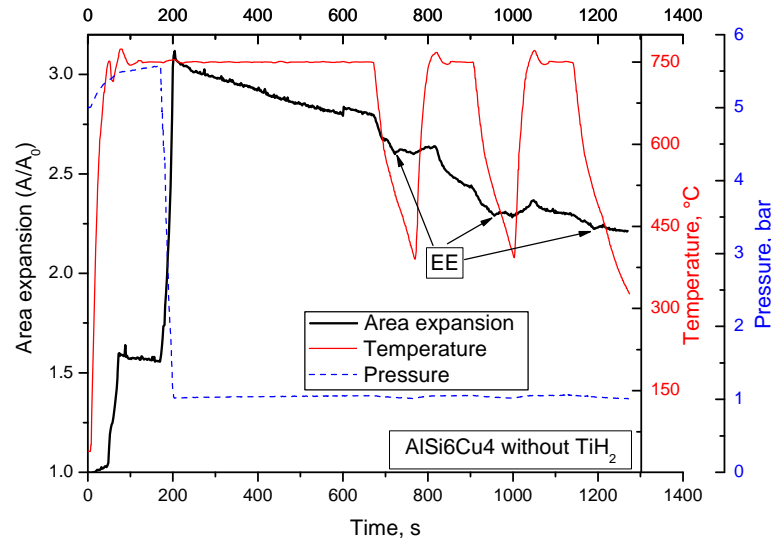


Figure 3.32. Area expansion, temperature and pressure as a function of time for AlSi6Cu4 foamed by PIF. After normal PIF, the sample undergoes two consecutive heating and cooling stages. Natural cooling was employed in each cooling stages. The starting point of EEs is indicated. The temperature represents the foaming temperature. Pressure inside the furnace was measured using a sensor.

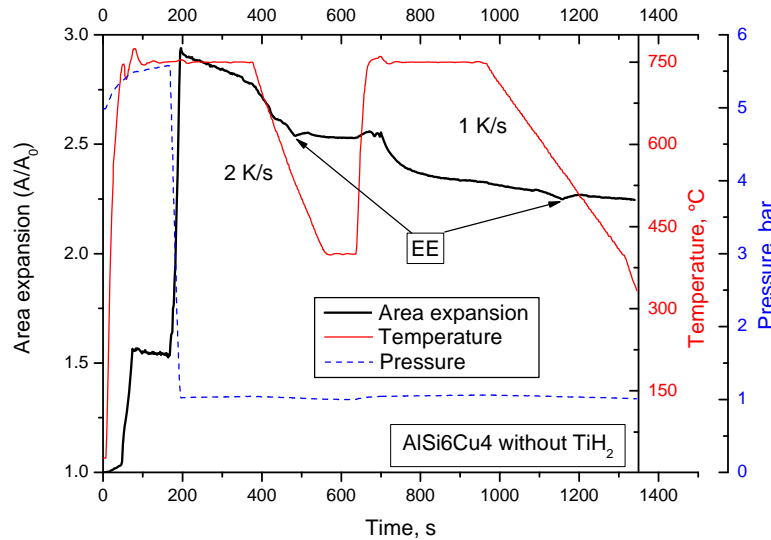


Figure 3.33. Area expansion, temperature and pressure as a function of time for AlSi6Cu4 foamed by PIF. After normal PIF, the sample undergoes one additional heating and cooling stages. Cooling in each stage was performed with slower rates than in natural cooling. The temperature represents the foaming temperature. Pressure inside the furnace was measured using a sensor.

Blowing agent free AlCu13Mg4, AlCu13Mg1 and AlCu20Mg5 alloys were foamed by PIF method. No EE was observed under natural or slow cooling for the first two alloys. Under natural cooling 2.5% EE was observed in case of AlCu20Mg5 alloy.

3.7 Distribution of extra expansion inside foam

Area expansion is measured by the program, AXIM, by monitoring the X-ray projected image. As a result, the value of area expansion is a measure of the area surrounded by the outer contour of the projected image of foam. Since EE is calculated from the area expansion profile, it represents movement of the outer contour of the foam. It does not indicate whether EE occurs throughout the entire foam or whether any part of the foam expands more than the other parts. In order to track EE inside the foam, X-ray radioscopic image sequences were observed during EE. In radioscopic images the contrast of Plateau borders (PBs) or nodes—i.e., junction of PBs—appear darker than to the other parts of the foam. More liquid metal in these areas results in higher X-ray absorption makes them appearing as dark points (nodes) or lines (PBs). These dark regions can allow tracking the internal movements of the foam during EE only if they exist throughout the entire EE stage. Many dark regions, which are present at the beginning of EE, disappear due to ruptures. However, in few cases regions were found which are present during the total EE time period. Foams cooled with slower rate were chosen for this purpose. High value of EE1 in these foams allow for easy monitoring of the internal foam structure. Radioscopic images at the beginning and end of EE1 and four intermediate stages were taken. Taking some of these dark regions as reference the height of the foam was divided into five nearly equal lengths in the image at the beginning of EE1. The measurement scheme is illustrated in Fig. 3.34(a). After some expansion (fictitious) the change in length of each part of the height can be visualized from Fig. 3.34(b). Measurement of individual lengths in each image and comparison of the corresponding lengths of other images reveals the evolution of each part of the foam. For example, by comparing Figs. 3.34(a) and (b) it can be seen that lengths **3** and **4** expanded more than others while length **2** remained the same.

An example of such measurement is shown in Fig. 3.34(c) for an AlSi6Cu4 alloy foam, which was foamed with 200 s HT followed by a cooling with 0.28 K/s rate. The evolution of five different sections along the height of the foam is shown as a function of time during EE1; EE1 is 29.9%. 0 second in the X-axis indicates the beginning of EE1. It can be seen that each part of the height evolves differently. No particular trend can be observed. Such random behaviour was observed in other measurements as well. Hence, it can be inferred that there is no trend in expansion of different parts of the foam during EE. EE is not a global activity inside the foam; some parts of the foam could have more expansion than others, and some parts can shrink at the same time.

The same behaviour can be seen in some other phenomena. In some cases it was observed that when an outer bubble ruptures during cooling but before EE1 (in slow cooled foam) it reappears to some extent during EE1. This can be seen in Fig. 3.35. The images correspond to the data in Fig. 3.20 for 0.31 K/s. There is a rupture in the middle image (614 s) marked by a dashed circle. The image at 712 s represents the stage at the end of EE1. It is clear that during EE1 the ruptured part has redeveloped nearly to its initial state (image at 612 s). The rupture corresponds to the sharp drop marked by the circle in Fig. 3.20. The value EE1 in this foam is 34.4%.

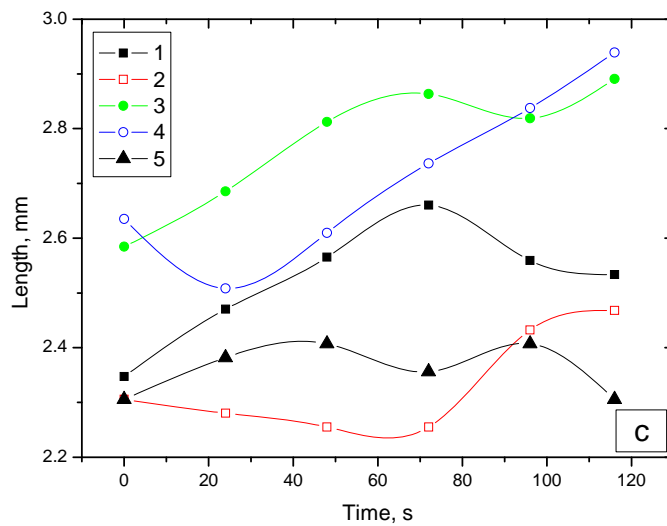
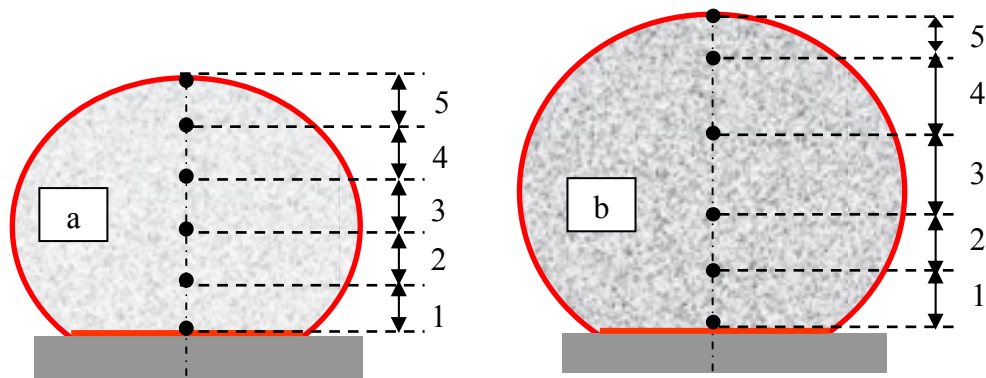


Figure 3.34. (a) Illustration of the selection of five different sections along the vertical axis of the foam. Sections are labelled by numbers. After some expansion (fictitious) the same foam is shown in (b). By comparing (a) and (b) the change in each section of the foam can be determined. (c) Real experiment: length of 5 different sections as a function of time during EE1 (value 29.9%) in an AlSi6Cu4 foam solidified with 0.28 K/s cooling rate after applying 200 s HT. Lines through the points only serve as a guide to the eye.

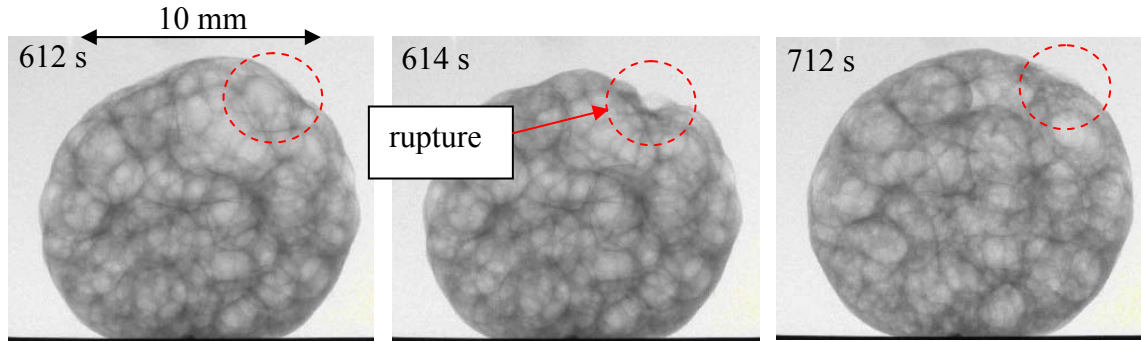


Figure 3.35. Radioscopic images showing rupture (614 s) and re-growth of an outer surface bubble in an AlSi6Cu4 foam that was solidified with 0.31 K/s after applying 200 s HT. The time given in each image corresponds to the time in Fig. 3.20 for 0.31 K/s.

3.8 Foam morphology

3.8.1 Macrostructure

Rupture of a cell is shown by the radioscopic image sequence in Fig. 3.36. This rupture was observed during EE1 in AlSi6Cu4 foam (600 s HT) that was solidified with cooling rate of ~ 0.28 K/s; EE1 is 12%. The rupture of the cell wall that is indicated by an arrow in image 1148 s can be seen by following the image sequence. Initially, due to EE1 the arrow-marked cell wall is stretched which can be seen by comparing images at 1148 and 1158 s. The central part of the cell wall thins and breaks at 1160 s. Subsequently the ruptured ends separate from each other, 1166 s. The ruptured ends still seem to be connected by a thin dark line. Perhaps the entire central area of the cell wall surface is not completely detached. Gradually this connecting thin line disappears. The ruptured cell wall can be seen in the solidified foam, i.e., in the image at 1440 s.

X-ray tomograms of foams, with large EE1, reveal many broken or missing cell walls in the solidified foam. Some examples are shown in Fig. 3.37. The 2D slices shown in Fig. 3.37(a) and (b) show the structure of foams with large EE1: 29.7% for (a) and 33.8% for (b). On the other hand, no such broken cell walls can be observed in the 2D slices of foams cooled by natural cooling (c and d). The image (e) shows a 3D reconstruction of the same foam that is shown in (b). The missing cell walls and partially coupled cells can be seen in (e).

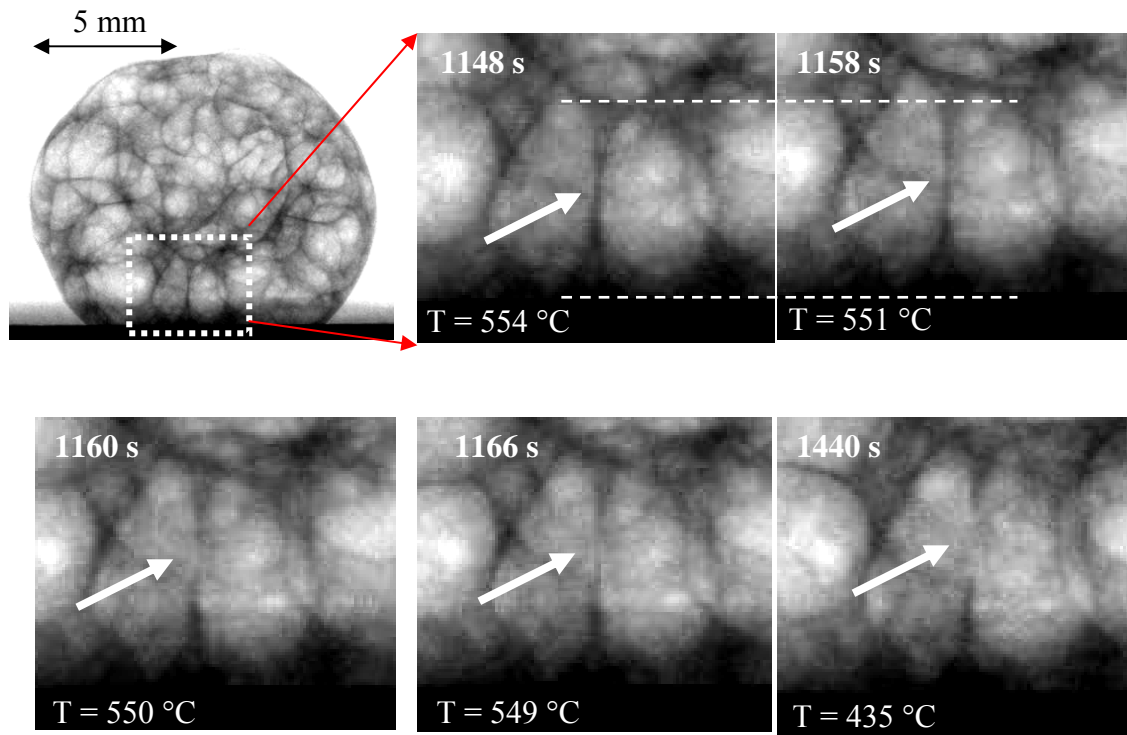


Figure 3.36. Radioscopic image sequence showing different stages of a cell wall rupture during EE1 in AlSi6Cu4 foam. Foam was solidified with 0.28 K/s cooling rate after applying 600 s HT. The last image (1440 s) corresponds to the solid foam.

3.8.2 Microstructure

The microstructure of the cell wall shows significant variation at different cooling rates as shown in Fig. 3.38. Cooling rates corresponding to the microstructures in (a) and (b) are the typical cooling rates used in the present study: natural cooling (a) and slow cooling (b). Two higher cooling rates—that were achieved by forced air—microstructures are shown in (c) and (d) for comparison. The average grain size for 0.2 K/s (b) is about 400 μm , while that in the naturally cooled foam is about 200 μm (a). A broken cell wall can be seen in (b), indicated by a dashed arrow. This is similar to the broken cell walls shown in Fig. 3.37. The pore sizes are higher in slowly cooled foams (a and b) compared to those in fast cooled foams (c and d). The microstructure looks more homogeneous at higher cooling rates (c and d). Two kinds of porosities can be seen – irregular and circular. Irregular pores follow the geometry of the dendrites.

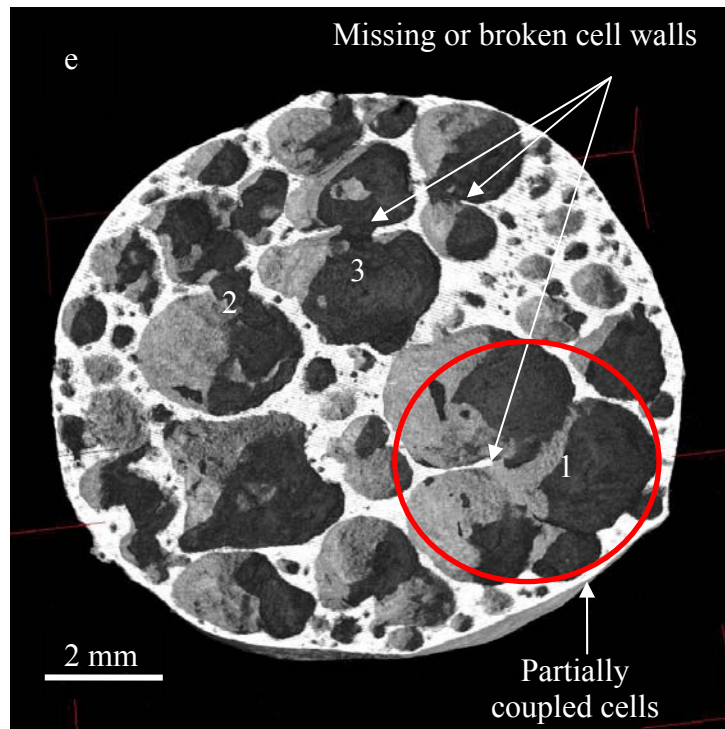
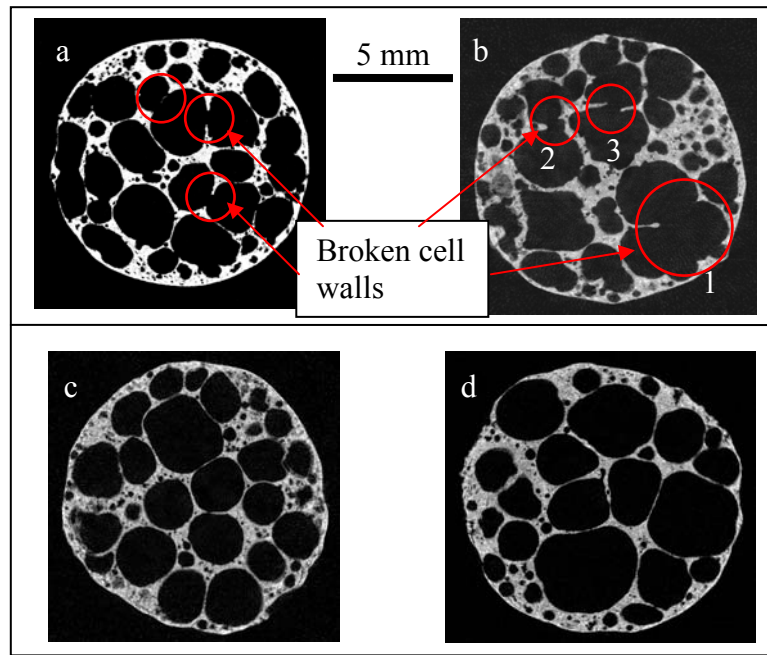


Figure 3.37. (a–d) 2D slices of X-ray tomograms of AlSi6Cu4 foams. (a–b) Slow cooling with an average cooling rate of ~ 0.3 K/s. (c–d) Natural cooling with an average cooling rate of ~ 1.3 K/s. Slowly cooled foams show broken cell walls. (e) 3D reconstruction of the foam corresponding to (b). The broken cell walls indicated by numbers in (b) correspond to the broken cell walls shown by the same numbers in (e). In all images the foaming direction is perpendicular to the plane of paper.

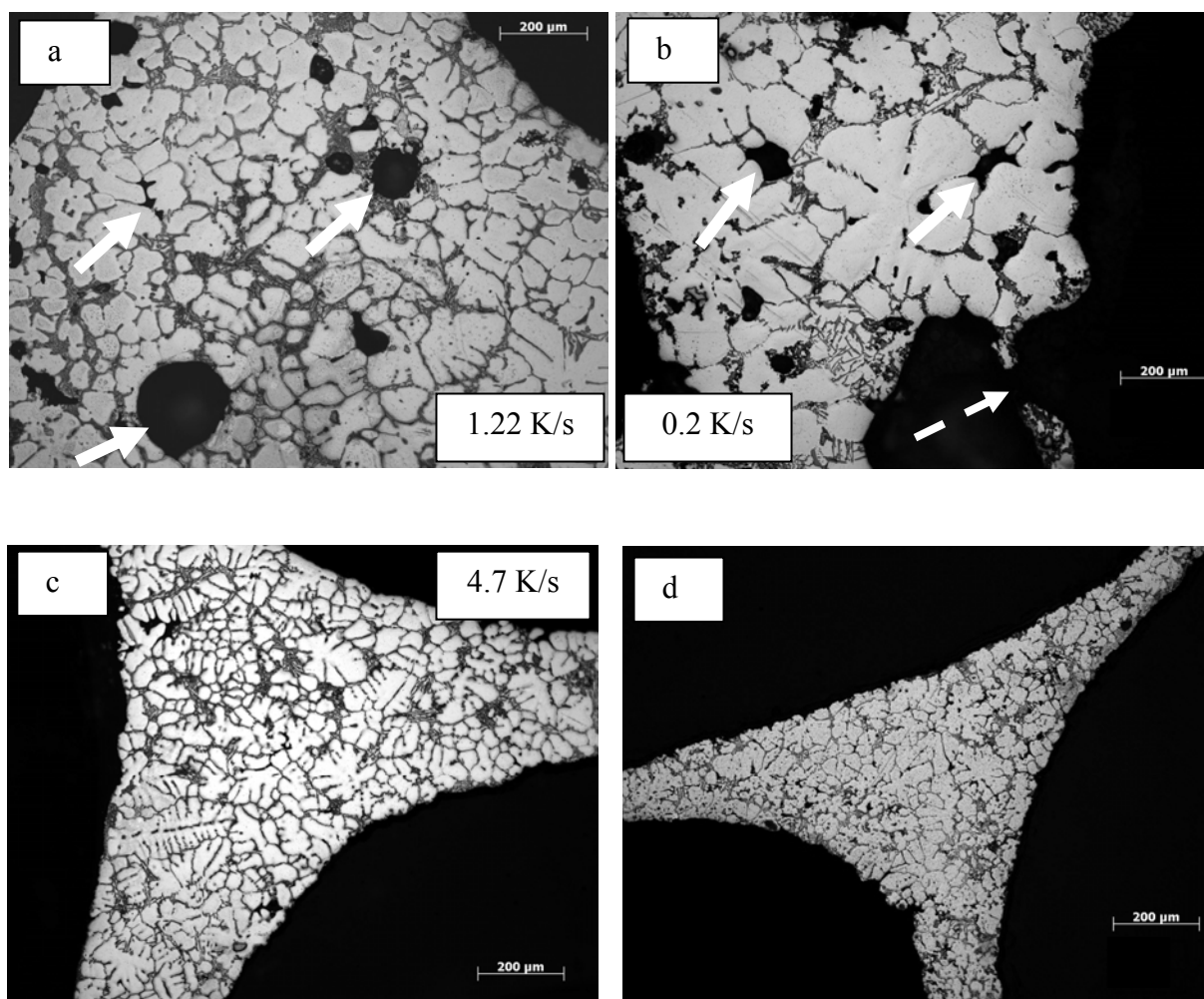


Figure 3.38. Optical micrograph of cell walls of AlSi6Cu4 alloy foams solidified with different cooling rates after applying 600 s HT; cooling rates are given for (a) to (c). Foaming was carried out in the lamp furnace. (a) Represents the microstructure corresponding to the natural cooling. Cooling for (b) was achieved by reducing the power of the lamps. For (c), the foam was solidified by cooling the steel tube (inside which foaming was performed) by blowing air. (d) Foam was cooled directly by blowing air. The cooling rate was not measure in the foam as the foam moved from the thermocouple due to air flow. Solid arrows indicate the pores in the cell walls. Dashed arrow in (b) indicates a broken cell wall.

3.9 Influence of atmosphere on foaming

To investigate the effect of atmosphere, foaming was carried out in air and argon (Ar) under identical heating conditions. Heating was performed using the pressure furnace (modified, see section 2.2.2). For foaming under air the precursor was simply heated in an untreated ambient atmosphere and pressure (1 bar). In case of Ar, the furnace was evacuated to 1 mbar using a pump. Subsequently it was back-filled with Ar from a pressurized gas bottle (Argon 5.0, <2 ppmv O₂, Air Liquid, Germany) up to 1.5 bars pressure. The flushing steps were repeated

three times. Foaming was performed at 1 bar. In total 4 experiments, i.e., 2 in air and 2 in Ar were performed, the results are comparable. The representative foaming behaviour in air and Ar is shown in Fig. 3.39 that shows a comparison of foaming behaviour of Al foam in air and Ar. The precursor was prepared by extrusion and contains 0.5 wt.% TiH₂. The foaming temperature was set to 800 °C. It can be seen that the foam in Ar shows a high degree of collapse during the isothermal heating stage. In contrast, when the foaming atmosphere is air collapse is significantly less. EE was not observed in any of the cases.

Fig. 3.40 shows radioscopic images corresponding to the maximum A/A_0 value and the beginning of cooling in Fig. 3.39. The time given for each image corresponds to the time read from Fig. 3.39. The pronounced collapse under argon can be clearly seen by comparing the images and the A/A_0 values in (c) and (d).

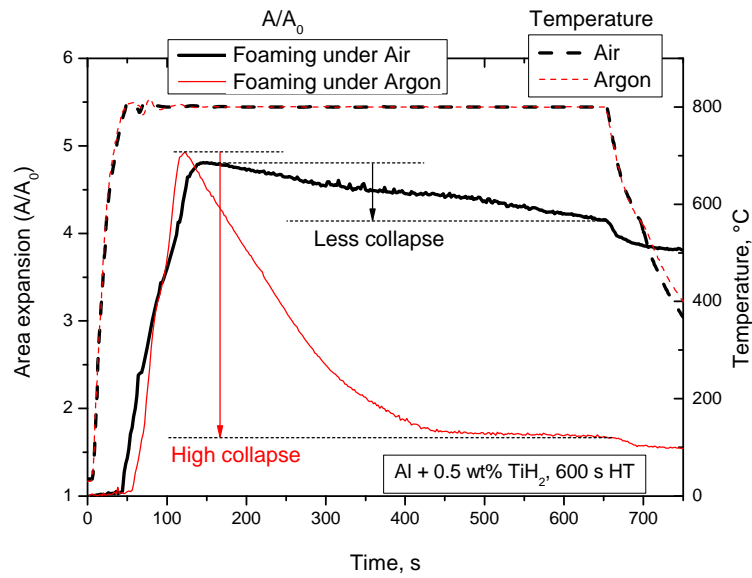


Figure 3.39. Area expansion and the foaming temperature as a function of time for foaming of Al in air and argon. Foaming was performed in the pressure furnace.

Similar experiments were carried out for AlSi6Cu4 alloy at 750 °C furnace temperature. One sample was foamed in each atmosphere. The sample foamed under argon shows more collapse than the one foamed under air, Fig. 3.41. The A/A_0 value of the foam under air after 2500 s HT is comparable to that of the foam that was foamed under Ar after 600 s HT. The difference between the expansions (after 600 s HT) foamed in air and Ar is less than what was observed for Al foam. One EE expansion is present in both cases.

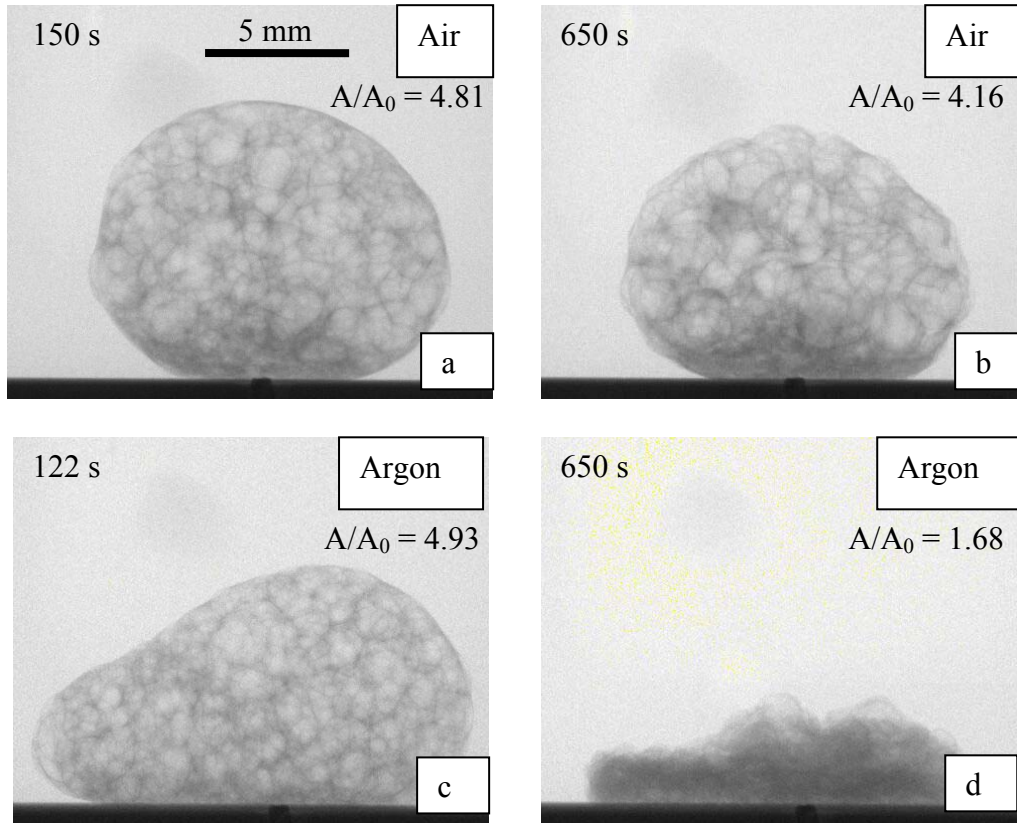


Figure 3.40. Radioscopic images corresponding to the maximum expansion (a and c) and the beginning of cooling (b and d). The images correspond to the data shown in Fig. 3.39. The respective A/A_0 values are mentioned.

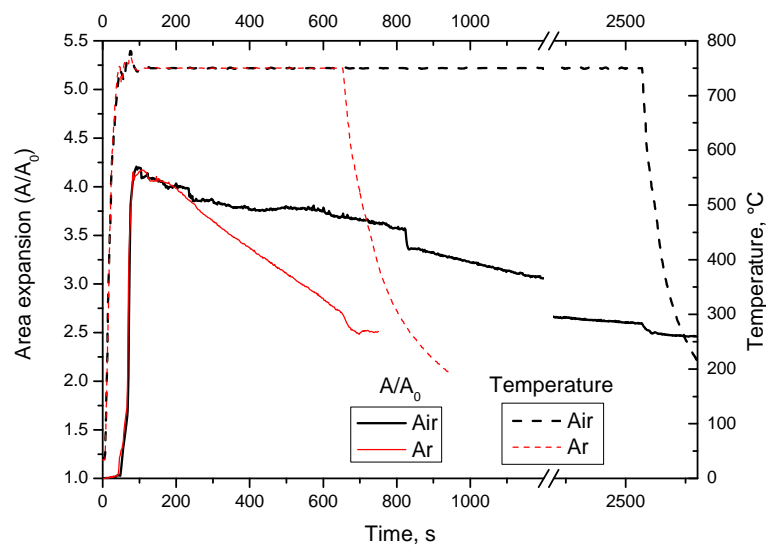


Figure 3.41. Area expansion and foaming temperature as a function of time for foaming of AlSi6Cu4 under different atmospheres. Foaming was performed in the pressure furnace.

3.10 Summary of the results

The occurrence of EE in all alloys under all experimental conditions is summarized in Table 3.3.

Table 3.3

EE values in holding time (HT), cooling rate and pressure induced foaming (PIF) experiments

Alloy	TiH ₂	Extra expansion seen?		
		Natural cooling		Slow cooling
AlSi6Cu4	Yes	EE1	Yes	Yes
		EE2	Yes	Yes
	No	Yes, one EE		Yes, one EE
AlSi7	Yes	EE1	Yes	Yes
		EE2	Yes	Yes
AlSi11	Yes	EE1	Yes	No
		EE2	Yes	
AlCu13Mg4	Yes	No		Yes, one EE
	No	No		No
Al	Yes	No*		No
Zn	Yes	Yes, one EE		Yes, one EE
AlCu13Mg1	No	No		No
AlCu20Mg5	No	Yes, one EE		Not measured
* Some slight EE can only be observed from the radiosopic image sequence, however it is not evident in A/A ₀ curve.				

This page intentionally left blank

4 Discussion

The main motivation of this thesis was to study the anomalous expansion behaviour, namely *extra expansion* or EE, which was observed during the cooling stage of the foaming process. In order to understand the mechanism(s) of EE one should, therefore, contemplate the various phenomena occurring during the cooling stage of foaming. However, as we will see later, the first two stages of foaming (heating and holding) also play a role in determining the behaviour of foam during cooling and thereby influence the EE to a large extent. Therefore, in order to understand EE, the holistic nature of the foaming process should be taken into account.

4.1 Phase transformations in alloys

Three alloy systems (Al-Si, Al-Si-Cu and Al-Cu-Mg) and two single element systems (Al and Zn) were used to prepare foamable precursors (see Table 2.2). The phase transformations during heat-treatment (melting or solidification) of these alloys are discussed here. Table 2.1 shows that none of the metal powers is 100% pure. Small amount of impurities, usually Si and Fe, are generally present in commercial Al powders. Al alloys produced by the PM route, as in the present case, also contain oxide (Al_2O_3). 0.4–1 wt.% of oxide can form on Al powder surfaces during its manufacture through gas (air) atomization [85]. Even use of inert gas for atomization cannot prevent oxidation and results in 0.1–0.3 wt.% of oxide. Moreover, addition of 0.5 wt.% TiH_2 can add 0.48 wt.% of Ti in the system. All these elements together suggest a multicomponent system, and hence, make it complicated to predict the exact phase transformations. For the sake of simplicity, these alloy systems will be treated as pure system in the following.

4.1.1 Al-Si-Cu system

The liquidus projection of the Al-rich corner of Al-Si-Cu ternary phase diagram is shown in Fig. 4.1(a) [86]. The points **e1**, **e2** and **E** represent the location of the Al-Si binary, Al-Cu binary and Al-Si-Cu ternary eutectic composition, respectively. The AlSi6Cu4 alloy used in this study is indicated by point **a** (full circle). Heating of this alloy (from room temperature) results in the first liquid phase at point **E**. Subsequently, the composition follows the monovariant line **E-e1** up to point **b** after which it enters the primary Al corner and at point **a** reaches the liquidus temperature. Solidification of this alloy melt (from above the liquidus temperature) will follow the reverse order, i.e., **a-b-E**. Melting or solidification can be understood better from the pseudobinary diagram at 6 wt.% Si shown in Fig. 4.1(b) where the dashed line denotes the composition of AlSi6Cu4 .

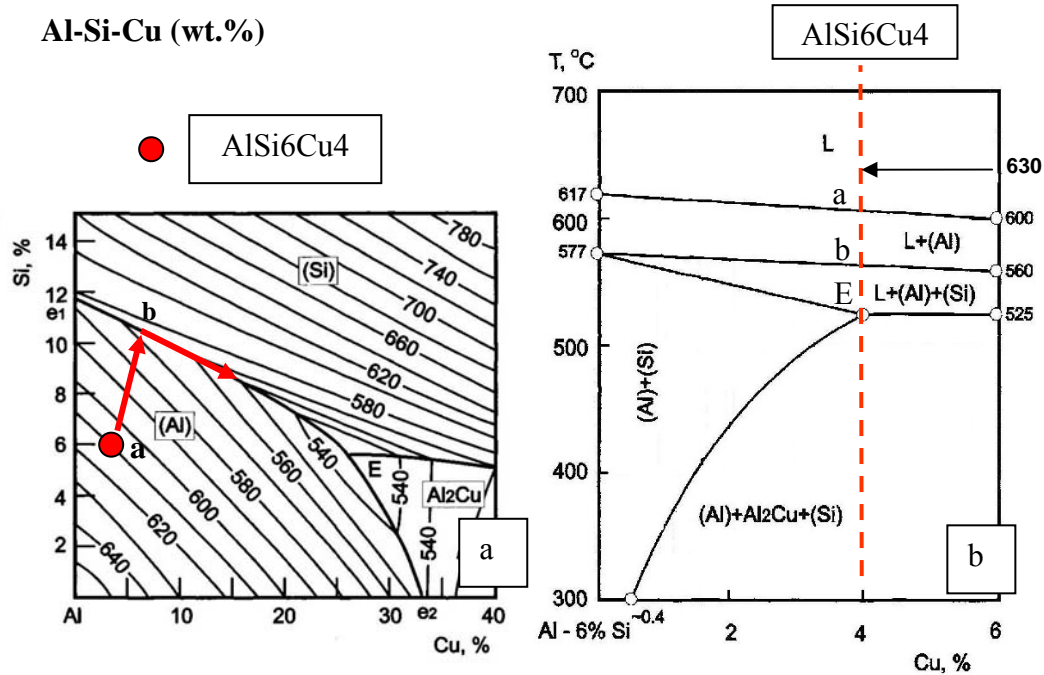


Figure 4.1. (a) Al-rich corner of the Al-Si-Cu ternary phase diagram (liquidus projection). The arrows indicate the solidification direction of AlSi6Cu4 alloy. (b) A pseudobinary diagram at 6 wt.% Si. The dashed line represents the composition of AlSi6Cu4 alloy. (Adapted from Ref [86])

The temperature arrest peaks observed in the cooling rate curve ($\Delta T/\Delta t$) of AlSi6Cu4 shown in Fig. 3.2(b) are the result of latent heat release during the precipitation of various solid phases. The corresponding values of the minimum of each temperature arrest peak represent the nucleation temperature. The first peak reflects the precipitation of Al that occurs from point **a** to **b** in Fig. 4.1(a). The second peak indicates the Al-Si binary eutectic precipitation (i.e., from point **b** to **E**). The third one represents the ternary eutectic reaction at point **E**. Reactions during precipitation of solid phases are given in Table 4.1. Temperatures are compared with the typical values measured during solidification of AlSi6Cu4 alloy foam by TC1 (at outer surface) and TC4 (inside foam) thermocouples (see Fig. 3.1). While the temperature (measured by TC4 thermocouple) of the second and third minima match very well with the literature values, the temperature of the first minimum differs by 10 K. It has been reported that the nucleation temperature of Al increases with cooling rate [87]. The liquidus temperature of commercial 319 aluminium alloy, similar composition as AlSi6Cu4, increases from 608.7 to 621.3 °C for an increase of cooling rate from 0.38 to 2.1 K/s. This cooling rate (2.1 K/s) is comparable to the initial cooling rate observed during natural cooling, and consequently the observed increase in liquidus temperature is expected. Note that the thermocouple placed inside the foam may or may not be touching the metallic matrix all the time as there is a chance that the tip of the thermocouple is inside a gas cell. Consequently, the temperature of the gas is measured. Hence, the temperature measurement during foaming

cannot be considered for critical thermal analysis, and therefore the over-interpretation of these results should be avoided.

Table 4.1

Phase transformations during solidification of AlSi6Cu4 alloy as seen in Fig. 4.1

Reaction	Point in Fig. 4.1	T, °C	T, °C (present study, Table 3.2)	
			TC4	TC1
$L \Rightarrow L + (Al)$	a	~610	619.9	597.9
$L \Rightarrow L + (Al) + (Si)$	b	~566	566.4	533.8
$L \Rightarrow (Al) + (Si) + Al_2Cu$	E	525	524.4	490.7

4.1.2 Al-Si system

Two alloys were chosen from the Al-Si binary system: AlSi7 and AlSi11. The compositions of both alloys are located in the hypoeutectic region of the phase diagram as shown by the dashed lines in Fig. 4.2. The release of latent heat during Al and Al-Si binary phase precipitation results in two temperature arrest peaks in the cooling rate curve of these alloys. The phase transformation reactions during solidification of these alloys are shown in Table 4.2. The phase transformation temperatures are compared with the corresponding temperature measured during solidification of these alloy foams by TC1 and TC4 thermocouples (see Fig. 3.1). In both the alloys the temperature (measured by TC4 thermocouple) of the first minimum is few degrees higher than the literature value. This is similar behaviour as seen in case of AlSi6Cu4 alloy. The temperature (measured by TC4 thermocouple) of the second minimum is few degrees lower than the literature value, see Table 4.2.

4.1.3 Al-Cu-Mg system

Fig. 4.3(a) shows the liquidus projection of the Al-rich corner of the Al-Cu-Mg ternary phase diagram [86]. The points **e1** and **E1** represent the Al-Cu binary and Al-Cu-Mg ternary eutectic, respectively. Solidification of AlCu13Mg4 follows the path **h-i-E1** and solidification of AlCu13Mg1 follows the path **j-k-E1**. The motivation to choose these two alloys was to have ternary system that undergoes three phase transformations during solidification ending with a ternary eutectic, similar to AlSi6Cu4. The composition was chosen from the triangle **Al-e3-e1** in order to avoid the monovariant line **e3-P** that would lead to the peritectic reaction at point **P**, and thereby results in different solidification behaviour than that of AlSi6Cu4 alloy. In contrast, AlCu20Mg5 shows a different solidification behaviour than the former alloys. After starting solidification at point **m** it goes directly to the ternary eutectic **E1**. As a result, there are only two phase transformations during solidification. The reactions during solidification of these three alloys are listed in Table 4.3. It can be seen in case of

AlCu13Mg4 that while the temperature (measured by TC4 thermocouple) of the first and second minima is higher than the literature value, the temperature (measured by TC4 thermocouple) of the third minimum is lower about 14 K less.

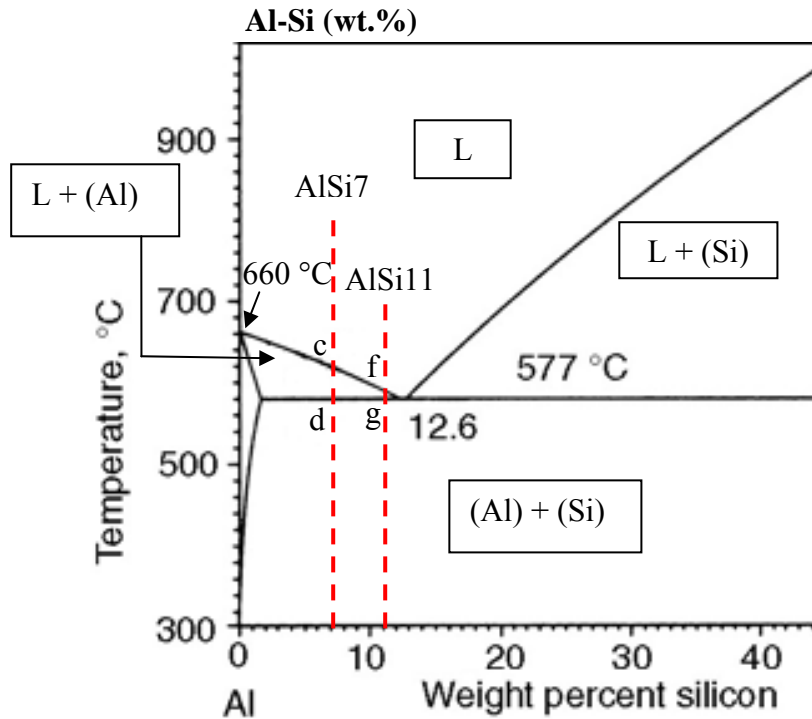


Figure 4.2. Al-Si phase diagram. Dashed lines indicate the location of the composition of AlSi7 and AlSi11 alloys. (Adapted from Ref [88])

Table 4.2

Phase transformations during solidification of AlSi7 and AlSi11 as seen in Fig. 4.2

Alloy	Reaction	Point in Fig. 4.2	T, °C	T, °C (present study, Table 3.2)	
				TC4	TC1
AlSi7	$L \Rightarrow L + (Al)$	c	~615	618	595.7
	$L \Rightarrow (Al) + (Si)$	d	577	572.4	547.6
AlSi11	$L \Rightarrow L + (Al)$	f	~590	597	557
	$L \Rightarrow (Al) + (Si)$	g	577	574.3	548.3

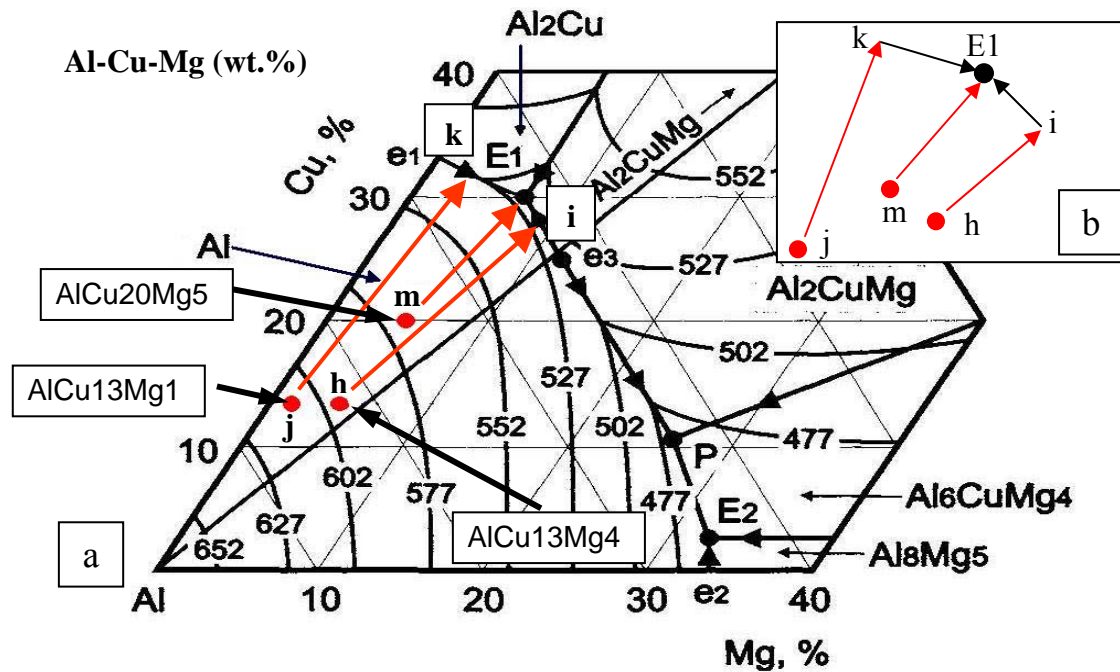


Figure 4.3. (a) Al rich corner of the phase diagram of Al-Cu-Mg system (liquidus). Locations of the three alloys used in the present study are shown. Solidification directions are indicated by arrows. (Adapted from Ref [86]) (b) Schematic of the solidification direction of three alloys.

Table 4.3

Phase transformation reactions and the corresponding temperatures during solidification of AlCu13Mg4, AlCu13Mg1 and AlCu20Mg5 as seen in Fig. 4.3

Alloy	Reaction	Point in Fig. 4.3	T, °C	T, °C (present study, Table 3.2)	
				TC4	TC1
AlCu13Mg4	$L \Rightarrow L + (Al)$	h	~600	606	583
	$L \Rightarrow L + (Al) + Al_2CuMg$	i	~512	521.5	503
	$L \Rightarrow (Al) + Al_2CuMg + Al_2Cu$	E1	507	493.3	477
AlCu13Mg1	$L \Rightarrow L + (Al)$	j	~610	Not measured	
	$L \Rightarrow L + (Al) + Al_2Cu$	k	~530		
	$L \Rightarrow (Al) + Al_2Cu + Al_2CuMg$	E1	507		
AlCu20Mg5	$L \Rightarrow L + (Al)$	m	~570	Not measured	
	$L \Rightarrow (Al) + Al_2Cu + Al_2CuMg$	E1	507		

4.2 Foam formation kinetics

4.2.1 Decomposition of TiH_2

The decomposition of TiH_2 takes place according to the following reaction



The decomposition behaviour of TiH_2 can be seen in Fig. 4.4 [30]. It shows *mass spectroscopic* (MS) measurement of the current produced by H ions as a function of time during the heating of a foamable precursor of AlSi6Cu4 alloy containing 0.5 wt.% TiH_2 . Two types of TiH_2 powders are shown in Fig. 4.4: untreated (as received) and pre-treated in air for 180 minutes at 480 °C. In the present study similar TiH_2 powders were used. Therefore, this MS data represent the hydrogen evolution behaviour during foaming of AlSi6Cu4 alloy of the present study. The pronounced edge shown in each case is considered as the onset temperature of hydrogen release. Hydrogen release from the untreated TiH_2 begins at about 370 °C, which is suitable for foaming Zn (melting point 420 °C). For pre-treated powder onset takes place at about 500 °C.

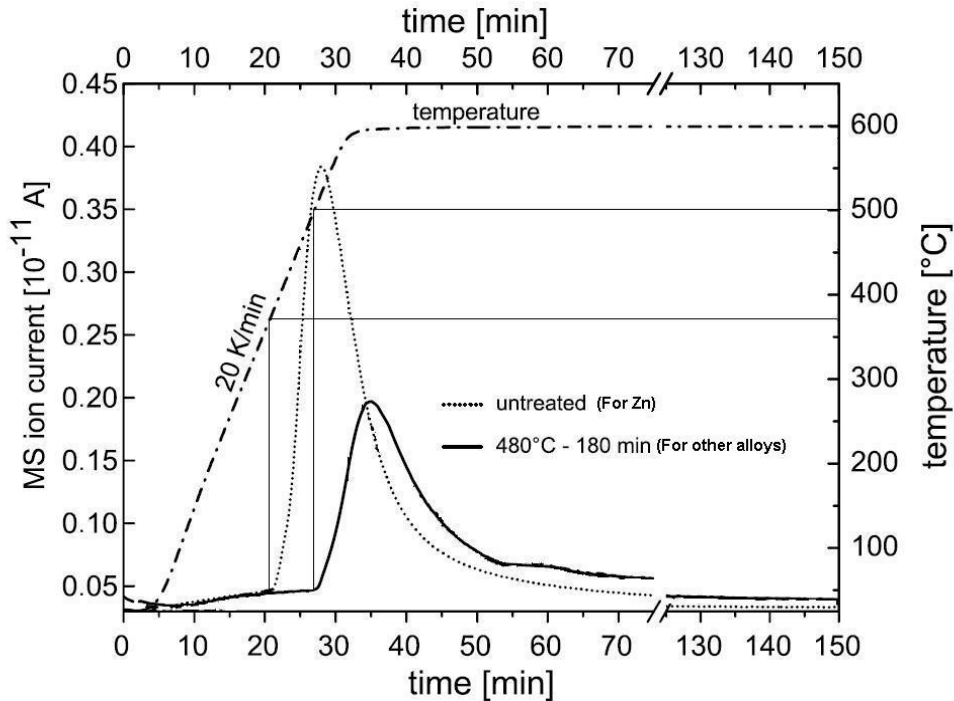


Figure 4.4. Mass spectroscopic analysis of untreated and pre-treated (in air) TiH_2 powders in foamable precursor (analysis is carried out under Ar). Isothermal conditions at 600 °C apply after heating at 20 K/min (adapted from Ref [30]). Features that are not relevant to the present study are removed from the original figure.

4.2.2 Foam expansion behaviour

Under identical experimental parameters and TiH_2 content, the early stages of foaming (i.e., during heating) vary from one alloy to the other. While the expansion of foam can be understood by the decomposition behaviour of TiH_2 , the different characteristics of the expansion behaviour observed in the various alloys requires knowledge of phase transformations occur during heating. Combination of both gives a better picture of the foaming kinetics.

Foaming behaviour of AlSi6Cu4 with 3000 s HT, which is shown in Fig. 3.11, is redrawn in Fig. 4.5(a) emphasizing the heating and holding stages. The initial part of foaming (marked by a dashed rectangle) is enlarged in Fig. 4.5(b). Note that temperature was measured using a TC1 thermocouple. For the real temperature, the TC4 value given in Table 3.2 or 4.1 should be considered. Note that the initial expansion characteristics mentioned for foaming of AlSi6Cu4 with 100 s HT in Fig. 3.4(a) can be compared with those shown in Fig. 4.5(b).

Besides expansion produced by the decomposition of TiH_2 , the metal also expands intrinsically by three phenomena: thermal expansion of metal, expansion due to melting and thermal expansion of metallic melt. The amount of each of these is quite small compared to the total expansion of foam; usually 200–500% expansion (i.e., $A/A_0 = 3\text{--}6$) in the present study. Consequently, these three expansions are usually not considered. Nevertheless, they contribute to the total expansion of foam. The amount of each of them can be determined from the data already available in literatures. Thermal expansion coefficients of solid and liquid metal are in the order of 10^{-5} and 10^{-4} K^{-1} , respectively. Note that the expansion measured in the present study represents area expansion, i.e., projected area of the volume. Accordingly, thermal expansion coefficients should also change. The order of magnitude of linear, area and volume expansion coefficient is same. Therefore, with reasonable approximation, the projection area counterpart of solid and liquid thermal expansion coefficient can be taken as 10^{-5} and 10^{-4} K^{-1} . Heating from room temperature to, say, 500°C would produce about 0.5% (i.e., $A/A_0 = 0.005$) expansion. Such a small value of expansion would appear on the time axis (in area expansion vs. time plot) when the total foam expansion is, e.g., 400% (i.e., $A/A_0 = 5$), see Fig. 3.16(a). It was observed that the initial linear expansion (before melting) accounts for 3–5%, which is one order of magnitude higher than the effect of thermal expansion. This is probably due to an internal gas pressure build-up (before melting) caused by early decomposition of TiH_2 [34] and/or adsorbants [37]. The foaming temperature is usually only 10–15 K higher than the melting point. As a result, thermal expansion of the liquid melt (above liquidus temperature) is about 0.1% (i.e., $A/A_0 = 0.001$) and thus can be ignored for the present purpose.

Melting of different phases is indicated by alphabets (**a**, **b** and **E**) in Fig. 4.5(b). The reactions corresponding to each alphabet is shown in Fig. 4.1. The precursor is not 100% dense and therefore contains some amount of porosities. In powder compacts of Si-containing Al alloy (e.g. AlSi6Cu4 , AlSi7 , AlSi11) the bond strength between Al and Si is lower than between Al and TiH_2 or between individual Al particles. It has been found that pores usually

initiates in Al/Si interface by mechanical cracking triggered by the gas release during heating [40]. The evolving hydrogen gas migrates from the TiH_2 particles to the Al/Si interface through the interconnected porosities present in the precursor. Thus, the early stage of foam formation is by crack formation and subsequent merging of several cracks into one [41]. The large cracks, perpendicular to the foaming direction, can also be seen in the radioscopic images (see Fig. 3.5). Crack formation in the early stage is more prominent in high silicon content alloys, e.g., AlSi7 alloy. The high solidus temperature (577°C) results in a higher build-up of gas pressure leading to larger cracks.

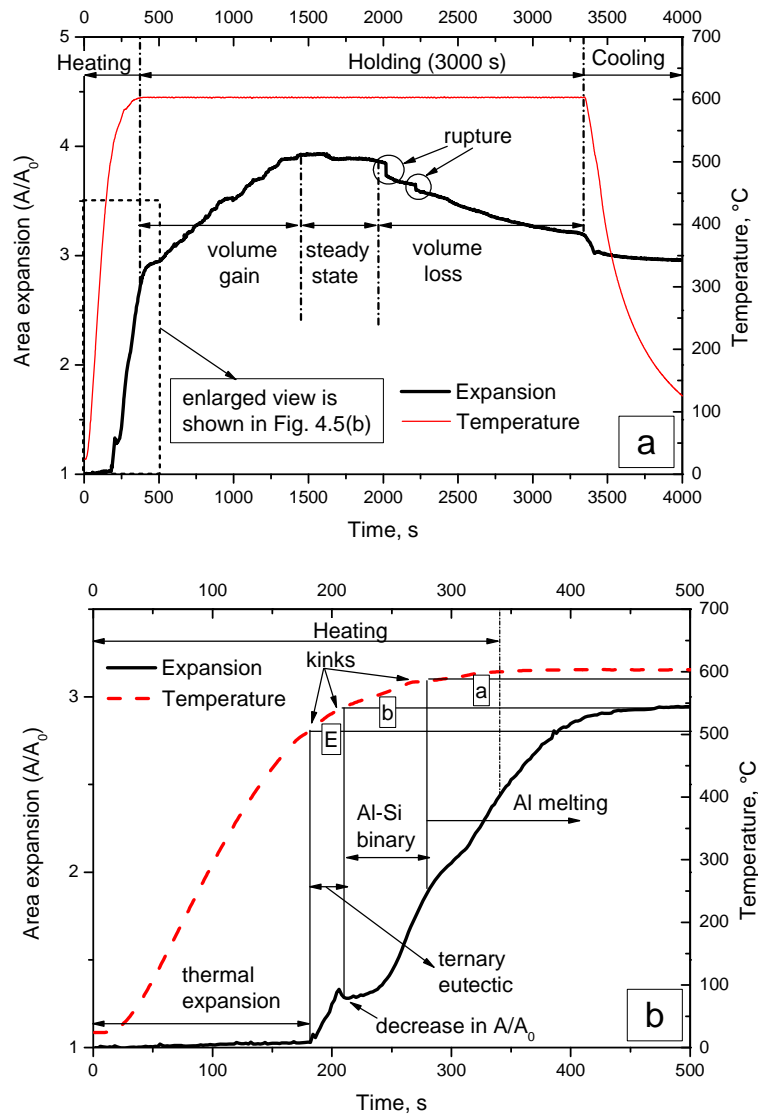


Figure 4.5. (a) Expansion and temperature (TC1) profile as a function of time for AlSi6Cu4 foam, holding time 3000 s. (b) Enlarged view of the dashed rectangle in (a) showing the first 500 s. The points **a**, **b** and **E** corresponds to the phase transformations as shown in Fig. 4.1 by the same alphabets. Data taken from Fig. 3.11.

In the case of AlSi6Cu4 the first liquid phase appears at lower temperature (525°C). The early hydrogen that is present in the porosities and cracks as pressurized gas can then

push the liquid through the interconnected pores to the outer surface at several locations. These appear as protrusions in early stages of foaming in AlSi6Cu4 alloy (see Fig. 3.5). These protrusions account at least partially for the sudden change in expansion, indicated by point **E** in Fig. 4.5(b). With further expansion, the protrusions are reabsorbed by the expanding precursor, which sometimes results in a small decrease in A/A_0 , as shown in Fig. 4.5(b). The next change in the A/A_0 slope, indicated by point **b**, corresponds to the Al-Si binary reaction. Latent heat absorbed during this reaction causes a decrease of the heating rate and thereby the foam expansion gradient. Upon reaching the liquidus temperature the slope of the curve changes once more (point **a**). After this the foam expands steadily and the A/A_0 curve enters the holding stage. The kinks corresponding to points **E**, **b** and **a** represent the Al-Si-Cu ternary, Al-Si binary and Al melting, respectively. Note that the temperature was measured by TC1 thermocouple. The real temperature of melting can be found approximately by comparing the corresponding TC4 temperatures in Table 4.1. Besides hydrogen evolution and phase transformations, there are other phenomena occurring during heating. The density difference between the solid and liquid phases results in a volume increase during melting of alloy. Usually, for aluminium alloys the change in volume is about 6–8% [89]. A detailed account of this will be discussed while addressing solidification of foam. The volume of the already produced gas increases with increasing temperature. Any outer surface bubble rupture and hydrogen diffusion out of foam would lead to volume loss. These mechanisms will be discussed in detail in section 4.3.

At any time, in the molten state the pressure balance in foam can be written as follows

$$P_i = P_o + P_{ST} \quad 4.2$$

where the inside and outside pressures are expressed as P_i and P_o , respectively. P_{ST} represents the pressure arising from the surface tensional force of metallic melt. During expansion of the precursor new surface forms and is readily oxidized when foaming under air. With increasing time and temperature, the oxide layer becomes thicker and inhibits foam expansion through mechanical resistance [42, 65]. Weigand measured the oxide film thickness in air- and argon-foamed AlSi7 alloy samples with Auger electron spectroscopy (AES) and found values of 92 and 30 nm, respectively [66]. On the basis of this result it has been postulated by Dudka et al. that Al foam may contain a 92 nm outer layer and 30 nm inner layer of oxide [64]. By taking into account the strength of the oxide layer it can be shown that the stretching of the oxide layer would need ~6 times more force than that would require for overcoming surface tensional force of liquid melt [64], where the surface tension of aluminium melt is 1 N m^{-1} , and the tensile strength of alumina was set to 100 MPa. So the modified pressure balance can be expressed by

$$P_i = P_o + P_{ST} + P_{oxide} \quad 4.3$$

where P_{oxide} represents the pressure induced by the oxide layer. How oxidation actually hinders expansion is not clear, however, it is evident that it must impose resistance against expansion. With time, hydrogen evolution comes down due to the decreasing H_2 capacity of TiH_2 . Both factors (less hydrogen and oxide layer) together change the expansion slope after some time during the holding stage. For instance, in Fig. 4.5(a) a pronounced edge in the

A/A_0 curve can be seen after about 50 s of HT. Thereafter expansion continues with slower but constant expansion rate. This rate of expansion can be seen in Figs. 3.9–11 for foaming of AlSi6Cu4 with 100 to 3000 s HT foaming.

In the isothermal heating stage, only two mechanisms determine the expansion behaviour: hydrogen production from TiH_2 and gas loss due to out-diffusion. Foaming in the holding stage can be divided into three parts: *volume gain*, *steady state* and *volume loss* (see Fig. 4.5(a)). Volume gain stage continues for about 1000 s HT at an approximately constant rate. This signifies that hydrogen production rate is higher than gas loss rates. After this, both rates may become equal and result in a steady state without much change in A/A_0 value. The time period of steady state may vary for different experiments and sometimes may not be present at all. Beyond steady state, the A/A_0 curve shows a downward movement (volume loss) suggesting that hydrogen production rate cannot compensate the gas loss. For long holding time, some large outer surface bubbles rupture results in sharp drops in A/A_0 as indicated by the circles in Fig. 4.5(a). Rupture of bubbles is a random event; however, for a significantly long HT they are more likely to happen.

In some cases, like for 2000 s HT in Fig. 3.11, A/A_0 may not decrease significantly even for long HT. This is probably due to the fact that diffusion is less in that case. Diffusion is greatly influenced by the thickness of the oxide layer. A thicker oxide skin may reduce gas loss in the volume loss stage. According to Fig. 4.4 there is a peak in hydrogen production. Consequently, A/A_0 is likely to show a maximal value followed by a decreasing trend. Hydrogen evolution is at its maximum after 32 min in Fig. 4.4, whereas the maximum expansion is seen at about 1500 s (i.e., 25 min) in Fig. 4.5(a). This is explainable if one considers different heating profiles: about 2 K/s (i.e., 120 K/min) for foaming and 20 K/min for mass spectroscopic measurements. The hydrogen evolution peak can shift depending on the heating rate as reported for loose TiH_2 powder [90]. Even measurements carried out at the same heating rate show a separation of hydrogen evolution and foam expansion peaks as studied by *thermal desorption spectroscopy* (TDS) [34]. Moreover, one should consider that foam expansion and hydrogen evolution measurement carry slightly different aspects. The hydrogen generated inside the foam results in expansion, whereas for detecting the evolved hydrogen by MS, the gas must first diffuse out of the sample. Foam evolution is a statistical process and greatly influenced by the accidental agglomeration of blowing agent. So, absolute values of expansion may vary from one experiment to the other. However, the characteristic behaviour can be observed in each case with sufficient reproducibility.

Here, it should be mentioned that the present foam expansion is considered as *free foaming* since there is almost no external resistance against foaming except the one arising from oxide skin formation. In-situ observation of foaming using X-ray radioscopy can reveal detailed characteristic behaviours connecting the respective phase transformations and TiH_2 decomposition. Conventional expansion measurements—like those performed using mechanical and laser expandometers [42]—often impose mechanical stresses. As a result, these fine details are easily lost.

The foam expansion behaviour of AlSi7, AlSi11, AlCu13Mg4 and Al which is shown in Figs. 3.16–3.19 can also be understood in a similar way from their respective phase diagrams and the decomposition behaviour of TiH₂. Further details about these individual alloys are avoided here and will be discussed later.

The foaming behaviour of blowing agent free precursors produced by PIF method (see Figs. 3.31–33) is explained by different mechanisms. It has been reported that adsorbants such as H₂, O₂, N₂, CO, CO₂, H₂O, hydroxides or hydrocarbons are the gas source in PIF [37]. It is necessary to keep this gas in the precursor during the heating stage. An overpressure (e.g. 9 bars) is applied in order to do so. During melting of the precursor, still under over pressure, gas nucleation occurs by the gas release from the adsorbants. Subsequently, the pressure is reduced to ambient pressure. As a result, the nucleated gas expands isothermally according to the gas law $PV = \text{constant}$ at constant temperature, where P and V are pressure and volume of the gas. So, if the nucleated gas volume is 20% of the precursor volume (under 9 bar overpressure), releasing pressure to 1 bar would result in 180% of foam expansion. As the expansion is entirely controlled by the external gas pressure, the expansion behaviour seen in blowing agent containing foam cannot be seen here. However, solidification of foams produced by PIF method is similar to that of blowing agent containing foams in some aspects as will be shown later.

4.3 Individual contributions to volume change of foam during solidification

EE was observed during solidification of foam. Figs. 3.8 and 3.13 show that for AlSi6Cu4 the temperature range of EE1 is located in-between the liquidus (first minimum) and the Al-Si binary reaction (second minimum) temperatures. EE2 is located in-between the Al-Si binary reaction and the Al-Si-Cu ternary reaction (third minimum) temperatures. This trend is highly reproducible and was observed for all HT (0 to 3000 s). Therefore, it is evident that there is an interconnection between solidification and EE. While, in general, solidification induces shrinkage in a foam, EE suggests, on the contrary, an intermediate expansion state during solidification. This can be inferred as following: at some time during solidification the volume gain mechanism (or mechanisms) overcomes the shrinkage and results in a net gain. Therefore all phenomena taking place simultaneously during solidification should be understood in order to identify the mechanisms responsible for EE. They can be broadly classified as *volume gain* and *volume loss*. Note that all the A/A_0 curves shown in this work represent projected area expansion, not volume. The starting precursor has a square cross section in the main foaming direction, i.e., perpendicular to the X-ray beam. As liquid phase increases, the corners of the square cross section round off due to surface tensional forces. A fully expanded foam appears nearly spherical. The cross section perpendicular to the foaming direction is nearly circular (see Fig. 3.37). In the radioscopic images of fully expanded foam, which represent the cross sections of the foam in the foaming direction, also appear near circular. Therefore it can be stated that the geometry of the foams produced in this study is

comparable to a sphere. The change in volume of a sphere affects the change in its projected area in a similar way. Hence, any of the phenomena resulting in volume expansion or shrinkage would also affect the projected area (i.e., A/A_0) in a similar way. Therefore, at first, the volume contribution of each phenomenon is considered in general. Later, their projected area counterpart will be considered for quantitative assessment of EE.

All possible mechanisms that can act as volume gain and loss factors are shown in Table 4.4. Note that some of the volume loss factors during solidification act as volume gain factor during the early heating stage (melting of precursor). Since the temperature range of EE is always in the solidification range, only those phenomena occurring during solidification are considered here. Thermal shrinkage of the liquid (above liquidus) and solid (below solidus) is not considered here.

Table 4.4
Possible mechanisms and their contribution on foam expansion

Effect on foam expansion	Mechanism
Volume gain	Hydrogen production from TiH_2 Precipitation of hydrogen from the metallic melt Recalescence effects
Volume loss	Solidification shrinkage of metallic melt Gas bubble shrinkage due to decreasing T Hydrogen out-diffusion or effusive losses Rupture of outer surface bubble

4.3.1 Hydrogen production from TiH_2

It can be seen in Fig. 4.4 that there is some evolution of hydrogen even after a long time, e.g. 60 min. MS measurement on loose powders also indicate the same behaviour [30]. Even heating (5 K/min) of TiH_2 under air cannot decompose fully up to a temperature 850 °C [34]. This is because of the influence of oxygen when heated under air. Oxide layer on TiH_2 acts as additional diffusion barrier, as suggested also by other authors [18]. Hence, it is expected that TiH_2 can still release hydrogen gas during solidification of a foam. However, the amount released will depend on the HT. For short HT, the rate of hydrogen production—caused by higher hydrogen capacity of the TiH_2 —can be so much that foam may show expansion during the early stage of cooling. This explains why AlSi6Cu4 foam for 50–200 s HT continues to expand during the early stage of cooling, see Fig. 3.12. For longer HT, as the amount of available hydrogen decreases, the evolved hydrogen is not sufficient to compensate the effect of volume loss factors, and the result is shrinkage immediately at the start of cooling. The expansion during the initial cooling period for 0 s HT in AlSi11 (see Fig. 3.17) and Al (see Fig. 3.19) is also caused by the ongoing decomposition of TiH_2 .

4.3.2 Precipitation of hydrogen

Hydrogen can be dissolved in liquid metals. There is a significant difference of hydrogen solubility between liquid and solid metal. During solidification, the hydrogen is rejected from the liquid metal at the solid/liquid interface. Precipitation of hydrogen during solidification is known to produce gas porosity in aluminium products [76, 91]. This property of metal-gas binary system is also exploited to manufacture the so called *lotus-type* porous metals [17]. Hydrogen is the only gas soluble in liquid aluminium and its alloys in large quantities. Therefore, precipitation of hydrogen during solidification of aluminium foams can be considered as volume gain factor. The data on solubility of hydrogen in multicomponent alloys are not copious. Therefore, the amount of hydrogen in the alloys used in the present study cannot be predicated accurately. On the other hand, for pure Al, there are some experimental studies, however, mostly reported for 700 °C or higher temperature, e.g. Ref [92].

The hydrogen solubility in aluminium and aluminium alloys has been measured by some authors, e.g., Liu et al. [93] and Lutze et al. [94]. Fig. 4.6, which is redrawn from Lutze et al.'s work [94], shows hydrogen solubility in Al and Al-Si alloys as a function of temperature. From this, the solubility level at liquidus; T_L , (for Al at the melting point) and at solidus or eutectic, T_E , are extracted and shown in Fig. 4.7 as a function of Si content. There are two values corresponding to solidus (577 °C): in the liquid and solid states. The value at liquidus and at solidus (liquid) shows a near linear variation, as verified by fitting straight lines through them. Corresponding values for AlSi7 and AlSi11 are then determined by interpolation. Solubility at solidus (solid) is taken from AlSi6 for AlSi7 and from AlSi12 for AlSi11. The difference in solubility between liquidus and solidus (liquid) precipitates during primary Al precipitation up to 577 °C. In contrast, during the binary reaction (at 577 °C), the amount of precipitated hydrogen is the difference between solubility at 577 °C in the liquid and solid states. These two precipitation stages are indicated in Fig. 4.7.

Hydrogen solubility is usually determined by measuring the hydrogen gas volume at room temperature (300 K) as reported from Sieverts' apparatus measurement of hydrogen solubility [92, 93]. Therefore, the gas volume is the corresponding room temperature value. While considering the actual volume in the foam generated by this gas, one has to consider the corresponding volume at the dissolution temperature. If the measured volume of the dissolved gas is $V1$ at room temperature ($T1$), then the effective volume $V2$ at the precipitation temperature ($T2$) is $V2 = V1(T2/T1)$. This is the reason why the porosity found in Al castings is often three times higher than the theoretical room temperature solubility of hydrogen would suggest [95]. Alternative ways of expressing hydrogen solubility are in atomic% or wt.% which are temperature independent; this way any confusion can be avoided but the direct connection to foam volume is lost.

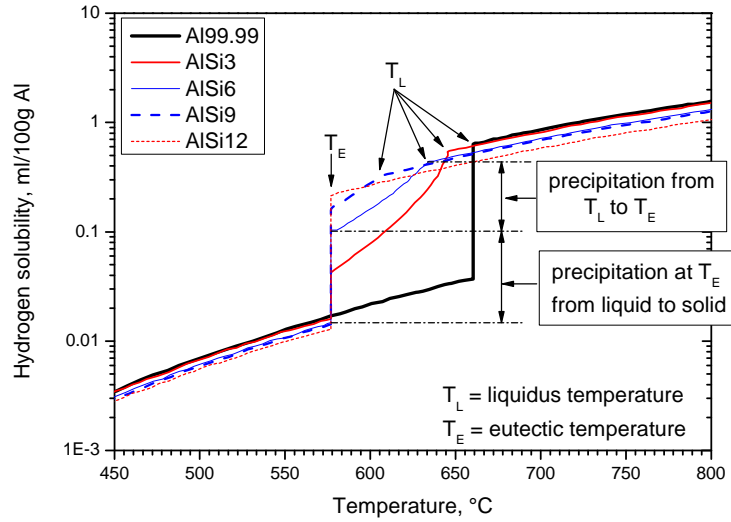


Figure 4.6. Hydrogen solubility in aluminium and its alloys. Redrawn from Ref [94]. Two different hydrogen precipitation stages during solidification of AlSi6 are shown.

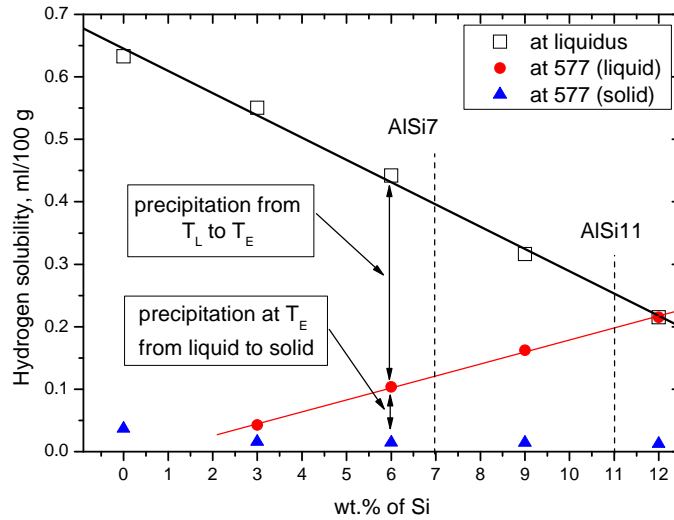


Figure 4.7. Hydrogen solubility in Al and its alloys at liquidus and at solidus (in liquid and solid) as a function of Si amount. The straight lines indicate linear fit. Data extracted from Fig. 4.6.

It is evident that while considering hydrogen precipitation as volume gain factor one should take into account the respective temperature conversion. The liquidus temperature of AlSi7 and AlSi11 can be found in Table 4.2. The melting point of Al is 660 °C, the liquidus temperature of AlSi6 is 634 °C (taken from Fig. 4.6). Taking into account individual temperature conversion factors—e.g., for Al $(660+273)/300 = 3.11$ —the real precipitation volume can be calculated. The volume contribution of precipitation in each alloy can be estimated by using the theoretical density of the alloy; such values in some Al alloys are shown in Table 4.5. There is no data available from which the hydrogen solubility in Al-Si-Cu and Al-Cu-Mg alloys can be determined at the foaming temperature used in the present study. Anyalebechi suggested an alternative way of hydrogen solubility calculation in Al-H-Cu-Mg-Si alloys based on the Wagner's interaction parameters. Interaction parameters are calculated

from experimental data [96, 97]. The values of interaction parameters are valid for 700 °C and higher temperatures. Still, this strategy was used to calculate solubility at 700 °C in order to get an idea of hydrogen content of Al-Si-Cu and Al-Cu-Mg alloys (see Appendix B). Temperature conversion factor is applied similarly on these calculated data considering 700 °C as precipitation temperature. Moreover, using Wagner's interaction parameters, hydrogen solubility in Al, AlSi6, AlSi7 and AlSi11 alloys was also calculated in order to compare with those calculated from Lutze et al.'s work. Values corresponding to 700 °C for Al and AlSi6 measured from Fig. 4.6 are also shown as a direct comparison between experimental and calculated value. Each data in Table 4.5 was obtained after applying temperature conversion factor. Experimental values (7.53 for Al and 6.2 for AlSi6) are in good agreement with the calculated values (8 for Al and 6.33 for AlSi6).

An effort is made to assign some approximate value of hydrogen precipitation at the liquidus temperature of AlSi6Cu4 and Al-Cu-Mg alloys. The reasoning is as follows. The total hydrogen precipitation from AlSi7 (second column in Table 4.5) is approximately 50% of the calculated total hydrogen solubility in that alloy (fifth column in Table 4.5). AlSi7 and AlSi6Cu4 have similar liquidus temperature, 615 and 610 °C. So, as a first approximation, AlSi6Cu4 could precipitate about 2.5 vol.% (i.e., 50% of 4.9 vol.%) hydrogen at its liquidus temperature. In a similar way, AlCu13Mg4 (liquidus 610 °C) and AlCu13Mg1 (liquidus 600 °C) may precipitate about 3.76 and 2.4 vol.% of hydrogen at their liquidus temperature. AlCu20Mg5 (liquidus close to AlSi11) can precipitate approximately 2.6 vol.% of hydrogen. These approximations may differ significantly from the real value. However, under the present circumstances—without having any measured value—this is quite reasonable way to get some estimation.

Table 4.5

Volume contribution of hydrogen precipitation from Al/Al alloys assuming gas saturation in the melt with hydrogen. The volumes given are at the precipitation temperatures or at 700 °C

Alloy	Hydrogen precipitation (vol.%), from Lutze et al.		Hydrogen solubility (vol.%)	
	Total (from T_L to T_E)	At solidus (during eutectic reaction at T_E)	Lutze et al. (at 700 °C)	Anyalebechi (at 700 °C)
Al	5	—	7.53	8
AlSi6	3.45	0.7	6.2	6.33
AlSi7	3.05	0.8		6.13
AlSi11	1.86	1.41		5.5
AlSi6Cu4				4.9
AlCu13Mg4				7.52
AlCu13Mg1				4.83
AlCu20Mg5				7.57

The solubility of hydrogen in Zn is very small [98, 99]. According to the data given in Ref [99] the maximum hydrogen solubility at the melting point of Zn is resolved to be about $8.6 \cdot 10^{-5}$ atoms per Zn atom. In contrast, the same at the melting point of Al is $1.18 \cdot 10^{-3}$ atoms per Al atom [99]; which is more than one order of magnitude higher. Therefore the theoretical dissolved hydrogen is one order of magnitude less in Zn. The density of Zn is about 2.64 times greater than that of Al. Temperature conversion factor at melting point of Al is about 1.35 times higher than that at the melting point Zn. The atomic weight of Zn and Al are 65 and 27, respectively. All these together suggest that the volume contribution of the hydrogen precipitation in Zn foam would be $\left(\frac{8.6 \cdot 10^{-5}}{1.18 \cdot 10^{-3}} * \frac{2.64}{1.35} * \frac{27}{65} \right) * 100\%$, i.e., $\approx 6\%$ the value that is experienced by Al foam.

4.3.3 Recalescence effects

Precipitation of any phase from the liquid state requires nucleation sites. Pure systems contain a limited number of particles which act as nuclei. These particles have a poor nucleating potency and need a high degree of undercooling before they become active [100]. Therefore, upon heat removal the temperature of any melt drops below its melting point before nucleation sets in and crystals start forming. As soon as the crystals have grown to a reasonable size, the latent heat liberated from the system heats up the melt and brings the temperature of the whole system to the value corresponding to the actual state of crystallization; this effect is called *recalcescence*. If such recalcescence occurs during the solidification of foam the associated heating of the melt could both increase the volume of the gas present inside bubbles and act on the remaining blowing agent in the alloy leading to a slightly increased production of gas.

The alloy used in the present study cannot be considered as pure alloy because the powders used for making precursor sample always contain oxide layers around them [64, 85]. Hence, it can be stated that heterogeneous nucleation is more likely to happen and as a result the amount of undercooling cannot be very high, typically less than 1 K [100]. However, in case of AlCu13Mg4 a temperature increase of 9 K (see Fig. 3.3) was observed corresponding to the ternary reaction during solidification. Even so this alloy did not produce any EE during ternary reaction (see Fig. 3.18). This implies that even if in some cases the recalcescence effect is a potential volume gain factor it may not necessarily result in EE. Due to other volume loss factors the effect cannot result in a net gain.

4.3.4 Solidification shrinkage of metallic melt

There are three quite different contractions that occur when metal/alloy cools from liquid to room temperature: contraction of liquid metal, contraction on solidification and shrinkage in solid state. A schematic illustration is presented in Fig. 4.8. Here the contraction during

solidification will be discussed. At the freezing point solid metal, in general, has a larger density compared to that of the liquid metal. As a result, the metallic matrix undergoes volume contraction while solidifying. This phenomenon is known as *solidification shrinkage* (β). The amount of solidification shrinkage is considered a volume loss factor (see Table 4.4). The value of β can be defined by the following equation:

$$\beta = \frac{\rho_s - \rho_l}{\rho_s} \quad 4.4$$

where ρ_s and ρ_l are the densities in the solid and liquid, respectively. Shrinkage associated with solidification of metals used in the present study is given in Table 4.6. The solidification shrinkages for Al and Zn foam can be directly taken from Table 4.6. Al foam will show an about 3% higher volume shrinkage than Zn foam. To correlate volume shrinkage with area shrinkage—which can be measured from the A/A_0 curve—some assumptions have to be made. The foams produced in the present study by PM route can be considered as roughly spherical in shape; the reason has already been discussed earlier in section 4.3. As a rough estimation, the volume data of spherical geometry ($\frac{4}{3} * \pi r^3$, where r is the radius of the sphere) can be converted to its projected area counterpart (πr^2) by introducing the power 2/3 in the volume data. Following this reasoning the area shrinkage in Al foam will be about 2% higher than that in Zn foam. If all metals were solidifying in pure form, then by applying the *rule of mixtures* one could determine the solidification shrinkage in the alloys used in this study. However, Cu and Mg solidify as Al_2Cu (solid density 4.34 g.cm^{-3}) and Al_2CuMg (solid density 3.55 g.cm^{-3}) intermetallics as shown in the Al-Si-Cu and Al-Cu-Mg phase diagrams and therefore do not agree with the rule of mixture. It is necessary to know the solidification shrinkage as a function of temperature in order to estimate its contribution in the A/A_0 curve of the foam.

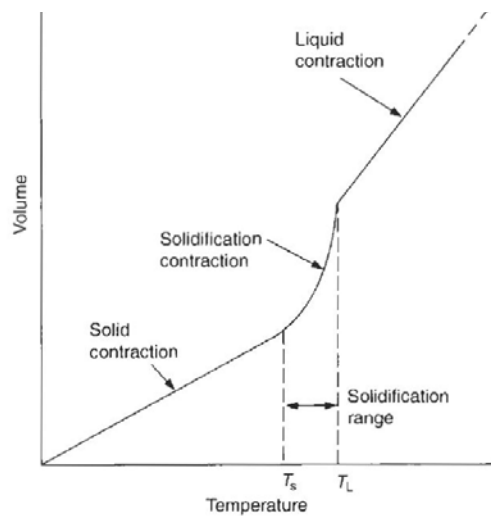


Figure 4.8. Schematic illustration of three shrinkage regimes: in the liquid, during freezing and in the solid. T_s and T_L are solidus and liquidus temperature. Adapted from [76].

AlSi6Cu4 and AlSi7 are the two main alloys used in the present study. The compositions of these alloys are similar to that of commercial 319 and 356 alloy, respectively (see composition in the figure caption of Fig. 4.9). Therefore, the solidification shrinkage data corresponding to 319 and 356 can be used for AlSi6Cu4 and AlSi7. The temperature dependent volume shrinkage data for these two alloys are calculated from the Materials Property Simulation Package JMatPro (Sente Software Ltd., United Kingdom). The results are shown in Fig. 4.9. Both the alloys show about 6% volume shrinkages during solidification. The projected area counter part of it would be about 4%. So, both AlSi6Cu4 and AlSi7 foam would experience 4% shrinkage in their area expansion curve in the solidification range. Note that solidification shrinkage is not a continuous function of temperature. The rate of shrinkage depends on the phase (e.g. primary aluminium or Al-Si binary mixture) that is solidifying. For AlSi11 foam volume shrinkage is about 5% according to the data reported by Magnusson et al. [101]; the area shrinkage would be about 3.4%.

Table 4.6

Solidification shrinkage for some metals as reported in Ref. [76]. () = own calculated value

Metal	Melting point °C	Liquid density (g.cm ⁻³)	Solid density (g.cm ⁻³)	Solidification shrinkage (vol.%)
Al	660	2.368	2.550	7.14
Cu	1083	7.938	8.382	5.30
Mg	651	1.590	1.655	4.1
Zn	420	6.577	(6.857)	4.08
Si	1410	2.525	(2.454)	-2.9

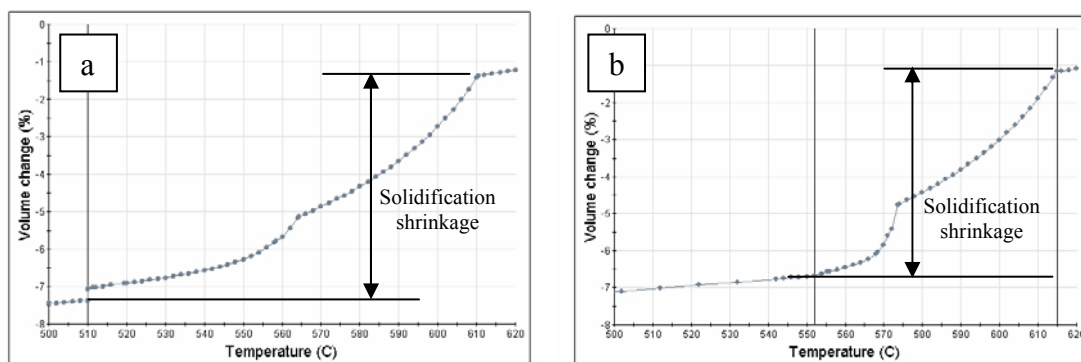


Figure 4.9. Volume change as a function of temperature during solidification of 319 (a) and 356 (b) alloys. The composition (as wt.%) of 319 is – Al: 89.2, Cu: 3.01, Fe: 0.68, Mg:0.3, Mn:0.71, Si:6.1; and of 356 is – Al: 92.43, Cu: 0.05, Fe: 0.2, Mg: 0.3, Mn: 0.02, Si: 7.0.

4.3.5 Gas bubble shrinkage

Gas shrinkage is one of the major volume loss factors and has quite high values compared to solidification shrinkage. According to the ideal gas law, at constant pressure the volume of an ideal gas is proportional to the absolute temperature. Hydrogen can be considered as almost ideal gas. By following the same reasoning as discussed before, the area shrinkage of the hydrogen gas present inside the foam is roughly proportional to $T^{2/3}$. At the onset of solidification, A/A_0 is a combination of the contributions of the area of the gas present in the foam and the area of the metallic melt. In order to estimate the gas shrinkage during solidification, only the gas area should be taken into account. The gas area can be obtained by subtracting the area contributed by the metallic melt. The area of the metallic melt is combination of the initial precursor area and its expansion due to temperature rise (thermal expansion) and melting. For instance, in case of AlSi6Cu4 the area of the metallic matrix at the onset of solidification is about $(1 + 0.005 + 0.04)$, i.e., 1.045, where 0.005 and 0.04 represent the thermal expansion (see section 4.2.2) and the expansion due to melting (see section 4.3.4), respectively. This suggest that if A/A_0 is, e.g., 4.4 at the onset of solidification, the area of the gas present inside the foam accounts for $(4.4 - 1.045)$, i.e., 3.355. While considering gas shrinkage, 3.355 should be taken as the amount of gas.

4.3.6 Hydrogen out-diffusion

Out-diffusion of gas from the foam into the surrounding space is a potential source of gas loss which is present throughout the total foaming process. However, there is no literature available which shows any account of gas loss from foam due to diffusion. Banhart et al. showed (using $D = 3.2 \cdot 10^{-3} \text{ cm}^2/\text{s}$, where D is the diffusion coefficient of hydrogen in liquid aluminium at 660°C) that inter-bubble gas diffusion is irrelevant in metal foams [43]. In contrast, it has been concluded by other authors (using $D = 2.5 \cdot 10^{-2} \text{ cm}^2/\text{s}$ at 650°C) that the size of the pore in aluminium foam is controlled by the diffusion of hydrogen through the liquid [48]. The values of D used in these two studies differ by one order of magnitude. The scatter in the data of D reported from different authors is large. Most of the data are available for diffusion in solid aluminium. A compilation of data can be found in [102, 103]. The range of D in solid Al at 660°C is 10^{-3} – $10^{-5} \text{ cm}^2/\text{s}$. This implies that the diffusion of hydrogen in aluminium is unpredictable. The reason of scatter could be the small hydrogen solubility of Al, as already shown in section 4.3.2, that makes an accurate measurement difficult. Moreover, due to the high oxygen affinity of Al, it also cannot be excluded that surface oxide layers may have influenced the measurements [102]. Eichenauer et al. experimentally measured D in liquid aluminium at various temperatures and provided the following equation for D calculation [104]:

$$D = 3.8 \cdot 10^{-2} \cdot \exp\left(-\frac{4600 \text{ cal/mol}}{RT}\right), \quad 4.5$$

where, R is the gas constant ($1.987 \text{ cal.K}^{-1}.\text{mol}^{-1}$) and T is the absolute temperature. From this equation D was calculated for liquid aluminium at its melting point (660°C); the value is $3.2 \cdot 10^{-3} \text{ cm}^2/\text{s}$. Note that the data is identical to that used by Banhart et al. taken from another source.

It is evident that hydrogen diffusion will start readily after the decomposition of TiH_2 starts. Initially the diffusion will be in solid state. D in solid aluminium at 660°C is $5.6 \cdot 10^{-4} \text{ cm}^2/\text{s}$ [104]. As a result, diffusion will be much less than that in liquid state. As the precursor starts melting, diffusion increases by one order of magnitude. It can be assumed that at some time during heating or holding stage there should be a constant flux of hydrogen if the formation of oxide is ignored for the time being. If equilibrium condition of diffusion is assumed then the volume loss rate, $\partial V/\partial t$ (where V is the volume of the foam), can be estimated by applying Fick's first law. If the foam is considered as a sphere of radius r then $\partial V/\partial t$ as percentage of the total volume is given as follows (for detailed calculations see Appendix C)

$$\frac{\partial V}{\partial t} = -\frac{3 \cdot D \cdot S}{d_{\text{wall}} \cdot r} \cdot 100 \text{ \%} \cdot \text{s}^{-1}. \quad 4.6$$

Here D is diffusion coefficient of hydrogen in Al, d_{wall} is cell wall thickness and S (in cm^3/cm^3 of Al) represents the equilibrium solubility of hydrogen. The negative sign in Eq. 4.6 indicates out-diffusion of gas. D at 660°C is $3.2 \times 10^{-3} \text{ cm}^2 \cdot \text{s}^{-1}$ [104], a typical value of d_{wall} is $100 \mu\text{m}$ (see Fig. 3.38). Due to the small sample size the foams in fully expanded condition appear to be nearly spherical. A spherical foam with 340% expansion has a radius of 7.3 mm considering the present precursor dimensions. At 660°C the solubility of hydrogen in liquid Al is $0.6328 \text{ cm}^3/100 \text{ g Al}$ [94]. In measurement hydrogen solubility is expressed as the corresponding room temperature (300 K) volume. While considering the actual volume of the gas dissolved at the melting point of Al (923 K), one has to consider the corresponding volume at that temperature. Accordingly, the solubility in terms of effective volume is ($923 \text{ K}/300 \text{ K}$), i.e., 3.11 times higher. Density of liquid Al at 660°C is $2.368 \text{ g} \cdot \text{cm}^{-3}$ [76]. So, S is about $0.0466 \text{ cm}^3/\text{cm}^3$ of Al. By using these values in Eq. 3 the obtained $\partial V/\partial t$ is about $6.13 \text{ \%} \cdot \text{s}^{-1}$. According to Eq. 1, $\partial V/\partial t$ is inversely proportional to the radius. Therefore as the foam shrinks due to continuous loss, $\partial V/\partial t$ increases further. This implies that the foams produced in this study would collapse completely in about 10–15 seconds through out-diffusion of hydrogen. The present observation does not agree with this. And also no such evidence has been reported in literature.

The possible reason for this apparent contradiction is the surface oxide skin. For pure aluminium the oxide film is initially an amorphous variant of alumina (Al_2O_3) that quickly transforms into a crystalline variety, $\gamma\text{-Al}_2\text{O}_3$, which is probably a few nanometres thick, and inhibits further oxidation [76]. However, after an incubation period the $\gamma\text{-Al}_2\text{O}_3$ transforms into $\alpha\text{-Al}_2\text{O}_3$ that allows oxidation at faster rate. Alumina present in foam is obviously in solid form due to its high melting point, $\sim 2054^\circ\text{C}$. Belonoshko et al. determined hydrogen diffusion in $\alpha\text{-Al}_2\text{O}_3$ (solid) by first-principle calculation [105]. The value of D at 660°C is

about 10^{-9} cm²/s, which is six orders of magnitude less than that in liquid aluminium. Therefore the main rate determining diffusion is the diffusion through Al₂O₃, which prevents any drastic collapse of foam by slowing down gas losses.

It is expected that the inner surface of the foam is in contact with a pure hydrogen atmosphere, and therefore, there is little chance of oxidation. However, the oxide content of the powders, as reported in Ref [64, 85], may result in an inner oxide skin. Note that the measurement of the thickness of the oxide skin in Ref [66] was performed in air; it is not clear if there is any influence of additional oxidation during the measurement. The greater oxide thickness on the outer surface could be because of oxidation during foaming in air. Foaming under inert atmosphere (e.g. Ar) could reduce the outer oxide skin thickness to some extent, at least. Consequently, when foaming is performed in Ar, the collapse of the foam should be faster compared to that of the foam in air. To test this hypothesis pure aluminium was foamed both under air and Ar atmosphere (see section 3.9). During solidification other volume loss factors superimpose on each other and thus would not allow distinguishing the effect of diffusion. To avoid this difficulty, the foam was isothermally held at foaming temperature. This way the only source of gas loss should be the one resulting from out-diffusion of hydrogen. However, the gas generation from the TiH₂ cannot be avoided. The results are presented in Figs. 3.39–40. The difference in foaming under air and Ar is significant. Foams in air collapse at a slower rate, while in Ar foams show rapid collapse. The initial area loss rates (i.e., slope of A/A_0 at onset of collapse after reaching the maximum expansion) measured from Fig. 3.39 for foam in air and Ar are 0.2 and 1.4%, respectively.

Besides the oxide skin, there are some oxide zones inside the cell wall as shown by Dudka et al. [64]. How the diffusion changes with the increasing collapse of the foam is not clear. As the volume of the foam decreases, the surface area also changes. The change in surface area results in a decrease in total diffusion. After the outer layer of bubbles collapses, the outer surface of the foam comes in contact with the surface just immediately beneath it. This in turn can increase the effective thickness of the oxide layer and consequently decrease the gas loss due to diffusion. All these parameters make the accurate estimation of the out diffusion complicated. Al powder is not 100% pure, Si and Fe are usual impurities. The presence of these elements increases the oxide thickness by some factors, which range from ~2 for Fe to ~2.5 for Si [76].

It was observed for AlSi6Cu4 foam that the difference in collapse between air and Ar is less than for Al foam, see Fig. 3.41. The presence of Si and Cu together could have increased the oxide thickness even in inert atmosphere. As a result, the foam did not collapse so much in Ar. Still however, the collapse rate under Ar is higher than under air. Diffusion in metal foams is difficult to understand due to the unknown thickness and morphology of the oxide layer produced in different alloys, and further detail study is required. However, it can be concluded that the amount of diffusion is less when foamed under air.

The last volume loss factor, rupture of outer surface bubbles, is entirely random in nature. For longer HT there are some bubble ruptures as shown in Fig. 3.11. However, during solidification under natural cooling no such significant rupture was observed. In case of slow

cooling there is some evidence of ruptures during solidification, see Fig. 3.20 for AlSi6Cu4 and Fig. 3.27 for AlSi7 foam. During both natural and slow cooling outer surface bubble rupture is uncommon during EE. Hence, they could be ignored while considering EE.

4.3.7 Contribution from all mechanisms

The total *volume increase* (V_{in}) of the foam during solidification is a combination of all the volume gain (V_G) and volume loss (V_L) mechanisms that occur during solidification. The total volume increase rate of the foam can be given by the following equation:

$$\frac{\partial V_{in}}{\partial t} = \frac{\partial V_G}{\partial t} - \frac{\partial V_L}{\partial t}. \quad 4.7$$

When $\partial V_L/\partial t > \partial V_G/\partial t$, $\partial V/\partial t$ is negative, i.e., the foam undergoes shrinkage. If $\partial V_G/\partial t > \partial V_L/\partial t$, $\partial V/\partial t$ is positive, then the foam experiences expansion, which is referred as extra expansion or EE. In terms of its constituents V_G and V_L can be expressed as

$$\frac{\partial V_G}{\partial t} = \frac{\partial}{\partial t} (V_H + V_{prec}) \quad 4.8$$

and

$$\frac{\partial V_L}{\partial t} = \frac{\partial}{\partial t} (V_{SS} + V_{GS} + V_D + V_R), \quad 4.9$$

where,

V_H = hydrogen produced from TiH_2 ,

V_{prec} = precipitated hydrogen,

V_{SS} = solidification shrinkage of the metallic melt,

V_{GS} = gas bubble shrinkage,

V_D = hydrogen out-diffusion, and

V_R = volume of bubbles rupture on outer surface.

$\partial V_H/\partial t$ is a function of temperature and amount of hydrogen stored in the TiH_2 . $\partial V_{prec}/\partial t$ and $\partial V_{SS}/\partial t$ depend on the alloy and temperature. $\partial V_D/\partial t$ is a function of temperature and oxide layer thickness. For different HT, it can also be a function of HT since $\partial V_D/\partial t$ decreases with increasing oxide thickness as explained earlier. Under identical condition the thickness of the oxide layer is only a function of HT; it increases with HT. $\partial V_R/\partial t$ is excluded from further discussion for the reason given in section 4.3.6. So, Eq. 4.7 can be rewritten as:

$$\frac{\partial V_{in}}{\partial t} = \frac{\partial}{\partial t} (V_H + V_{prec} - V_{SS} - V_{GS} - V_D). \quad 4.10$$

4.4 Reason of extra expansion – the kinetic effects

Based on the temperature measured inside the foam (i.e., with TC4 thermocouple) it is possible to estimate the shrinkage of the gas present inside the foam. An example is shown in

Fig. 4.10 for AlSi6Cu4 alloy foam with 200 s HT and solidified by natural cooling. Only the solidification part of the A/A_0 curve is shown. The TC4 temperature data is taken from another experiment. The time corresponding to the beginning of Al precipitation in TC4 temperature curve is shifted to that in TC1 temperature curve of Fig. 4.10. This allows to consider the TC4 temperature as the inside temperature of the foam from the beginning of solidification. Note that the starting points of Al-Si binary and ternary precipitation in TC4 temperature do not match with their corresponding point in TC1 temperature. It has already been stated in section 4.3.5 that the value of the A/A_0 curve is a combination of the metal (or alloy) of the initial precursor, the expansion of the metallic matrix and the gas present in the bubbles. The total contribution from the metal part and its expansion corresponds to 1.045. In Fig. 4.10, the A/A_0 value at the beginning of solidification is about 3.789. So, the amount of the gas is $(3.789 - 1.045) = 2.744$. This amount of gas will experience shrinkage due to the temperature drop.

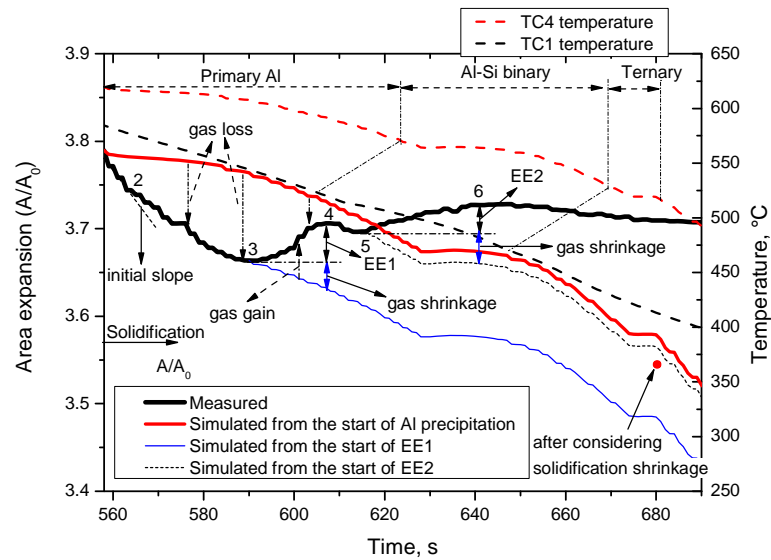


Figure 4.10. Area expansion behaviour (legend “Measured”) as a function of time during solidification of AlSi6Cu4 alloy foam. The data is taken from Fig. 3.9 corresponding to 200 s HT. Simulated A/A_0 curve (legend “Simulated from the start of Al precipitation”) is calculated based on the gas shrinkage considering the temperature (measured by TC4 thermocouple) inside the foam. The A/A_0 value at the start of Al precipitation is taken as the reference starting point of calculation. The filled circle indicates the A/A_0 value after subtracting the total solidification shrinkage value from the simulated A/A_0 value. Two other simulated A/A_0 curves were calculated taking the A/A_0 values at the start of EE1 and EE2. The interesting points of the A/A_0 curve are labelled by numbers.

Since at constant pressure the volume of gas is proportional to the absolute temperature T , the projected area can be expressed as proportional to $T^{2/3}$. Following this reasoning, the A/A_0 curve is calculated by only considering gas shrinkage. This calculation does not include the contribution from the solidification shrinkage and hydrogen precipitation

for two reasons: the first, the temperature dependent behaviour of these quantities is not known; the second, their effective contributions may differ from the theoretical ones. These will be discussed in detail in later sections (sections 4.5.2 and 4.5.3). The expected value (at the end of solidification) of the simulated A/A_0 after considering the solidification shrinkage (0.04) is indicated in Fig. 4.10. The present discussion mainly focuses on the gas shrinkage, diffusion and hydrogen production. The numbers in Fig. 4.10 indicate the characteristic features of the A/A_0 curve. The significance of each number is the same as that described for Fig. 3.6.

The time dependent form of gas shrinkage rate can be divided into two parts,

$$\frac{\partial V_{GS}}{\partial t} = \frac{\partial V_{GS}}{\partial T} \cdot \frac{\partial T}{\partial t}, \quad 4.11$$

where T is the absolute temperature. According to the ideal gas law ($\partial V_{GS}/\partial T$) is constant. Therefore, the gas shrinkage rate ($\partial V_{GS}/\partial t$) depends only on the cooling rate ($\partial T/\partial t$). During solidification of any solid phase latent heat is released and it takes time to dissipate. As a result, the cooling rate decreases. This is reflected by the plateaus in each of the phase precipitation regions in the TC4 temperature (see Fig. 4.10). Decrease in cooling in turn decreases the gas shrinkage rate. Precipitation of Al results in the decrease of the gas shrinkage rate during the initial solidification stage; this can be seen as a nearly flat region of the simulated A/A_0 curve in the primary Al precipitation zone. In the original A/A_0 curve this is reflected by a change in slope (point 2). Fig. 3.13 shows that the change in slope is consistent for all holding times and always appears after the start of primary Al precipitation. The experimental A/A_0 curve shows more shrinkage of the foam than the gas shrinkage would suggest. With increasing time during solidification the deviation between simulated and original A/A_0 curve increases up to point 3. This is caused by the continuous gas loss due to out-diffusion of hydrogen. It has been mentioned earlier (see section 4.3.1) that probably the hydrogen production is still continuing. This indicates that the rate of the loss due to diffusion is more than the hydrogen production rate up to point 3, i.e., $\partial V_D/\partial t > \partial V_H/\partial t$ in Eq. 4.10. After this, the A/A_0 curve shows expansion up to point 4; this is referred as the EE1. Evidently in-between points 3 and 4 the hydrogen production rate (from TiH_2) $\partial V_H/\partial t$ is greater than the total volume loss rate $\partial V_L/\partial t$ due to all the volume loss factors. Presence of EE1 confirms that there is still hydrogen evolution from the TiH_2 . Note that the hydrogen precipitation rate ($\partial V_{prec}/\partial t$) can, in principle, also contribute to the EE1. However, since EE1 was observed only for shorter HT, $\partial V_H/\partial t$ is expected to be the main factor of EE1.

The value of EE1 measured from the original A/A_0 curve does not indicate the total hydrogen production. The contributions from gas shrinkage and out-diffusion during EE1 should be taken into account and added with the measured EE1 in order to get the real hydrogen production. The amount of gas shrinkage can be estimated by simulating the A/A_0 curve and taking the A/A_0 value corresponding to point 3 as starting value, see Fig. 4.10. The amount of gas loss due to diffusion cannot be calculated. After point 4, the A/A_0 curve shows shrinkage again up to point 5. This is probably due to the increase in gas shrinkage rate caused by the increase in cooling rate towards the end of Al precipitation. It has been shown

in Fig. 3.7 that the cooling rate increases at the end of each peak in the cooling rate curve. EE2 takes place in between point **5** and **6**. TC4 temperature suggests that Al-Si binary phase precipitation starts after the time corresponding to point **5**. However, the measured temperature (TC1 temperature) indicates the opposite. The mismatch in time of Al-Si precipitation in TC1 and TC4 temperature curve probably resulted from accidental variation in cooling rate from one experiment to the other. Hence, the simulated A/A_0 curve, which is calculated based on TC4 temperature, is not helpful in explaining the EE2. If the time corresponding to Al-Si binary precipitation in TC4 temperature curve is shifted to that in TC1 temperature curve (in a similar way that has been done for the Al precipitation) then the simulated A/A_0 will show a plateau region in the time range of points **5** to **6**. As a result the shrinkage of the foam will nearly stop at point **5**. However, the observed expansion between point **5** to **6** (i.e., EE2) requires a source of gas. Hydrogen production from TiH_2 can contribute to some extent. It has been shown in Fig. 3.14 that EE2 is present for all HT and is nearly constant. Hence, the hydrogen production from TiH_2 cannot be the reason of EE2 as it decreases with increasing discharge of H_2 from TiH_2 . Moreover, EE was also observed in blowing agent free foams (see Figs. 3.31–33). These observations suggest that precipitation of hydrogen is the main reason of EE2. The amount of gas shrinkage during EE2 can be calculated by simulating the gas shrinkage curve during EE2 in a similar as explained for EE1, see Fig. 4.10.

Beyond point **6** there is no significant shrinkage. The shrinkage of the foam no longer follows the gas law due to the high amount of solid fraction generated during solidification. Note that the shrinkage of the foam can be affected in this way by the beginning of solidification. It is not clear from which point the shrinkage of the gas will no longer follow the gas law. However, it is clear that towards the end of solidification the shrinkage will be highly hindered by the amount of solid.

4.5 Individual influences on extra expansion

EE can only be understood by considering simultaneous action of multiple mechanisms. The parameters that influence EE are illustrated schematically in Fig. 4.11. The independent parameters are given by the choice of the experiments, whereas the dependent parameters are automatically determined once the independent parameters are chosen. For example, for any alloy, HT can be varied independently. However, the amount of remaining H_2 in TiH_2 that is present at the end of HT gets automatically fixed by the choice of the alloy and HT. The parameters given in Eq. 4.10 directly influence EE. However, they are influenced by several dependent and independent parameters. Because of the complicated interwoven nature of the parameters in Fig. 4.11 their contributions cannot be discussed separately. Different influences of one parameter will be addressed separately. In all the subsequent discussions, the illustration shown in Fig. 4.11 should be consulted to see the integration of different

contributions of each parameter. For the sake of simplicity some interconnections—those are less relevant—are avoided from the illustration; they will be mentioned in the text.

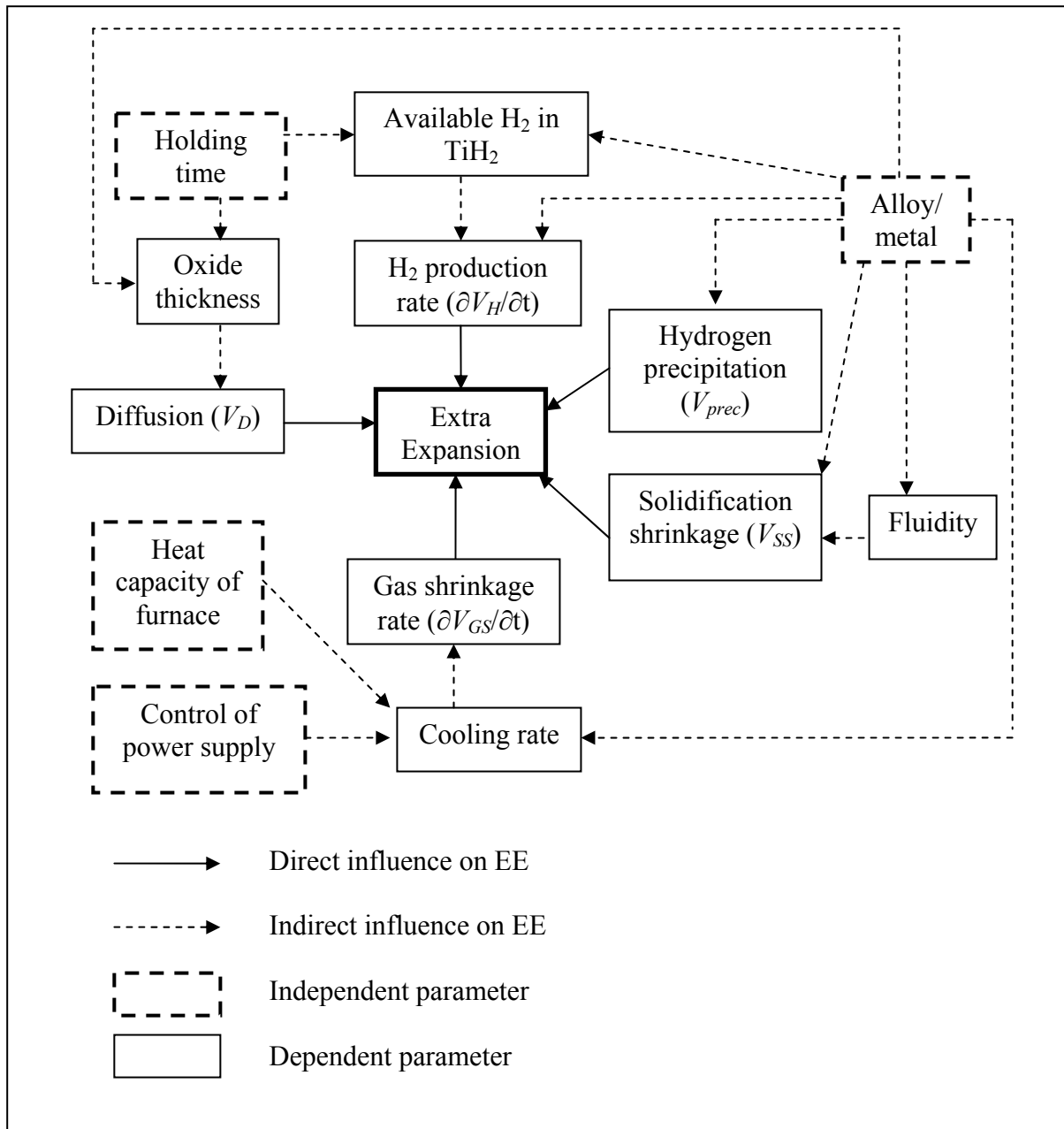


Figure 4.11. Schematic illustration of the parameters that influence extra expansion (EE).

4.5.1 Holding time

Let us assume that only two phenomena occur during solidification of foam: the first, hydrogen production from TiH₂; the second, gas loss due to out-diffusion of hydrogen. The resultant effect of their contribution is shown schematically in Fig. 4.12. If the amount of hydrogen production is more than out-diffusion, then EE will take place. Otherwise, foam will just show shrinkage. Note that the curves in Fig. 4.12 do not follow any equation. The

decrease in hydrogen production with HT is reasonable assumption according to the trend shown in Fig. 4.4, which shows the hydrogen production as a function of heating time. The same has also been mentioned in section 4.3.1. The rate of gas loss due to out-diffusion is expected to decrease with increase in HT as we will see in the next paragraph.

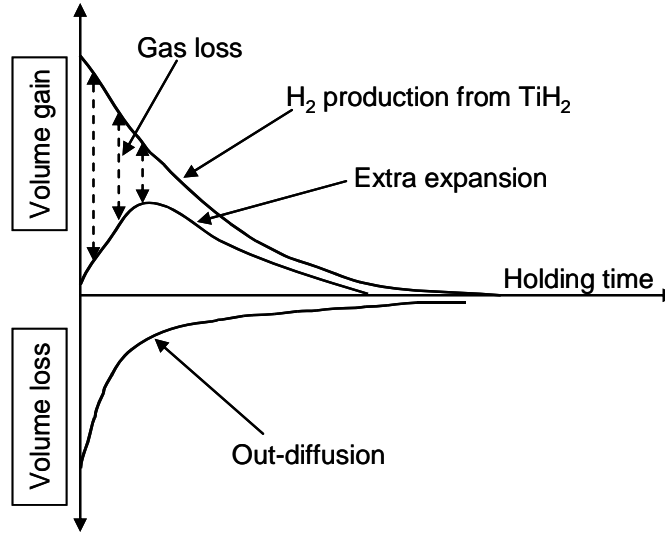


Figure 4.12. Schematic illustration of extra expansion in terms of hydrogen production from TiH_2 and out-diffusion of hydrogen. Other volume loss and gain factors are ignored.

For a given alloy (e.g. AlSi6Cu4) and cooling rate (e.g. natural cooling), $\partial V_{\text{prec}}/\partial t$, $\partial V_{\text{SS}}/\partial t$ and $\partial V_{\text{GS}}/\partial t$ in Eq. 4.10 are constant for all HT. Therefore, the variation in EE with HT shown in Fig. 3.14 (for AlSi6Cu4 alloy solidified with natural cooling) can be attributed to the change in $\partial V_{\text{H}}/\partial t$ and $\partial V_{\text{D}}/\partial t$ with HT. It has already been mentioned in section 4.3.1 that $\partial V_{\text{H}}/\partial t$ decreases with HT. It has been shown in section 4.3.6 that the rate of out-diffusion of hydrogen is mainly controlled by the presence of the oxide skin on the outer surface of foam. The thickness of the oxide skin is expected to increase with HT as reported in [76]. Hence, according to Eq. 4.6 the rate of out-diffusion ($\partial V_{\text{D}}/\partial t$) will decrease with increase in HT. This is shown in the schematic in Fig. 4.12. When shrinkage of foam starts, the slope of the shrinkage depends on the value of $\partial V_{\text{H}}/\partial t$ and $\partial V_{\text{D}}/\partial t$. For shorter HT, e.g. 50 s, the slope is less than the slope for longer HT due to the higher production rate of hydrogen, see Fig. 3.12. As the production rate of hydrogen drops after long HT, the initial shrinkage slope increases. The exact amount of change in $\partial V_{\text{D}}/\partial t$ cannot be predicted. However, it is clear that $\partial V_{\text{D}}/\partial t$ decreases with increasing HT.

Due to a relatively higher value of $\partial V_{\text{D}}/\partial t$ for 0 s HT (than for longer HT) EE1 starts at a later stage of solidification, i.e., at lower temperature. As HT increases, $\partial V_{\text{D}}/\partial t$ decreases and therefore the gas loss can be compensated at an early stage during solidification. Consequently, the start of EE1 shifts towards a higher temperature. It can be seen in Fig. 3.13, despite the fluctuations in data, that EE1 starts at lower temperature for 0 s HT and subsequently the starting temperature increases with HT. $\partial V_{\text{H}}/\partial t$ is also a function of

temperature. Hence, when EE1 starts at higher temperature, $\partial V_H/\partial t$ increases which in turn increases EE1. Therefore there is an increasing trend in EE1 value from 0 to 200 s HT, see Fig. 3.14. With further increase of HT, $\partial V_H/\partial t$ decreases due to continuous discharge of H_2 from TiH_2 . $\partial V_H/\partial t$ and $\partial V_D/\partial t$ act together in tandem and keep the EE1 value at an approximately constant level for 200 to 450 s HT. However, the schematic in Fig. 4.12 suggests that there should be a peak in EE1. The error bars shown in Fig. 3.14 are so large that a peak in EE1 value can also be assumed in-between 150 s and 500 s HT. The decreasing rate of diffusion is the reason why the initial slope of shrinkage—before EE1—decreases for HT longer than 200 s, see Figs. 3.12 and 3.21. Beyond that—although diffusion decreases—hydrogen production decreases further and EE1 shows a decreasing trend up to 500 s HT, see Fig. 3.14. This decreasing trend is also shown in Fig. 4.12. For longer HT than 500 s, $\partial V_H/\partial t$ is not enough to compensate the gas loss rate. As a result, there is no EE1 for HT greater than 500 s (Fig. 3.14). The observed EE1 can only be explained qualitatively. However, no value can be assigned to $\partial V_H/\partial t$ and $\partial V_D/\partial t$. This rules out any quantitative assessment of EE. The knowledge of TiH_2 dissociation kinetics and oxidation rate in each alloys are required to be able to make any quantitative evaluation of EE.

With decreasing temperature the volume of the foam decreases according to the gas law. Consequently, the surface area of the foam is also expected to decrease. Without the presence of an outer oxide skin, the metallic melt would shrink uninterruptedly and at any time the outer surface of the foam would remain in a stretched condition. The oxide formed on the foam surface stabilizes the film, and due to its solid state merely contracts during solidification via thermal contraction. Oxide skin conserves the outer surface area of the foam, and thereby results in a corrugation of the outer surface [65]. At the point when EE starts the resistance against stretching is less. In fact, there is little resistance from the outer surface if EE does not increase the expansion of the foam beyond the original expansion of the foam, i.e., the expansion value at the onset of cooling. The situation inside the foam, however, does not change. In this way, EE is somewhat different from the original expansion stage of the foam since the resistance from outer layer varies significantly from one to another.

It has been shown that the observed EE1 can be explained by the combined mechanism of decomposition of TiH_2 and out-diffusion of gas. In a similar way one would expect a similar behaviour for EE2. For HT of 0–500 s EE2 follows a similar trend like EE1. In contrast, for HT more than 500 s, EE2 remains at a constant level of 1.5%. If TiH_2 discharges H_2 continuously then with increasing HT EE2 would show a decreasing trend until the value became zero at some HT, see Fig. 4.12. The constant nature of EE2 from 600–3000 s HT therefore indicates that hydrogen production from TiH_2 cannot be the reason. Precipitation of hydrogen (V_{prec}) from the alloy during solidification is expected to be the main reason. V_{prec} is constant for a given alloy and does not depend on the HT or nature of cooling. As a result, EE2 remains at a constant level for 600–3000 s HT. Note that V_{prec} is also present for 0–500 s HT. It is superimposed with the hydrogen production from TiH_2 . So, the value of EE2 higher than 1.5% is contributed by the hydrogen production from TiH_2 .

4.5.2 Alloy composition – gas evolution from dissolved hydrogen

Hydrogen dissolution is an intrinsic property of an alloy. If sufficient amount of hydrogen is available, then every time the alloy is melted it dissolves the theoretical amount of hydrogen which precipitates while solidifying. The adsorbants present in the metal powders are thought to be the sources of gas in foams produced via PIF method as described in section 4.2.2. H_2 and H_2O are two of the adsorbants that can present in the metal powder surface. While the precursor is melted the aluminium metal can dissolve the H_2 that is already present. Alternatively, aluminium reacts with the H_2O vapour that is produced during heating from the adsorbed H_2O . This produces hydrogen according to the reaction [106]:



The hydrogen is dissolved in the liquid aluminium in atomic form [92, 106]. This is the mechanism of hydrogen dissolution in aluminium casting even if there is no obvious hydrogen atmosphere. Hence, when the blowing agent free precursor is melted in PIF method, it also dissolves hydrogen. The precipitation of this dissolved hydrogen during solidification results in EE. The amount of EE was observed to be about 2.2%, see Fig. 3.31. This can be considered similar to the EE2 in AlSi6Cu4 foam containing TiH_2 ; the values do not match exactly though. It has already been mentioned that the image analysis software AXIM is not efficient to measure small values accurately. This is because of the limitation of detector resolution, 12.5 μm . So, some small error could be present in all measurements, and, hence, 1.5 and 2.2% can be considered as similar values. Note that these two EE were measured for foams produced in different furnaces: one in a lamp and the other in a pressure furnace. So, the measurements are not identical and thus some deviation in absolute value can be expected.

It is shown in Fig. 3.32 that every time the same foam is solidified it produces EE. This again proves that this EE is an intrinsic nature of the alloy. However, the decreasing value of EE in subsequent solidifications is noticeable. During the first solidification the value (2.3%) is similar to that seen in another identical measurement (see Fig. 3.31). During the initial melting the amount of hydrogen dissolved would be maximal due to the presence of higher amount of adsorbants. In contrast, in the subsequent melting sequences the amount of adsorbants is obviously less having been already used up in the first melting. In addition, due to the closed-cell structure the interior of the foam has no access to the atmospheric H_2O . Therefore, during the second and third melting sequences the amount of dissolved hydrogen is less than that during the first melting sequence. Consequently, the amount of EE decreases in all subsequent solidifications. If the subsequent solidifications are performed with slower cooling rate, then the EE can be higher than that observed during the first solidification, see Fig. 3.33. The effect of cooling rate will be discussed in section 4.5.5.

The amount of hydrogen precipitated is given in section 4.3.2. This amount is comparable to the observed fixed amount of EE2. However, the total dissolved hydrogen does not precipitate at a single point, see Figs. 4.6–4.7. Before it can precipitate, the hydrogen atom has to migrate from its site to a nucleation site; this process is diffusion-controlled. So, the

precipitation of hydrogen is controlled by the kinetics of diffusion. For very slow cooling, the dissolved hydrogen in the system would follow the theoretical solubility limit. However, in practice this is not the case. As a result, the system is usually supersaturated with hydrogen while solidifying. During solidification of foam the precipitation of hydrogen could thus be delayed for few to several seconds depending on the cooling rate. The precipitation of the total hydrogen, or most of it, can be shifted to the Al-Si binary phase transformation zone. In this way the theoretical amount of dissolved hydrogen is enough to explain the observed EE2 in blowing agent containing foams, and the EE in blowing agent free foams. Zn dissolves very small amount of hydrogen as shown in section 4.3.2. Thus, the EE produced by hydrogen precipitation in Zn foam would be hardly visible.

The amount of solid phase at the end of Al-Si binary precipitation in AlSi6Cu4 is about 90%. This hinders any expansion and shrinkage of the foam at this stage as stated earlier in section 4.4. Therefore, corresponding to the ternary phase precipitation in AlSi6Cu4 alloy any further EE (i.e., EE3) is possible neither by hydrogen production from TiH_2 nor by hydrogen precipitation.

4.5.3 Alloy composition – fluidity of metallic melt

The amount of V_{prec} from AlSi6Cu4 is about 2.5 vol.%, see section 4.3.2. The amount of V_{ss} during Al-Si binary phase precipitation in AlSi6Cu4 alloy is about 2 vol.%, see Fig. 4.9. Consequently, a part of the V_{prec} must be used to compensate V_{ss} before resulting in EE. This suggests that the EE produced by V_{prec} cannot be higher than 0.5%. In contrast, the observed constant EE2 (i.e., at HT longer than 500 s) in AlSi6Cu4 and EE in blowing agent free foams suggest the effect of V_{prec} must be higher. To address this apparent contradiction, the fluidity of the metallic melt should be taken into account. Fluidity of the melt can modify the effective V_{ss} . Fig. 4.11 shows the interconnection between alloy, fluidity and solidification shrinkage.

The ability of the molten metal to continue to flow while temperature drops and even when it is starting to solidify is known to be an important factor that controls the quality of casting products. The measure of the ability to flow is referred to as *fluidity*. Fluidity of pure metals and eutectics that freeze at a single temperature is different from that of alloys which freeze over a temperature range. Two different solidification types are referred to as *skin freezing* and *pasty freezing*. Al and Zn can be considered as skin freezing systems, while AlSi6Cu4, AlSi7, AlCu13Mg4, AlCu13Mg1 and AlCu20Mg5 are of the pasty freezing type. AlSi11 is close to the Al-Si eutectic, so it is closer to the skin freezing type. During solidification of skin freezing alloys the solidification front moves as planar surface from the cold wall to the centre of casting. In contrast, for pasty freezing alloys dendrites form at cold surfaces and grow towards the interior of the casting [76]. Solidification of the metallic melt in the cell wall of foam can be considered a special type of casting, where the casting mould thickness is in the order of 100–300 μm . However, there is a fundamental difference: in

casting the heat is removed through the mould surface; in contrast, in case of a cell wall the heat is removed along the cell wall into the Plateau borders.

A schematic illustration of the solidification process inside a cell wall for a pasty freezing type metal is shown in Fig. 4.13. The liquid content of the cell walls is below that of the Plateau borders (PBs). Therefore, it is expected that cell walls solidify faster due to their low heat content. The direction of heat removal is indicated. The heat is removed from the cell walls to the PBs, and thereafter through the PBs to the outer surface of the foam. The dendrites are not likely to grow from the cell wall surface (i.e., the gas/liquid interface) as the heat is not removed through it. However, the presence of oxide skin of the cell walls could provide a potential nucleation site for dendrites. Consequently, dendrites could also grow from the cell wall, as seen in Fig. 3.38. The growth direction should be along the heat removal direction. Hence, in general dendrites will point towards the PBs; this is indicated in Fig. 4.13. The arms of the dendrites can be broken by the flow of the liquid. Broken arms can also act as nucleating sites for dendrites [76]. The dendrites nucleated from the broken arms appear as free floating dendrites those are not particularly attached to the cell wall surface. In addition, any floating oxide particle can also acts as nucleating site [100].

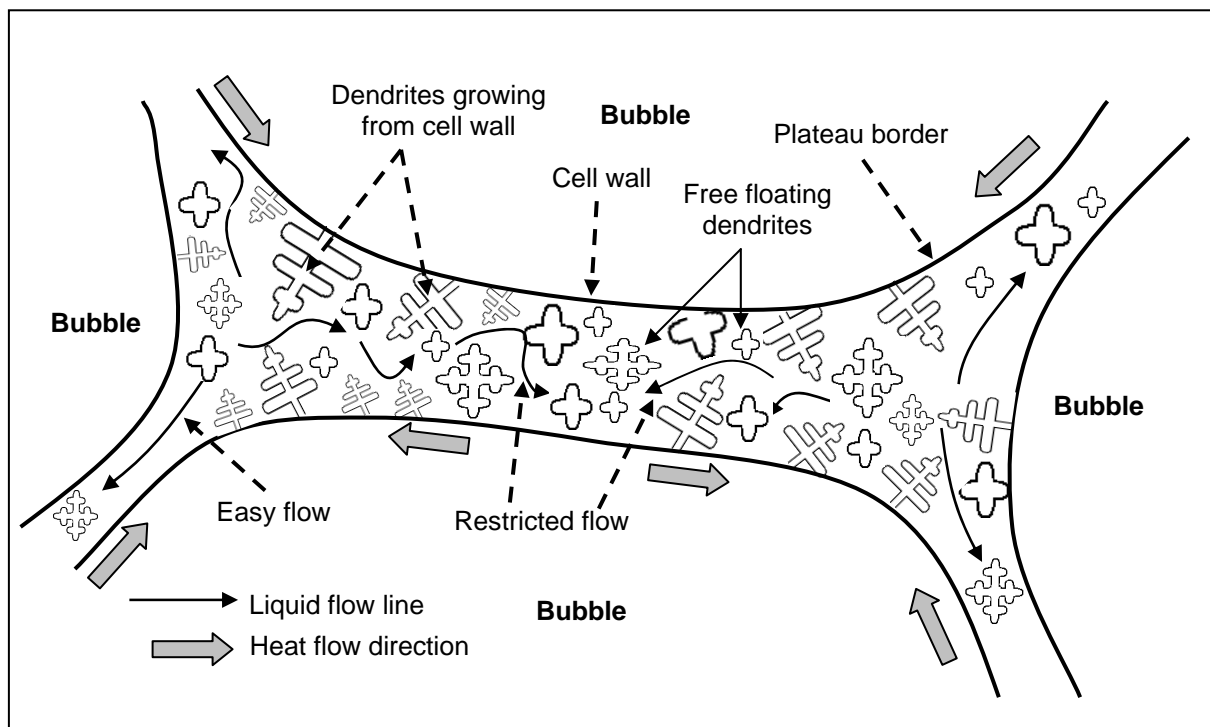


Figure 4.13. Schematic of liquid melt flow through cell walls in the semi-solid state. The solid arrows indicate flow lines.

In order to compensate the solidification shrinkage, the liquid metal flows to the growth front of dendrites. Flow lines of liquid metal are indicated in Fig. 4.13. It can be seen that where the amount of dendrites is less, flow is in general uninterrupted. On the contrary, at the central part of the cell wall, flow is heavily restricted due to the presence of dendrites. The volumetric flow rate is proportional to the fourth power of radius of the flow channel [107].

As dendrites grow further, the flow channel becomes smaller resulting in further decrease in flow rate. At some point during solidification the individual dendrites start to impinge their neighbours. This is known as the *dendrite coherency* [75]. The thickness of the cell walls is comparable to the length of the dendrites as shown in Fig. 3.38. As a consequence, the system can quickly reach the dendrite coherency limit. The volume fraction of the solid at which the coherency limit is reached is called *coherency fraction solid* (f_s^{coh}). It has been reported that for a cooling rate of 0.7 K/s f_s^{coh} in AlSi7 and AlCu4Si7 (i.e., close to AlSi6Cu4) alloy f_s^{coh} is 0.22 and 0.21, respectively [75]. It can be estimated from the phase diagram of Al-Si-Cu (see Fig. 4.1) that during the solidification of AlSi6Cu4 the fraction of solid will be about 0.50 at the point the solidification reaches the Al-Si monovariant line, i.e., point **b** in Fig. 4.1. Hence it can be assumed that during solidification of AlSi6Cu4 foam the dendrite structure of the cell wall will reach the coherency limit before the start of Al-Si binary phase precipitation.

At the point dendrite coherence is reached the inside of the cell wall can be considered as an interconnected porous structure. In order to compensate the volume contraction during solidification, the liquid metal has to find its way through this porous medium which slows down its flow. When permeability gets too small the flow stops; from this point the formation of micro-porosity or shrinkage porosity takes place. Shrinkage porosity is irregular in shape and follows the geometry of the dendrites, see Fig. 3.38. However, irregular pores may also be a combined effect of gas and shrinkage porosities [106]. If the solidification shrinkage (V_{ss}) is distributed in the cell wall microstructure as porosity, then the foam as a bulk would not reveal any solidification shrinkage when measured from the outer contour (i.e., the X-ray projected image) of the foam. The concept is illustrated schematically for skin freezing and pasty freezing type metals in Fig. 4.14. The presence of shrinkage porosities is the evidence that outer contour of the foam does not experience the theoretical amount of solidification shrinkage. As a result, the total amount of hydrogen precipitation can produce EE (EE2 for blowing agent containing foam) in AlSi6Cu4 alloy without having to fully compensate the solidification shrinkage.

The amount of hydrogen precipitation (V_{prec}) in Al foams is about 5 vol.% (see Table 4.5), higher than that of AlSi6Cu4 foam. Still it does not show any significant EE. The high solidification shrinkage (7.14 vol.%, see Table 4.6) is possibly the reason. As solidification of Al is of the skin freezing type, most part of the theoretical shrinkage would be manifested as bulk shrinkage instead of shrinkage porosities. Similarly, for Zn shrinkage porosity would be less due to its skin freezing type solidification behaviour. In AlSi11 alloy V_{prec} is 1.86 vol.% (see Table 4.5). The solidification shrinkage is higher than this value, 5 vol.% as mentioned in section 4.3.4. AlSi11 is close to the binary eutectic, and therefore has a high fluidity. Consequently, the amount of shrinkage porosities will be less. This discards any possibility of EE due to V_{prec} in AlSi11 alloy foam.

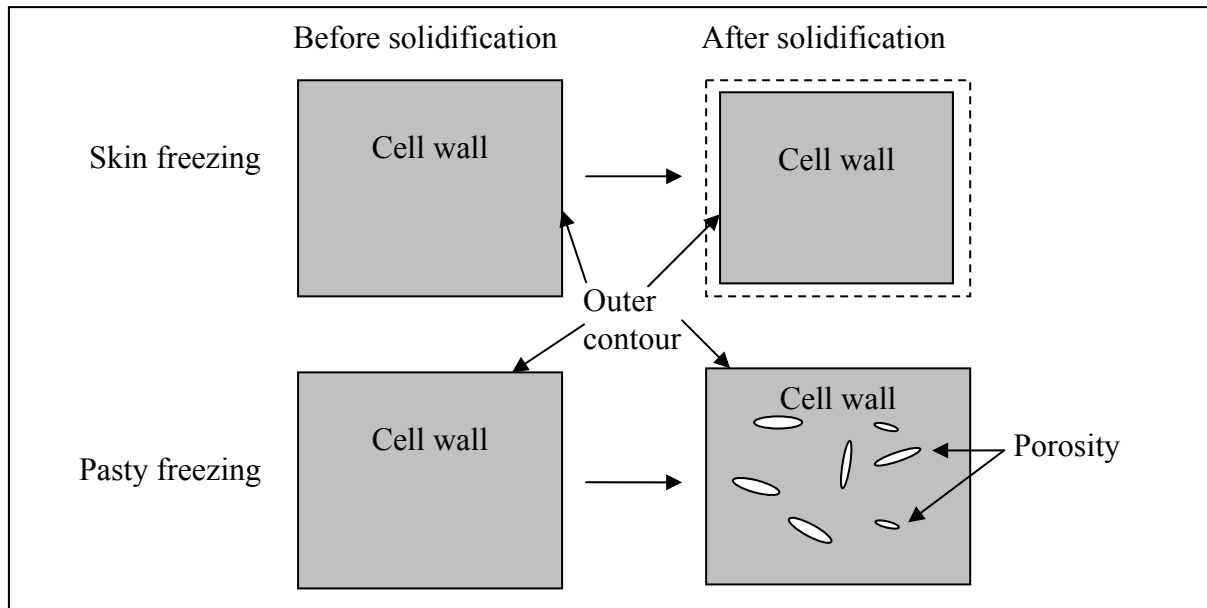


Figure 4.14. Schematic of the effect of different kinds of solidification shrinkage on the cell wall microstructure in skin and pasty freezing type metals.

4.5.4 Alloy composition – rate of gas production from TiH_2

The foaming alloy has manifold effects on EE, see Fig. 4.11. Some of them—hydrogen precipitation, solidification shrinkage and fluidity—have already been addressed in the previous sections. The effect of alloy composition on the out-diffusion by affecting the oxide thickness has been mentioned in section 4.3.6. Effect of alloying elements on diffusion will not be considered, since in the presence of an oxide skin the diffusion coefficient of hydrogen in metal does not play any significant role. Other effects of the alloy composition are the amount of available hydrogen in TiH_2 and hydrogen production rate (see Fig. 4.11) as we will see in the next paragraph. The effect of the alloy composition on cooling rate will be addressed in section 4.5.5.

The difference in melting point affects the amount of the remaining hydrogen in TiH_2 for a given HT. Remaining hydrogen directly controls the hydrogen production rate ($\partial V_H / \partial t$). Melting sequences of four alloys are schematically given in Fig. 4.15. The foaming temperature is the constant for all. During heating and cooling the time spent in each phase (solid, semi-solid and liquid) is not same for all alloys. When the precursor material is in the solid state, the dissociation of TiH_2 into Ti and H_2 is the lowest. According to Le Chatelier's principle, further dissociation of TiH_2 is not possible if the produced H_2 is not removed from the reaction site. H_2 is removed from the precursor either by diffusion, which is the lowest in solid state, or through the interconnected pores that open at the outer surface of the precursor. As a result, dissociation is restricted in the solid state. As liquid phase appears, the dissociation rate increases. When the metal of the foam is completely liquid the dissociation rate becomes very high. For a given heating rate, HT and cooling rate the time spent in the

liquid phase depends on the alloy. Dissociation is maximal in AlSi11 alloy since it spends a long time in the liquid state due to its low liquidus temperature when cooling down from the foaming temperature. As a result, when AlSi11 foam starts solidifying, i.e., below the liquidus temperature, the amount of remaining H_2 (in TiH_2) in the foam is less compared to, e.g., AlSi7. If one considers the effect of remaining H_2 (in TiH_2) on EE then it is expected that AlSi7 will show higher EE than AlSi11. When AlSi6Cu4 and AlSi7 alloys are compared, both have similar liquidus temperatures, 610 °C and 615 °C. However, AlSi6Cu4 has a solidification range of 85 K, much higher than the range of AlSi7 (38 K). For a fixed foaming temperature, the discharge of TiH_2 is more in AlSi6Cu4 than in AlSi7 alloy foam. Consequently, at the start of solidification, the amount of remaining TiH_2 is higher in AlSi7 than in AlSi6Cu4. This causes a higher amount of EE in AlSi7 than in AlSi6Cu4 under identical conditions. For example, for 200 s HT EE1 in AlSi7 and AlSi6Cu4 are about 16 and 4%, respectively (see Figs. 3.14 and 3.16(b)). EE2—which is caused mainly by hydrogen precipitation—is almost the same in both alloys since the level of dissolved hydrogen is similar in these two alloys, see section 4.3.2.

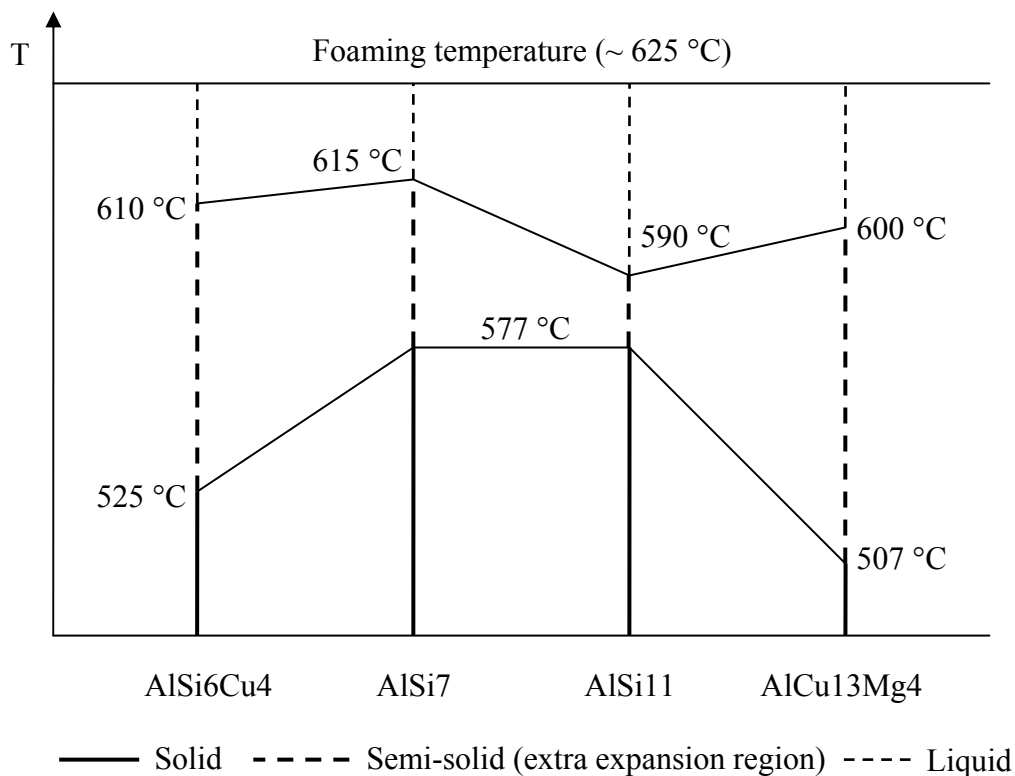


Figure 4.15. Schematic illustration of the temperature ranges of solid, semi-solid and liquid region of various alloys with respect to a fixed foaming temperature. For each alloy theoretical liquidus (top) and solid (bottom) temperatures are indicated.

AlCu13Mg4 alloy has a longer semi-solid range (93 K) and lower liquidus temperature compared to those in AlSi7 and AlSi6Cu4. Both factors act together to enhance the dissociation of TiH_2 in this alloy. Therefore, AlCu13Mg4 will have less EE than

AlSi6Cu4 and AlSi7. In fact, no EE was observed in this alloy under natural cooling condition. In contrast, AlSi11 alloy foam shows EE for 0 s HT mainly due to less dissociation of TiH₂ in the semi-solid state, the range of which is only 13 K. The amount of remaining H₂ is higher in Zn compared to Al foam due to the lower melting point of Zn. The foaming temperature of Zn was 430 °C (melting point of Zn is 420 °C), while that for Al was more than 660 °C. It is expected that at the start of solidification, Zn foam will contain a higher amount of remaining H₂ (in TiH₂) than Al foam. For this reason, EE was observed in Zn foam (EE ~6%) but not in Al foam. The amounts of TiH₂ in Zn and Al are similar by wt.%: 0.5 and 0.6 wt.% in Al and Zn, respectively. As Zn (7.14 g.cm⁻³) has a higher density than Al (2.7 g.cm⁻³) the vol.% of TiH₂ in Zn foam is about 3 times higher than that in Al foam. This could be one of the reasons of high EE in Zn foam. One can, however, argue whether Zn foam will show EE if the vol.% of TiH₂ is same as in Al foam. Nonetheless, the presence of EE in Zn foam suggests that EE can also take place in foams containing a pure element.

In the previous paragraphs it has been shown that the hydrogen production rate is affected by alloy composition via variation in available hydrogen in TiH₂. The hydrogen production rate can also be affected directly by alloy composition, see Fig. 4.11. This is due to their different liquidus temperatures (and not due to their solidification range). Hydrogen production rate increases with increasing temperature [90]. EE occurs in the solidification range, i.e. during the semi-solid state of solidification as indicated in Fig. 4.15. Therefore, for a given amount of remaining hydrogen in TiH₂, the production rate of hydrogen at the beginning of solidification is higher for high melting alloys than that for low melting alloys. As a result, on the basis of their hydrogen production rate, high melting alloys are more likely to show higher EE than low melting alloys if the amount of available hydrogen is same in both cases.

Under natural cooling the choice of alloy can control the cooling rate ($\partial T/\partial t$), which in turn affects EE by influencing $\partial V_{GS}/\partial t$, see Fig. 4.11. Under identical cooling condition different alloys have different cooling curves, see Fig. 3.3(b). This is because of the different amount of latent heat release. For example, the cooling curve during Al precipitation in AlSi11 alloy is steeper than that in AlSi7 alloy. As a result, $\partial T/\partial t$ will be smaller for AlSi7 alloy, and thereby decreases the gas shrinkage rate. Consequently, EE will be higher in AlSi7 alloy foam. Compared to AlSi7, AlSi11 has a longer plateau during the Al-Si binary phase precipitation (577 °C). So, if the amount of remaining hydrogen is same, then AlSi11 would show higher EE₂ than AlSi7. However, due to the low amount remaining hydrogen and hydrogen precipitation, EE₂ was not observed in AlSi11 alloy except for 0 s HT. When the cooling curves of AlSi6Cu4 and AlCu13Mg4 are compared, it becomes evident that the cooling rate in the latter is higher. Therefore, it is more likely that AlSi6Cu4 alloy foam would show higher EE than AlCu13Mg4 alloy foam under identical condition.

The amount of dissolved hydrogen is higher in AlCu13Mg4 compared to that in AlSi6Cu4 and AlSi7 alloy, see Table 4.5. In spite of that, there is no EE₂ in AlCu13Mg4 either with blowing agent or without blowing agent. Due to the Al-Si binary reaction both AlSi6Cu4 and AlSi7 produce a plateau at the temperature corresponding to EE₂. In contrast,

AlCu13Mg4 has a small range of binary reaction phase (see Fig. 4.3). The latent heat release from this binary reaction cannot result in a plateau in the cooling curve. As a result, there is no EE2 corresponding to the binary reaction. Similarly, AlCu13Mg1 also has a small binary reaction temperature region, and therefore EE was not observed. Moreover, AlCu13Mg1 dissolves a smaller amount of hydrogen. That further prevents any possible EE. On the other hand, AlCu20Mg5 (without blowing agent) shows EE. The different solidification sequence could be the reason. The amount of hydrogen precipitation from this alloy is about 2.6 vol.% as estimated in section 4.3.2. There is no binary precipitation in this alloy. The solidification directly goes to the ternary eutectic point of Al-Cu-Mg system, see Fig. 4.3. Till the eutectic reaction point it could retain its entire dissolved hydrogen. According to the phase diagram, the approximate amount of liquid phase during eutectic reaction is 75%. Thus, the expansion of foam is still possible provided there is a gas source. The combination of hydrogen precipitation and liquid fraction of the foam could thus produce EE in AlCu20Mg5 alloy foam. Note that AlCu13Mg4 shows 9 K temperature rise (recalescence effect) during ternary reaction as mentioned in section 3.1. Considering an average expansion of 200%, the expansion of the gas would be 2.3 vol.% due to the recalescence effect. Even so EE was not observed corresponding to the ternary reaction. This suggests that the foam contains high amount of solid phase which does not allow gas expansion.

4.5.5 Cooling rate

In the previous section it has been stated that the cooling rate can vary with alloy composition due to the difference in latent heat release. It can be seen that the change in alloy composition can simultaneously influence many parameters. This makes it difficult to separate the effect of cooling rate. It is evident that cooling rate is one of the major factors which can influence the EE by controlling the gas shrinkage rate ($\partial V_{GS}/\partial t$). In order to verify the effect of cooling rate it is essential to perform solidification with different cooling rates and without changing any of the independent parameters, which are the alloy composition, HT and heat capacity of the furnace.

This was performed for a fixed alloy (AlSi7) and HT using the lamp furnace. Different cooling rate was achieved by manually controlling the power of the lamps (for details see section 3.5.2). Setting up a fixed cooling rate in the temperature controller would give a better control on cooling rate. However, an automatic ramp in the controller tries to maintain a constant cooling rate either by providing or extracting power at small intervals. When the latent heat is released during solidification, the controller would decrease the power in order to counteract the extra heat. Consequently, the influence of latent heat on EE will be suppressed. By reducing the power of the lamps to lower values does not impose any such constraint. The values of EE1 in AlSi7 alloy foam for different cooling rate (see Fig. 3.28) proves that cooling rate has significant influence on EE. As stated in section 4.4, $\partial V_{GS}/\partial t$ decreases with decreasing $\partial T/\partial t$, which in turn increases EE. The results shown for different

cooling rate agrees with this theory. However, at a cooling rate 1.28 K/s EE1 appears to be higher than the lower cooling rate value and does not agree with the general trend seen for other cooling rates, see Fig. 3.28.

In different cooling rate experiments for AlSi7 foam, apart from the rate of hydrogen production and gas shrinkage, the rate of all other gas loss and gain parameters can be assumed to be constant. Eq. 4.10 is expressed as:

$$\frac{\partial V_{in}}{\partial t} = \frac{\partial V_H}{\partial t} - \frac{\partial V_{GS}}{\partial t} + const. \quad 4.13$$

where,

$$\frac{\partial}{\partial t}(V_{prec} - V_{SS} - V_D) = const. \quad 4.14$$

The value of EE1 can be obtained by integrating Eq. 4.13 over the entire time period of EE1. The integration is expressed as:

$$EE = \int_0^t \frac{\partial V_{in}}{\partial t} dt \quad 4.15$$

where, t is the total time of EE1. Note that EE measured from the A/A₀ curve gives the resultant value obtained after subtracting the volume loss factors from the volume gain factors. To estimate the real volume gain during EE one has to take into account the contribution from the volume loss factors.

The cooling curves for three different cooling rates measured inside the foam by a TC4 thermocouple is shown in Fig. 3.26. The corresponding foaming behaviours are shown in Figs. 3.16(a) and 3.24-25. The time range shown for each cooling curve in Fig. 3.26 is the time duration of Al precipitation, i.e., the time in-between the first and second minimum in the cooling rate curve. It is clear that the time of Al precipitation gets extended at lower cooling rate. Since EE1 takes place during Al precipitation, the time period of EE1 is also expected to increase. It has already been mentioned in section 3.5.2 that the duration of EE1 increases with decreasing cooling rate. As the total time t in Eq. 4.15 increases, the integration results in a higher EE1. If EE1 is normalized by its time duration then one would expect similar value for all cooling rate. The time-normalized EE1 value in Fig. 3.29 agrees with this hypothesis. This implies that the enhanced value of EE1 at lower cooling rate is mainly because of the extended period of EE1. Note that the time-normalized EE1 corresponding to the natural cooling rate also agrees with the trend shown by the other cooling rate data. Hence, the higher time period of EE1 at natural cooling rate is the main reason of high value of EE1 (see Fig. 3.28). The time-normalized EE for different HT under natural cooling in AlSi6Cu4 (Fig. 3.15) shows the same trend as shown by the EE vs. HT behaviour in Fig. 3.14. This suggests that for a given cooling rate the change in EE with HT is not because of the change in duration of EE.

The similar effect of cooling rate on EE1 was observed in AlSi6Cu4 alloy. The combined effect of cooling rate and HT can be seen in Fig. 3.22. The time-normalized EE1 in AlSi6Cu4 also shows nearly constant value for all cooling rate, a similar behaviour as seen in AlSi7 alloy. The same effect of cooling rate was also observed on Zn alloy foam; an EE of

10.3% was observed for a cooling rate of ~ 0.6 K/s. Although no EE was observed under natural cooling in AlCu3Mg4 alloy, it showed 5.4% EE for a slow cooling rate (0.1 K/s). At slower cooling rate, AlSi11 continues to expand after the onset of cooling (see Fig. 3.30). The absence of EE could be the possible overlapping with this expansion stage.

It was observed that foams that solidified at a slower cooling rate exhibit higher collapse after EE1 due to outer surface bubble rupture (see Fig. 3.27). At slower cooling rate the foam spends more time at higher temperature which leads to higher oxide thickness at the outer surface. The oxide skin does not allow the shrinkage of the cell wall metal. This generates a stress at the oxide/metal interface. Due to its brittle nature AlSi7 cannot withstand the tensile stress and the cell wall ruptures [65]. In contrast, for high cooling rate the oxide is thinner and therefore less stress is imposed on the cell wall. Hence, the number of ruptures observed at higher cooling rate is less.

4.5.6 Heat capacity of furnace

It has already been verified that the cooling rate has a major influence on EE. The heat capacity of the furnace can significantly change the cooling rate. The lamp and pressure furnace used in the present study have different heat capacities. The ceramic heater in the pressure furnace consists of conductive graphite printed on a silicon nitride (Si_3N_4) substrate. Si_3N_4 has a specific heat about $0.7 \text{ J.g}^{-1}.\text{K}^{-1}$ at room temperature [108]. The mass of the heater is about 17 g. So, as a rough estimate, the total heat capacity (C_p) of the heater is $\sim 12 \text{ J.K}^{-1}$. The cooling of the foam, which is foamed in pressure furnace, depends on the C_p of this heater. The mass of the steel tube, inside which foaming was performed in the lamp furnace, is about 45 g. The specific heat of steel at room temperature is $\sim 0.5 \text{ J.g}^{-1}.\text{K}^{-1}$ [109]. So, the C_p of the steel tube is $\sim 22.5 \text{ J.K}^{-1}$. Hence, it can be assumed that for the same heat removal rate the ceramic heater will have twice the cooling rate of the steel tube. The more negative slope in the cooling curve of Al—foamed using the pressure furnace—is the result of low C_p of the ceramic heater (see Fig. 3.3(b)). The increase in cooling rate in turn increases $\partial V_{GS}/\partial t$, and thereby decreases EE. So, according to the furnace property, EE is likely to be less for those foams produced in the pressure furnace. However, Al foam did not show EE even for the lower cooling rate. Insufficient remaining hydrogen seems to be the main reason.

4.6 Practical relevance of extra expansion and its effect on foam structure

When foam is solidified by natural cooling the expansion at the end of solidification is less than that achieved at the end of HT (e.g. see Figs. 3.9–11). In the manufacture of foam-filled sections foaming is performed inside a mould. The volume of the section limits the maximum possible expansion of the foam. For sufficient heating it is possible to fill the section;

however, when cooling is introduced, the shrinkage often results in gap in-between the wall of the section and the foam. If metallic or mechanical bonding is formed in-between the section wall and the foam then the gap can be avoided. In this case, however, mechanical stresses generate in the mould/foam interface. In either case, the mechanical properties of the foam-filled parts deteriorate. Slower cooling (than natural cooling) introduces high amount of EE. With higher EE the expansion at the end of solidification can be comparable to the maximum expansion achieved at the end of HT (e.g. see Figs. 3.20, 3.23 and 3.24–3.25). By introducing high EE, the gap between the mould and the foam can be minimized. Shrinkage in the solid state (i.e., after solidification) cannot be avoided anyway.

The effect of EE can also be seen as a way to obtain higher expansion using less thermal energy. A 30–40% expansion can be achieved by EE just by introducing a slow cooling rate. As EE occurs during the cooling stage, less energy is required compared to that consumed during the HT. In the present case, slow cooling was achieved by reducing the power of the lamps to lower values. If proper insulation is provided then slow cooling can be achieved even without supplying any energy during the cooling stage.

EE can result in adverse effects on the foam morphology. Therefore, before applying EE to obtain higher expansion one has to consider the final resulted structure of the foam. It has been observed that high EE induces structural defects in the final foam morphology by inducing cell wall rupture during solidification, Fig. 3.37. In contrast, when foam is solidified by natural cooling such types of defects were not observed. The liquid redistribution after rupture is largely dominated by the surface tension of the metallic melt. Due to the low viscosity of the melt the liquid movement is not significantly affected by the viscous force. For instance, if F_v and F_s are the viscous and surface tensional force then $F_v \approx \frac{1}{4} F_s$ [58]. The time of rupture in fully liquid metal foams has been measured as 400 to 1000 μs [58]. Consequently, if any cell wall breaks in the liquid state, the metallic melt of the ruptured cell wall is quickly redistributed and the geometry of the surrounding cells is adjusted to an equilibrium structure. Hence, the final foam structure should not contain broken cell walls. On the other hand, if rupture occurs during the semi-solid state then the viscous force can become dominant. The rupture event induced by EE takes place during the semi-solid state of cooling. The amount of the solid fraction gradually increases in the semi-solid state and thereby the effective viscosity of the melt. The high value of the effective viscosity slows down rupture. It has been shown in Fig. 3.36 that the rupture event is distributed over about 10 s. As temperature decreases during cooling the liquid metal may turn into solid before the redistribution of the material is over. In this way the final structure of the foam can reveal the partially ruptured cell walls and thereby results in structural defects as shown in Fig. 3.37.

It was observed that the distribution of the expansion inside foam is not homogeneous during EE, Fig. 3.34–3.35. Thicker cell walls may contain more TiH_2 . That can result in a larger EE in that part of the foam. The higher amount of melt in the thick cell walls releases more latent heat. The distribution of heat inside the foam is affected by its low thermal conductivity [110]. Everything together suggests that some part of the foam experiences larger expansion than that in other parts during EE. If the total amount of EE is, say, 30%

(i.e., for slow cooling), then the effective EE in some region inside the foam can exceed this value as indicated in Fig. 3.34. Consequently, some cell walls may suffer extensive stretching in the semi-solid state, which can cause rupture of that cell wall. Broken cell walls cause an adverse effect on the mechanical properties of foams.

By applying EE it is possible to fill a section; however, one has to consider the fact that this effect can decrease mechanical strength of the foam. In industrial production foams are produced as large blocks. This suggests that the cooling of foam will be automatically slowed down due to its lower conductivity. Hence, some EE cannot be avoided if the foam contains a high amount of hydrogen in the TiH_2 at the beginning of solidification. Hence a clear understanding of EE is necessary before foam manufacture is carried out. By a proper control of EE, it could be possible to avoid—or, at least to reduce—the structural defects in foams produced using blowing agents.

5 Summary and Conclusions

The formation, evolution and solidification of metal foams were studied using X-ray radioscopy. The main focus of this thesis was to investigate the behaviour of foam during solidification, i.e., during cooling. The PM route was employed to produce foamable precursors based on Al, Al-alloy and Zn. The precursors were heated and cooled inside X-ray transparent furnaces at various gas atmospheres and pressures. Their foaming behaviour was quantified by applying image analysis on radioscopic images acquired in-situ during the foaming and cooling process.

A hitherto unknown expansion stage was observed during solidification of metal foams (see section 3.3.1). This expansion has been referred to as extra expansion (EE) in this thesis. EE is an anomalous behaviour since the foam is expected to contract during solidification. The EE stage in binary and ternary alloys can be subdivided into two parts (EE1 and EE2) based on the definition given in section 3.3.3. Foaming experiments were carried out by varying alloy composition, holding time (HT, i.e., isothermal heating period), cooling rate of solidification, gas atmosphere and pressure in order to elucidate the mechanisms responsible for EE. Among the alloys, AlSi6Cu4 and AlSi7 were the main alloys used in this study.

The phenomena that occur simultaneously while foam solidifies can be classified into two categories based on their contribution to the volume change of foam: volume gain and volume loss factors (see section 4.3). EE takes place whenever the combined volume gain rate is more than the combined volume loss rate. The kinetic interplay of shrinkage of the hydrogen gas present inside the foam, the out-diffusion of hydrogen to the surrounding space and the production of new hydrogen from the blowing agent was identified as the main reason of EE (see section 4.4).

Cooling rate can vary intrinsically during solidification due to the production of latent heat released by the solidifying alloys. Therefore, different alloys experience different cooling rate by virtue of their various solidification stages. Alternatively, cooling rate was also varied manually by controlling the power of the furnace. While the gas shrinkage rate is controlled by the cooling rate, hydrogen production and out-diffusion are determined by the HT prior to cooling. Hydrogen production rate decreases with increasing HT within about 500 s. As the thickness of the outer surface oxide layer increases at longer HT, the out-diffusion of hydrogen becomes less.

In the absence of any outer oxide layer, an aluminium foam is expected to collapse in a few seconds (see section 4.3.6). In practice, a foam gets oxidised in the liquid state and due to the presence of oxides in the metal powders. A drastic collapse of Al foam was observed when the foaming was carried out under a very pure argon atmosphere.

It was observed for AlSi6Cu4 that as HT increases the value of EE1 initially increases, then becomes nearly constant and finally decreases. EE1 was not observed for HT longer than 500 s (see section 3.4.1). This trend in EE1 is a result of the interplay between hydrogen

production and out-diffusion as described in section 4.5.1. In contrast, EE2 was observed for all HT and almost constant at HT longer than 500 s. Blowing agent free foams—those produced by pressure induced foaming (PIF) method—also showed EE. The ever present constant value of EE2 in AlSi6Cu4 and the EE in blowing agent free foams are produced by hydrogen precipitation from the metallic matrix as it solidifies. Cooling rate showed significant influence on EE1 as demonstrated for AlSi7 alloy in section 3.5.2. EE1 increases as the cooling rate decreases. This is mainly because of the increased production of hydrogen as the solidification time is extended in case of slower cooling rates (see section 4.5.5). Besides HT and cooling rate, EE is also influenced by many other parameters (see Fig. 4.11). The occurrence of EE in various alloys and experimental conditions are summarized in section 3.10.

It was observed that higher EE—as seen in slowly cooled foams—induces defects in foam morphology (see section 3.8.1). This is due to the EE-induced rupture during solidification of the metallic melt inside the cell walls as described in section 4.6. The defects thus produced are similar in nature to those defects found in commercial aluminium foams produced using blowing agents. It has been postulated that the slow cooling of foams—while manufactured at large scale—could trigger EE which in turn can cause defects in the morphology. On that basis, knowing the nature of EE in those commercial foams may help to reduce the defects and thereby to improve the mechanical performance of the foam.

Appendix A – Fatigue of a laterally constrained closed cell aluminium foam

The compression-compression fatigue behaviour, both with and without lateral constraint, of commercial closed cell aluminium foams (namely Alporas) were investigated in this study. The constraint was applied using a steel sleeve. Prior to the fatigue tests, quasi-static compression tests were conducted in order to determine the plastic strength of the specimens. Complementary X-ray tomography was performed on specimens whose cyclic and quasi-static loading was interrupted.

A key feature of compression-compression fatigue in metal foams is the progressive strain accumulation, which leads to shortening of the specimens during fatigue. The plot of the accumulated strain, ϵ_a , vs. number of fatigue cycles, N , reveals three distinct stages. In stage I, rapid strain accumulation within the first few cycles ($N < 50$) of fatigue is noted. This is followed by stage II, where large number of cycles elapse with little strain accumulation. Then, at a critical number of cycles, N_c , the strain starts to accumulate rapidly again (stage III). In both the constrained and unconstrained cases, ϵ_a at the end of the stage I is similar. Also, the onset of stage II occurs at about the same N . However, marked differences are seen in N_c , with stage III being initiated relatively earlier in unconstrained samples followed by a rapid rise in ϵ_a . For constrained samples, stage III is not a continuous process, but shows periodic slow strain accumulation.

The difference in behaviour in stage III was ascribed to the noticeable hardening with plastic deformation observed under constraint during quasi-static loading, which in turn reduces the effective maximum stress experienced by the foam specimens during fatigue loading. X-ray tomograms suggest that the fatigue behaviour of the foams is less sensitive to morphological defects such as missing cell walls than the quasi-static mechanical properties such as plastic strength. In the case of quasi-static loading deformation usually initiates at large cells where one or more number of cell walls is missing.

The details of this work are not given in this thesis and the reader is referred to [81].

Appendix B – Hydrogen solubility calculation in aluminium alloys

Hydrogen solubility limits in liquid multicomponent aluminium alloys can be calculated using Wagner's interaction parameters derived from data on hydrogen solubility in binary aluminium alloy systems [97]. The logarithm of the hydrogen activity coefficient ($\log_{10}f_H$) in Al-H-Cu-Mg-Si alloys can be written as follows:

$$\log_{10} f_H = e_H^{Cu} (wt.\%Cu) + r_H^{Cu} (wt.\%Cu)^2 + e_H^{Si} (wt.\%Si) + r_H^{Si} (wt.\%Si)^2 + e_H^{Mg} (wt.\%Mg). \quad B.1$$

Here e_H^{Cu} , e_H^{Si} and e_H^{Mg} are the Wagner's first order interaction parameters for Cu, Si and Mg, respectively. r_H^{Cu} and r_H^{Si} represent the Wagner's second order interaction parameters for Cu and Si, respectively. The value of the interaction parameters at 973 K are given in Table B.1. f_H is expressed as:

$$f_H = \left[\frac{(wt.\%H)_{inAl-H}}{(wt.\%H)_{inAl-H-Cu-Mg-Si}} \right]_{T, P_{H_2}}. \quad B.2$$

The limit of hydrogen solubility in pure Al is given by [96]:

$$\log_{10} (wt.\%H)_{inAl-H} = -\frac{2691.96}{T} - 1.32. \quad B.3$$

At $T = 973$ K, $(wt.\%H)_{inAl-H} = 0.82 \cdot 10^{-4}$.

Table B.1

First order (e_H^X) and second order (r_H^X) interaction parameters for hydrogen solution in Al-H-Cu-Mg-Si alloys at 973 K and 101.3 kPa hydrogen partial pressure ($X = Cu, Si, Mg$) [96]

	Interaction parameters		
	Cu (< 32 wt.%)	Si (< 16 wt.%)	Mg (< 6 wt.%)
e_H^X	0.0334	0.0193	-0.066
r_H^X	-0.00065	-0.00045	—

Using the value of hydrogen solubility in pure aluminium and combining Eqs. B.1–B.2, hydrogen solubility limit in AlSi6Cu4, AlSi7, AlSi11, AlCu13Mg4, AlCu13Mg1 and AlCu20Mg5 alloys has been calculated in this thesis.

Appendix C - Calculation of out-diffusion of hydrogen from foam

The surrounding atmosphere of foam has almost zero partial pressure of hydrogen. The hydrogen partial pressure inside the foam is about 1 bar since the cells are filled with hydrogen. Note that if the surrounding pressure is 1 bar, the pressure inside the foam is slightly higher due to surface tensional force. However, that is negligibly small compared to 1 bar and therefore is ignored here. If a cell wall at the outer surface of foam is considered, then the Al melt at the inner surface of cell wall is saturated with hydrogen due its direct contact with hydrogen. The outer surface of the same cell wall, which is exposed to the surrounding atmosphere, has almost zero concentration as it tries to maintain equilibrium with the surrounding zero partial pressure of hydrogen. If a constant concentration gradient is considered across the cell wall and d_{wall} (in cm) is the cell wall thickness then the concentration gradient is S/d_{wall} (in $\text{cm}^3 \cdot \text{cm}^{-4}$), where S (in cm^3/cm^3 of Al) represents the equilibrium solubility of hydrogen.

If equilibrium condition of diffusion is assumed then according to the Fick's first law the flux (J) of hydrogen out-diffusion from the foam into the surrounding is given by

$$J = -D \cdot \frac{S}{d_{wall}} \text{ cm} \cdot \text{s}^{-1}, \quad \text{C.1}$$

where, D (in $\text{cm}^2 \cdot \text{s}^{-1}$) is the diffusion coefficient of H_2 in Al. The negative sign in Eq. 1 indicates gas loss due to out-diffusion. If A (in cm^2) is the outer surface area of the foam then the total rate of gas loss is $J \times A$. So for a foam volume V (in cm^3), the volume loss rate ($\partial V/\partial t$) as percentage of the total volume V follows the equation

$$\frac{\partial V}{\partial t} = -D \cdot \frac{S}{d_{wall}} \cdot A \cdot \frac{1}{V} \cdot 100 \text{ \%} \cdot \text{s}^{-1}. \quad \text{C.2}$$

If the foam is considered as sphere of radius r (in cm) then Eq. 2 can be simplified as

$$\frac{\partial V}{\partial t} = -\frac{3 \cdot D \cdot S}{d_{wall} \cdot r} \cdot 100 \text{ \%} \cdot \text{s}^{-1}. \quad \text{C.3}$$

References

1. J. Banhart, *Foam metal: the recipe*, Europhysics News, 1999, **30**: p. 17-20.
2. D. Weaire, S. Hutzler, *The physics of foams*, Oxford University Press, 1999.
3. M.A.De Meller, French Patent 615,147, 1926.
4. B. Sosnick, US Patent 2,434,775, 1948.
5. B. Sosnick, US Patent 2,553,016, 1951.
6. J.C. Elliott, US Patent 2,983,597, 1961.
7. J.F. Pashak, US Patent 2,935,396, 1960.
8. B.C. Allen, M.W. Mote, A.M. Sabroff, US Patent 3,087,807, 1963.
9. L.M. Niebylski, C.P. Jarema, US Patent 3,847,591, 1974.
10. S.E. Speed, US Patent 3,981,720, 1976.
11. J.W. Patten, US Patent 4,099,961, 1978.
12. G.J. Davies, S. Zhen, *Metallic foams: their production, properties and applications*, Journal of Materials Science, 1983, **18**: p. 1899-1911.
13. S. Akiyama, et al., US Patent 4,713,277, 1987.
14. I. Jin, L.D. Kenny, H. Sang, US Patent 4,973,358, 1990.
15. J. Baumeister, German Patent 4,018,360, 1991.
16. V.I. Shapovalov, US Patent 5,181,549, 1993.
17. H. Nakajima, *Fabrication, properties and application of porous metals with directional pores*, Progress in Materials Science, 2007, **52**: p. 1091-1173.
18. V. Gergely, B. Clyne, *The FORMGRIP process: foaming of reinforced metals by gas release in precursors*, Advanced Engineering Materials, 2000, **2**: p. 175-178.
19. D. Leitmeyer, H.P. Degischer, H.J. Flankl, *Development of a foaming process for particulate reinforced aluminum melts*, Advanced Engineering Materials, 2002, **4**: p. 735-740.
20. F. Garcia-Moreno, J. Banhart, German Patent 102,005,037,305, 2007.
21. D.M. Elzey, H.N.G. Wadley, *The limits of solid state foaming*, Acta Materialia, 2001, **49**: p. 849-859.
22. N.G.D. Murray, D.C. Dunand, *Effect of thermal history on the superplastic expansion of argon-filled pores in titanium: part I kinetics and microstructure*, Acta Materialia, 2004, **52**: p. 2269-2278.
23. M.F. Ashby, A.G. Evans, N.A. Fleck, L.J. Gibson, J.W. Hutchinson, H.N.G. Wadley, *Metal foams: A design guide*, Boston: Butterworth-Heinemann, 2000.
24. J. Banhart, *Manufacturing routes for metallic foams*, JOM Journal of the Minerals, Metals and Materials Society, 2000, **52**: p. 22-27.
25. J. Banhart, *Manufacture, characterisation and application of cellular metals and metal foams*, Progress in Materials Science, 2001, **46**: p. 559-632.

26. N. Babcsan, F. Garcia-Moreno, J. Banhart, *Metal foams-high temperature colloids part II: in situ analysis of metal foams*, Colloids and Surfaces A, 2007, **309**: p. 254-263.
27. B. Matijasevic, J. Banhart, *Improvement of aluminium foam technology by tailoring of blowing agent*, Scripta Materialia, 2006, **54**: p. 503-508.
28. A.R. Kennedy, *The effect of TiH₂ heat treatment on gas release and foaming in Al-TiH₂ preforms*, Scripta Materialia, 2002, **47**: p. 763-767.
29. A. Kennedy, V. Lopez, *The decomposition behavior of as-received and oxidized TiH₂ foaming-agent powder*, Materials Science and Engineering A, 2003, **357**: p. 258-263.
30. B. Matijasevic-Lux, J. Banhart, S. Fiechter, O. Görke, N. Wanderka, *Modification of titanium hydride for improved aluminium foam manufacture*, Acta Materialia, 2006, **54**: p. 1887-1900.
31. Z. Yang, J. Fang, B. Ding, *Effect of SiO₂ coating layer morphology on TiH₂ gas release characteristic*, Journal of Colloid and Interface Science, 2005, **290**: p. 305-309.
32. J. Fang, B. Ding, Z. Yang, K. Zhao, C. Gu, *The effect of SiO₂ and Al₂O₃ coating on the surface of TiH₂ powders on gas release*, Journal of Colloid and Interface Science, 2005, **283**: p. 1-4.
33. A. Irretier, J. Banhart, *Lead and lead alloy foams*, Acta Materialia, 2005, **53**: p. 4903-4917.
34. F. von Zeppelin, M. Hirscher, H. Stanzick, J. Banhart, *Desorption of hydrogen from blowing agents used for foaming metals*, Composites Science and Technology, 2003, **63**: p. 2293-2300.
35. C. Körner, M. Hirschmann, V. Bräutigam, R.F. Singer, *Endogenous particle stabilization during magnesium integral foam production*. Advanced Engineering Materials, 2004, **6**: p. 385-390.
36. D.C. Curran, *Aluminium foam production using calcium carbonate as a foaming agent*, Thesis, University of Cambridge, UK, 2003.
37. F. Garcia-Moreno, J. Banhart, *Foaming of blowing agent-free aluminium powder compacts*, Colloids and Surfaces A, 2007, **309**: p. 264-269.
38. C. Jimenez, F. Garcia-Moreno, J. Banhart, G. Zehl, *Effect of relative humidity on pressure-induced foaming (PIF) of aluminium-based precursors*, In: L. P. Lefebvre, J. Banhart, D. Dunand, editors, Proceedings of Porous Metals and Metallic foams, DEStech Publications, 2007: p. 59-62.
39. A. Kennedy, *Evolution of foam structure during the heating of extruded Al-Si-TiH₂ powders*, Journal of Materials Science Letters, 2002, **21**: p. 1555-1557.
40. L. Helfen, T. Baumbach, P. Pernot, P. Cloetens, H. Stanzick, K. Schladitz, J. Banhart, *Investigation of pore initiation in metal foams by synchrotron-radiation tomography*, Applied Physics Letters, 2005, **86**: p. 231907-1-3.

41. L. Helfen, T. Baumbach, H. Stanzick, J. Banhart, A. Elmoutaouakkil, P. Cloetens, *Viewing the early stage of metal foam formation by computed tomography using synchrotron radiation*, Advanced Engineering Materials, 2002, **4**: p. 808-813.
42. I. Duarte, J. Banhart, *A study of aluminium foam formation-kinetics and microstructure*, Acta Materialia, 2000, **48**: p. 2349-2362.
43. J. Banhart, H. Stanzick, L. Helfen, T. Baumbach, *Metal foam evolution studied by synchrotron radiography*, Applied Physics Letters, 2001, **78**: p. 1152-1154.
44. J. Banhart, D. Bellmann, H. Clemens, *Investigation of metal foam formation by microscopy and ultra small-angle neutron scattering*, Acta Materialia, 2001, **49**: p. 3409-3420.
45. D. Bellmann, H. Clemens, J. Banhart, *USANS investigation of early stages of metal foam formation*, Applied Physics A, 2002, **74**: p. S1136-S1138.
46. C. Körner, R.F. Singer, *Numerical simulation of foam formation and evolution with modified cellular automata*, In: J. Banhart, M. F. Ashby, N. A. Fleck, editors, Metal Foams and Porous Metal Structures, Bremen: MIT-Verlag, 1999: p. 91-96.
47. C. Körner, *Foam formation mechanisms in particle suspensions applied to metal foams*. Materials Science and Engineering A, 2008, **495**: p. 227-235.
48. C.C. Yang, H. Nakae, *The effects of viscosity and cooling conditions on the foamability of aluminum alloy*, Journal of Materials Processing Technology, 2003, **141**: p. 202-206.
49. H. Stanzick, J. Klenke, S. Danilkin, J. Banhart, *Material flow in metal foams studied by neutron radiography*, Applied Physics A, 2002, **74**: p. S1118-S1120.
50. F. Garcia-Moreno, N. Babcsan, J. Banhart, M. Haesche, J. Weise, *Analysis of metal foaming behaviour and development of foaming processes*, In: R. F. Singer, C. Körner, V. Altstädt, H. Münstedt, editors, Cellular Metals and polymers, Trans Tech Publications, Zuerich, 2005: p. 31-34.
51. V. Gergely, T.W. Clyne, *Drainage in standing liquid metal foams: modelling and experimental observations*, Acta Materialia, 2004, **52**: p. 3047-3058.
52. O. Brunke, A. Hamann, S. J. Cox, S. Odenbach, *Experimental and numerical analysis of the drainage of aluminium foams*, Journal of Physics: Condensed Matter, 2005, **17**: p. 6353-6362.
53. J. Banhart, *Metal foams: production and stability*, Advanced Engineering Materials, 2006, **8**: p. 781-794.
54. T. Wübben, H. Stanzick, J. Banhart, S. Odenbach, *Stability of metallic foams studied under microgravity*, Journal of Physics: Condensed Matter, 2003, **15**: p. S427-S433.
55. F. Garcia-Moreno, C. Jimenez, M. Mukherjee, P. Holm, J. Weise, J. Banhart, *Metallic foams under changing gravity conditions*, Colloids and Surfaces A, doi:10.1016/j.colsurfa.2009.03.010.
56. C. Körner, M. Arnold, R.F. Singer, *Metal foam stabilization by oxide network particles*, Materials Science and Engineering A, 2005, **396**: p. 28-40.

57. H. Stanzick, M. Wichmann, J. Weise, L. Helfen, T. Baumbach, J. Banhart, *Process control in aluminium foam production using real-time X-ray radioscopy*, Advanced Engineering Materials, 2002, **4**: p. 814-823.
58. F. Garcia-Moreno, A. Rack, L. Helfen, T. Baumbach, S. Zabler, N. Babcsan, J. Banhart, T. Martin, C. Ponchut, M. Di Michiel, *Fast processes in liquid metal foams investigated by high-speed synchrotron x-ray microradioscopy*, Applied Physics Letters, 2008, **92**: p. 134104-1-3.
59. C. Körner, Integral Foam Molding of Light Metals: Technology, Foam Physics and Foam Simulation, Springer-Verlag Berlin Heidelberg, 2008.
60. A.R. Kennedy, S. Asavavisitchai, *Effects of TiB₂ particle addition on the expansion, structure and mechanical properties of PM Al foams*, Scripta Materialia, 2004, **50**: p. 115-119.
61. G.S. Vinod Kumar, F. Garcia-Moreno, N. Babcsan, A.H. Brothers, B.S. Murty, J. Banhart, *Study on aluminium-based single films*, Physical Chemistry Chemical Physics, 2007, **9**: p. 6415-6425.
62. M. Haesche, J. Weise, F. Garcia-Moreno, J. Banhart, *Influence of particle additions on the foaming behaviour of AlSi11/TiH₂ composites made by semi-solid processing*, Materials Science and Engineering A, 2008, **480**: p. 283-288.
63. A. Haibel, A. Rack, J. Banhart, *Why are metal foams stable?* Applied Physics Letters, 2006, **89**: p. 154102-1-3.
64. A. Dudka, F. Garcia-Moreno, N. Wanderka, J. Banhart, *Structure and distribution of oxides in aluminium foam*, Acta Materialia, 2008, **56**: p. 3990-4001.
65. F. Simancik, K. Behulova, L. Bors, *Effect of ambient atmosphere on the foam expansion*, In: J. Banhart, M.F. Ashby, N.A. Fleck, editors, Cellular Metals and Metal Foaming Technology, MIT-Verlag, 2001: p.89-92.
66. P. Weigand, Thesis, Untersuchung der Einflussfaktoren auf die pulvermetallurgische Herstellung von Aluminiumschäumen, University of Aachen, Germany, 1999.
67. F. Garcia-Moreno, N. Babcsan, J. Banhart, *X-ray radioscopy of liquid metalfoams: influence of heating profile, atmosphere and pressure*, Colloids and Surfaces A, 2005, **263**: p. 290-294.
68. W. Zhaojin, H. Deping, *Changes of porosity of foamed aluminum during solidification*, In: J. Banhart, M.F. Ashby, N.A. Fleck, editors, Cellular Metals and Metal Foaming Technology, MIT-Verlag, 2001: p. 123-128.
69. V.V. Sobolev, *Modelling of solidification of metal foams*, In: J. Banhart, M.F. Ashby, N.A. Fleck, editors, Cellular Metals and Metal Foaming Technology, MIT-Verlag, 2001: 129-134.
70. S. Chu, Q. Niu, Y. Lin, K. Wu, *Control of foaming of Al alloy melt*, ISIJ International, 2000, **40**: p. 597-600.
71. A.E. Markaki, T.W. Clyne, *The effect of cell wall microstructure on the deformation and fracture of aluminium-based foams*, Acta Materialia, 2001, **49**: p. 1677-1686.

72. Y. Sugimura, J. Meyer, M.Y. He, H. Bart-Smith, J. Grenstedt, A.G. Evans, *On the mechanical performance of closed cell Al alloy foams*, Acta Materialia, 1997, **45**: p. 5245-5259.
73. E. Amsterdam, J.Th.M. De Hosson, P.R. Onck, *Failure mechanisms of closed-cell aluminum foam under monotonic and cyclic loading*, Acta Materialia, 2006, **54**: p. 4465-4472.
74. T. Ohgaki, H. Toda, M. Kobayashi, K. Uesugi, T. Kobayashi, M. Niinomi, T. Akahori, K. Makii, Y. Aruga, *In-situ high-resolution X-ray CT observation of compressive and damage behaviour of aluminium foams by local tomography technique*, Advanced Engineering Materials, 2006, **8**: p. 473-475.
75. N.L.M. Veldman, A.K. Dahle, D.H. StJohn, L. Arnberg, *Dendrite coherency of Al-Si-Cu alloys*, Metallurgical and Materials Transactions A, 2001, **32**: p. 147-155.
76. J. Campbell, Castings: The new metallurgy of cast metals, Second edition, Butterworth-Heinemann, Oxford, UK, 2003.
77. H. Bart-Smith, A.F. Bastawros, D.R. Mumm, A.G. Evans, D.J. Sypeck, H.N.G. Wadley, *Compressive deformation and yielding mechanisms in cellular Al alloys determined using X-ray tomography and surface strain mapping*, Acta Materialia, 1998, **46**: p. 3583-3592.
78. U. Ramamurty, A. Paul, *Variability in mechanical properties of a metal foam*, Acta Materialia, 2004, **52**: p. 869-876.
79. I. Jeon, T. Asahina, *The effect of structural defects on the compressive behavior of closed-cell Al foam*, Acta Materialia, 2005, **53**: p. 3415-3423.
80. Y. Sugimura, A. Rabiei, A.G. Evans, A.M. Harte, N.A. Fleck, *Compression fatigue of a cellular Al alloy*, Materials Science and Engineering A, 1999, **269**: p. 38-48.
81. M. Kolluri, M. Mukherjee, F. Garcia-Moreno, J. Banhart, U. Ramamurty, *Fatigue of a laterally constrained closed cell aluminum foam*, Acta Materialia, 2008, **56**: p. 1114-1125.
82. M. Mukherjee, F. Garcia-Moreno, J. Banhart, M. Kolluri, U. Ramamurty, *Deformation mechanisms in constrained monotonic and cyclic compressive loading of Al foam*, In: L.P. Lefebvre, J. Banhart, D. Dunand, editors, Porous Metals and Metallic Foams, DEStech Pub., Pennsylvania, 2008: p. 347-350.
83. M. Mukherjee, F. Garcia-Moreno, J. Banhart, *Anomalous behaviour of aluminium foams during solidification*. Transactions of the Indian Institute of Metals, 2007, **60**: p. 133-136.
84. F. Garcia-Moreno, M. Fromme., J. Banhart, *Real-time X-ray radioscopy on metallic foams using a compact micro-focus source*, Advanced Engineering Materials, 2004, **6**: p. 416-420.
85. P.W. Lee, Y. Trudel, R. Iacocca, R.M. German, B.L. Ferguson, W.B. Eisen, K. Moyer, D. Madan, H. Sanderow, editors, ASM Handbook: Powder Metal Technologies and Applications, volume 7, ASM International, Materials Park, OH, 1998.

86. N.A. Belov, D.G. Eskin, A.A. Aksenov, *Multicomponent Phase Diagrams: Applications for Commercial Aluminum Alloys*, Elsevier, 2005.
87. S.G. Shabestari, M.Malekan, *Thermal analysis study of the effect of the cooling rate on the microstructure and solidification parameters of 319 aluminum alloy*, Canadian Metallurgical Quarterly, 2005, **44**: p. 305-312.
88. H. Baker, editor, *ASM Handbook: Alloy Phase Diagrams*, volume 3, ASM International, Materials Park, OH, 1999.
89. D.G. Eskin, Suyitno, J. Mooney, L. Katgerman, *Contraction of aluminum alloys during and after solidification*, Metallurgical and Materials Transactions A, 2004, **35**: p. 1325-1335.
90. A. Takasaki, Y. Furuya, K. Ojima, Y. Taneda, *Hydride dissociation and hydrogen evolution behavior of electrochemically charged pure titanium*, Journal of Alloys and Compounds, 1995, **224**: p. 269-273.
91. A. Mitrasinovic, F.C. Robles Hernández, M. Djurdjevic, J.H. Sokolowski, *On-line prediction of the melt hydrogen and casting porosity level in 319 aluminum alloy using thermal analysis*, Materials Science and Engineering A, 2006, **428**: p. 41-46.
92. H. Liu, M. Bouchard, L. Zhang, *An experimental study of hydrogen solubility in liquid aluminium*, Journal of Materials Science, 1995, **30**: p. 4309-4315.
93. H. Liu, M. Bouchard, *Evaluation of interaction coefficient in Al-Cu-H alloy*, Metallurgical and Materials Transactions B, 1997, **28**: p. 625-632.
94. P. Lutze, J. Ruge, *Wasserstoff in Aluminium und seine Legierungen*, Metall, 1990, **8**: p. 741-748.
95. S.R. Shin, Z.H. Lee, G.S. Cho, K.W. Lee, *Hydrogen gas pick-up mechanism of Al-alloy melt during Lost Foam Casting*, Journal of Materials Science, 2004, **39**: p. 1563-1569.
96. P.N. Anyalebechi, *Analysis of the effects of alloying elements on hydrogen solubility in liquid aluminum alloys*, Scripta Metallurgica et Materialia, 1995, **33**: p. 1209-1216.
97. P.N. Anyalebechi, *Attempt to predict hydrogen solubility limits in liquid multicomponent aluminum alloys*, Scripta Materialia, 1996, **34**: p. 513-517.
98. R. Barrer, *Diffusion in and through Solids*, Cambridge University Press, Cambridge, UK, 1951.
99. B. Predel, editor, *Landolt-Börnstein: New Series IV/5 Phase Equilibria Crystallographic and Thermodynamic Data of Binary Alloys*, Springer, 1991.
100. L. Backerud, G. Chai, J. Tamminen, *Solidification Characteristics of Aluminum Alloys*, volume 2, Foundry Alloys, AFS / SkanAluminium, USA, 1990.
101. T. Magnusson, L. Arnberg, *Density and solidification shrinkage of hypoeutectic aluminum-silicon alloys*, Metallurgical and Materials Transactions A, 2001, **32**: p. 2605-2613.
102. H. Wipf, editor, *Hydrogen in Metals III: Properties and Applications*, Springer-Verlag Berlin, 1997.

103. H. Mehrer, editor, Landolt-Börnstein: Diffusion in Solid Metals and Alloys, volume 26, Springer-Verlag Berlin, 1990.
104. W. Eichenauer, J. Markopoulos, *Messung des Diffusionskoeffizienten von Wasserstoff in flüssigem Aluminium*, Zeitschrift für Metallkunde, 1974, **65**: p. 649-652.
105. A.B. Belonoshko, A. Rosengren, Q. Dong, G. Hultquist, C. Leygraf, *First-principles study of hydrogen diffusion in α -Al₂O₃ and liquid alumina*, Physical Review B, 2004, **69**: p. 24302-1-6.
106. J. Anson, J. Gruzleski, *The quantitative discrimination between shrinkage and gas microporosity in cast aluminum alloys using spatial data analysis*, Materials Characterization, 1999, **43**: p. 319-335.
107. G.M. Mala, D. Li, *Flow characteristics of water in microtubes*, International Journal of Heat and Fluid Flow, 1999, **20**: p. 142-148.
108. J. Pierson, Handbook of Refractory Carbides and Nitrides: Properties, Characteristics, Processing, and Applications, Noyes Publications, New Jersey, 1996.
109. ASM Handbook: Properties and Selection: Irons, Steels, and High Performance Alloys, volume 1, ASM International, Materials park, OH, 1990.
110. J.W. Paek, B.H. Kang, S.Y. Kim, J.M. Hyun, *Effective thermal conductivity and permeability of aluminum foam materials*, International Journal of Thermophysics, 2000, **21**: p. 453-464.